INFORMATION TO USERS

This manuscript has been reproduced from the microfilm master. UMI films the text directly from the original or copy submitted. Thus, some thesis and dissertation copies are in typewriter face, while others may be from any type of computer printer.

The quality of this reproduction is dependent upon the quality of the copy submitted. Broken or indistinct print, colored or poor quality illustrations and photographs, print bleedthrough, substandard margins, and improper alignment can adversely affect reproduction.

In the unlikely event that the author did not send UMI a complete manuscript and there are missing pages, these will be noted. Also, if unauthorized copyright material had to be removed, a note will indicate the deletion.

Oversize materials (e.g., maps, drawings, charts) are reproduced by sectioning the original, beginning at the upper left-hand corner and continuing from left to right in equal sections with small overlaps. Each original is also photographed in one exposure and is included in reduced form at the back of the book.

Photographs included in the original manuscript have been reproduced xerographically in this copy. Higher quality 6" x 9" black and white photographic prints are available for any photographs or illustrations appearing in this copy for an additional charge. Contact UMI directly to order.

UMI

A Bell & Howell Information Company
300 North Zeeb Road, Ann Arbor MI 48106-1346 USA
313/761-4700 800/521-0600

A COMPARISON AMONG LOCALIZED APPROXIMATIONS IN ONE-DIMENSIONAL PROFILE RECONSTRUCTION

by

Jacob Absolute Kwasi Adopley

A Dissertation Submitted to the Faculty of the

DEPARTMENT OF ELECTRICAL AND COMPUTER ENGINEERING

In Partial Fulfillment of the Requirements

For the Degree of

DOCTOR OF PHILOSOPHY

In the Graduate College

THE UNIVERSITY OF ARIZONA

1 9 9 6

THE UNIVERSITY OF ARIZONA ®
GRADUATE COLLEGE

As members of the Final Examination Committee, we certify that we have read the dissertation prepared by **Jacob Absolute Kwasi Adopley**

entitled **A Comparison Among Localized Approximations in One-Dimensional Profile Reconstruction**

and recommend that it be accepted as fulfilling the dissertation requirement for the Degree of **Doctor of Philosophy**

Donald G. Dudley	10/23/96 Date
Andreas Cangellaris	10/23/96 Date
Steven L. Dvorak	10/23/96 Date
	Date
	Date

Final approval and acceptance of this dissertation is contingent upon the candidate's submission of the final copy of the dissertation to the Graduate College.

I hereby certify that I have read this dissertation prepared under my direction and recommend that it be accepted as fulfilling the dissertation requirement.

Dissertation Director
Donald G. Dudley

10/23/96
Date

STATEMENT BY AUTHOR

This dissertation has been submitted in partial fulfillment of requirements for an advanced degree at The University of Arizona and is deposited in the University Library to be made available to borrowers under rules of the library.

Brief quotations from this dissertation are allowable without special permission, provided that accurate acknowledgment of source is made. Requests for permission for extended quotation from or reproduction of this manuscript in whole or in part may be granted by the head of the major department or the Dean of the Graduate College when in his or her judgment the proposed use of the material is in the interests of scholarship. In all other instances, however, permission must be obtained from the author.

SIGNED: 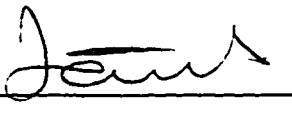

In memory of my father Akakpo B. Adopley

Dedicated to:

my mother A.A. Ametor

my wife Christine M. Adopley

and

my daughter Delali M.Y. Adopley

ACKNOWLEDGMENTS

For everything there is a beginning and an end. Maybe not! What about time? Well but this one, this is the end. It is over. The dream is now a reality. The journey was not easy but I met a lot of wonderful people along the way who made it possible.

First and foremost, I would like to thank my advisor, Professor D. G. Dudley, for his confidence in my abilities and his telescopic guidance. I also want to thank him for providing me with financial support throughout my graduate work.

I give thanks to my committee members, Professor A. Cangellaris, Professor S. Dvorak, Professor G. Lamb of the Mathematics Department, and Professor H. Groemer also of the Mathematics Department for reviewing this work. Over the years Professor Cangellaris has become a close friend and given me the inspiration and desire to do my best.

I cannot forget those guys at Schlumberger, Dr. Reza Taherian, Dr. Tarek Habashy and Ray White. It was a real pleasure to work with you all. I thank you Dr. Habashy for the interest you took in my work and for the useful comments and suggestions that make the completion of this work possible. I am also grateful to Schlumberger-Doll Research for providing the support for my graduate work.

I would not like to forget about the little folks. Jerry, I thank you for being a friend. How many turkeys haven't we devoured over these years? Now that it is over, I think some turkeys will actually be "happy". Give my thanks to your family for making me part of of the family. I always felt at home whenever I was there.

I thank Bill Pinello for visiting my family in New Castle Delaware. Bill I will miss the pizza days. Muntasir, thanks for "cracking the code" of my ways. So when I say there is Pork in the Pizza, you know what I really mean is leave it for me. Dave Heckmann, Pat Cicero, thanks for providing company. Jeff Seligman, thank you for setting up the alpha machines. Most of the "old" folks have gone! Chris, Charlie, and Justin.

Barbara Mrasak, I say thank you. Without you I don't think I could have got anything done with the university administration. Your grace and love have made it possible for me to handle the "insane" regulations of this administration.

My dear wife and daughter, I lower my hat for you. It has not been easy for all these years I was away from you. I cannot thank you enough. It is a blessing to have you as my family. Thanks.

TABLE OF CONTENTS

LIST OF FIGURES

ABSTRACT

We use the localized approximation and some modified versions of the localized approximation to study the electromagnetic field interaction of a plane wave with a slab of complex permittivity. The approximation as originally proposed is based on the localization property of the appropriate Green's function and the smooth variation of the internal field. In our one-dimensional case, the Green's function singularity degenerates into a localized peak. We apply two iterative techniques to the localized procedure in order to better simulate the internal fields. The first technique involves iterating the governing equation once before adopting the localized approximation, while the second technique involves iterating the localized approximation once. A study of other approximations based on the Born approximation is also included. In addition we present a generalization of the localized approximation using the Extended-Born approximation. We compare and contrast the performance of the various approximations in simulating the internal and external fields numerically.

The localized approximation and the two modified versions are next used in one-dimensional profile reconstruction based on a least-structured version of the least-squares inversion method. We compare and contrast the performance of the approximations in profile reconstruction. A noticeable consequence of these modifications is

an aggravation of the nonlinearity in the inverse problem. We investigate the consequences of this aggravation. We conclude with the introduction of a three-dimensional version of the localized approximation, the exploitation of which we leave for future work.

CHAPTER 1

Introduction

The task of electromagnetic profile inversion is extracting information about a material object from electromagnetic phenomenon observed or measured outside the material medium. The intrinsic quality that sets inversion problems apart from parameter estimation in statistics is that the unknowns are usually functions of space and time (or frequency). The implication is that, in principle, the solution contains an infinite number of variables and hence the problem is as underdetermined as it possibly can be. In addition inverse problems are well known to be nonunique. The nonuniqueness of electromagnetic inverse problems have been well documented in the literature [1]-[9] and will not be considered here. Rather, the present work is on the effectiveness of localized approximations as originally proposed by Habashy *et. al.* [10], and extensions thereto. As a vehicle for study, we consider a one spatial dimension problem involving scattering from a lossy dielectric slab, herein referred to as *the slab problem.*

The one-dimensional integral equation that describes the functional relationship between observed (or measurable) electromagnetic phenomena outside of the one-dimensional slab and its constitutive electromagnetic parameters seems deceptively

simple. The difficulty is embedded in the integrand of the integral equation. This integrand is the product of the unknown total internal electric fields, a Green's function, and the unknown contrast in complex conductivity (or permittivity). We emphasize that the internal electric field is functionally dependent on the slab complex conductivity profile. This renders the problem nonlinear. The starting point in obtaining a solution is finding an acceptable accurate approximation to the internal electric field. The first efforts in this direction were by Born [11] and Rytov[12]. The potentials and limitations of the two approximations have been reviewed extensively in the electromagnetic literature [13, 10, 15, 16]. Beyond the well known approximations of Born and Rytov, Habashy *et. al.* [10] proposed a nonlinear localized approximation based on the recognition that the Green's function has a singularity (in multidimensional problems) when computing the total internal electric field at the source point. Hence for internal fields that are smoothly varying, the field at the source point can be approximated by the field at the observation point. This approximation allows the internal electric field to be explicitly determined from the Green's function and the complex conductivity contrast. As pointed out by Torres-Verdin and Habashy [17], the technique is more difficult to apply in one-dimensional problems where the Green's function singularity degenerates into a localized peak or maximum.

Herein, we modify the localized approximation by introducing two iterative techniques in order to partially circumvent the difficulties in one-dimension. In the first

technique we iterate the governing equation once before adopting the localized approximation in [10], while in the second case we apply the iteration once after the localized approximation.

The first part of the present work deals with the evaluation of the effectiveness of the localized approximation (and modifications) in improving and/or enhancing accurate simulation of the total internal electric field. The second half of our work deals with the reconstruction of the slab conductivity profiles from noise contaminated synthetic data using the localized approximations and modifications. Most of the reconstruction techniques reported in the electromagnetic literature can be divided into two main groups, viz; the spectral-domain method which employs Fourier transform techniques and the weighted least-squares method. In the case of weak scatterers, the Born approximation is an acceptable accurate approximation and spectral methods are appropriate. Indeed the scattered field is just the Fourier transform of the conductivity profile with parameter $2k_b$, where k_b is the propagation constant of the homogeneous background medium. See the works of Tabbara [22]. Trantanella [19] used the method of super resolution to reconstruct high frequency dielectric constant.

The bulk of the reconstructions reported in the literature have used the least-squares method [23]-[31], based on minimizing the squares of the misfit between measured data and predicted data computed using a base model. A direct minimization of the least squares of the data misfit is very unstable. Hence, practical least-squares methods adopt regularization techniques [32, 33, 34] for stability and

for creating the illusion of obtaining a unique solution. Even though Levenberg [32] and Marquardt [33, 34] were the first ones to develop the regularization technique, it was not until 1977 that Tikhonov and Arsenin formalized the regularization into a theory in their now famous book [35].

In the least-squares method, it is important to select a model that ensures that any features exhibited by the model is required by the data [36]. Constable *et. al.* proposed a "smoothest" model based on minimizing the integral of the squares of the first or second derivative of the complex conductivity profile with respect to the slab axis. The model is called Occam's method. A generalization of the method was proposed later by Smith *et. al.* [37]. In their formulation, the derivative of the complex conductivity profile was taken with respect to a defined function of the slab axis, instead of just the slab axis. In that way, by changing the defined function they were able to change the characteristics of the model.

It is important to note that the least-squares technique is L_2 norm dependent and cannot estimate sharp discontinuities accurately. Rudin *et. al.* [38, 39] recognized this limitation in the least-squares method and proposed the use of the L_1 norm for reconstructing sharp changes in profiles accurately from noisy data. Kleinman *et. al.* [40] have adopted this method to reconstruct discontinuities in complex permittivity profiles. However, in their reported results, there was no firm basis for selecting a total variation penalty factor crucial to the accuracy of the reconstructions. This penalty factor was reportedly only determined after exhaustive numerical experimentation.

In the present work we adopt Occam's method [36] for its robustness and versatility. In the formulation we use the piecewise constant and linear profiles as models.

In chapter two, we introduce the slab problem. We derive an integral equation describing the electric field everywhere in space. For comparisons with existing literature, we include formulations in terms of both complex permittivity and complex conductivity.

In chapter three, we present the formulation of the localized approximation. Two extensions of the localized approximation are also formulated. In addition, we extend the Trantenella approximation [18, 19] to include lossy profiles. (In their study Trantanella *et. al.* [19] modified the Born approximation by including both a forward and a reflected wave approximation to the internal fields.)

In chapter four, we specialize the family of localized approximations to piecewise constant profiles. In chapter five, we do the same for linear profiles.

In chapter six, we perform numerical simulations using the approximations developed in chapter three. The simulations are carried out on the piecewise constant and the linear profiles. These results are evaluated for the various approximations against the exact solutions from transmission-line theory. We provide an exhaustive numerical study on the influence of both displacement and conduction currents on the accuracies of the various approximations.

In chapter seven we give a description and formalism of Occam's method. We compute explicit expressions of the Jacobians for all approximations.

The reconstruction of conductivities from contaminated synthetic data are performed in chapter eight. The effect of background complex conductivity profile on reconstruction is included. We also investigate numerically the effects of frequency and slab partition element size on reconstruction.

In chapter nine, as a basis for future work, we include a derivation (due to Habashy) of the generalization of the localized approximation applied to the Extended-Born approximation in three-dimensions. We present our summary and conclusions in chapter ten.

CHAPTER 2

Integral Equation Description of Slab

In this chapter we will give a description of the one-dimensional slab problem and perform a detailed derivation of the integral equation that governs the wave propagation in the slab. We will also derive the one-dimensional Green's function of the integral equation. The derivations will follow closely those of [18].

2.1 Physical Description of Slab

The geometry of the one-dimensional slab problem is illustrated in Figure 2.1. A slab of width d is located within the region $0 \leq z \leq d$. It extends to $+\infty$ from $-\infty$ in both x and y directions. It has a dielectric constant of ϵ_s and conductivity of σ_s, which are functions of space along the z-axis. The slab is assumed to be nonmagnetic with permeability μ_o. It is excited by a plane wave with the electric field linearly polarized along the y-axis. The wave is launched from the region $z < 0$ and propagates in the positive z-direction. It is generated by a plane sheet of electric current located in the region $z < 0$. The wave is time harmonic with $e^{j\omega t}$ time dependence.

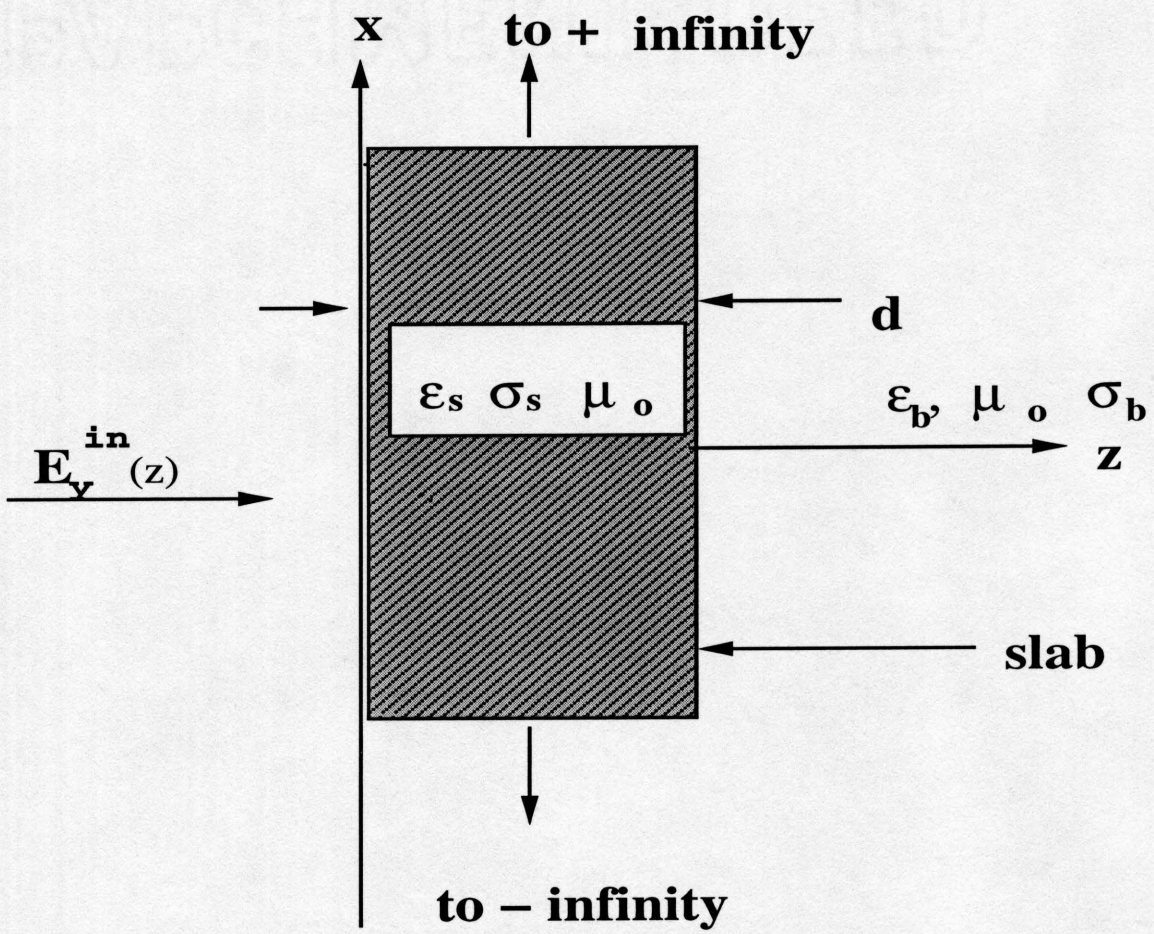

Figure 2.1: Dielectric Slab with Complex Permittivity

The slab is embedded in a homogeneous background medium. The homogeneous background medium has a dielectric constant of ϵ_b, a conductivity of σ_b and permeability of μ_o, which are all known quantities. In the next section we give a detailed derivation of the integral equation that governs wave propagation in the slab.

2.2 Derivation of the Integral Equation

With the time harmonic dependence assumed above, the Maxwell's equations that describe the wave phenomenon are

$$\nabla \times \vec{E} = -j\omega\mu_o\vec{H} \tag{2.1}$$

$$\nabla \times \vec{H} = j\omega\bar{\epsilon}\vec{E} + \vec{J} \tag{2.2}$$

where $\vec{E}$ is the electric field vector in *volts/meter*, $\vec{H}$ is the magnetic field vector in *amperes/meter*, $\vec{J}$ is the electric current density source in *amperes/(square meter)* and $\bar{\epsilon}$ is the complex permittivity defined by $\bar{\epsilon} = \epsilon - j\sigma/(\omega)$. The magnetic source $\vec{M}$ in *volts/(square meter)* is zero in our problem. We assume no variations in the x and y directions for both source and slab. Hence we have $\partial/\partial x = \partial/\partial y = 0$. The assumption above then decouples the TE_z and TM_z fields. For y-polarized $\vec{J}$, only the TEM_z mode is excited and the vector Maxwell's equations degenerate into scalar equations as follows:

$$\begin{aligned} \frac{dH_x}{dz} &= j\omega\bar{\epsilon}E_y + J_y \\ \frac{dE_y}{dz} &= j\omega\mu_o H_x \end{aligned} \tag{2.3}$$

We obtain the one-dimensional Helmholtz equation for wave propagation by taking the z derivative of the second equation in 2.3 and substituting it into the first equation in 2.3 to give

$$\frac{d^2E_y}{dz^2} + k^2E_y = -j\omega J_y \tag{2.4}$$

where k is the complex propagation constant, defined for homogeneous background medium and the slab regions as follows:

$$k^2 = \begin{cases} k_s^2 = \omega^2\mu_o[\epsilon_s(z) - j\sigma_s(z)/\omega] & \text{in the slab,} \\ k_b^2 = \omega^2\mu_o[\epsilon_b - j\sigma_b/\omega] & \text{in the background medium,} \end{cases} \tag{2.5}$$

We define the complex permittivity profile of the slab as

$$\bar{q}(z) = \bar{\epsilon}_{sr} - \bar{\epsilon}_{br} \tag{2.6}$$

where the subscript $_r$ refers to the relative complex permittivity constant relative to free space. We note that $\bar{q}(z) \neq 0$ *only* within the slab. The complex propagation constant becomes

$$k^2 = k_b^2\left[1 + \frac{\bar{q}(z)}{\bar{\epsilon}_{br}}\right] \tag{2.7}$$

where k_b is the constant complex propagation constant of the homogeneous background medium. We can then substitute for k^2 in equation (2.4) to obtain

$$\frac{d^2E_y}{dz^2} + k_b^2E_y = j\omega J_y - \frac{k_b^2}{\bar{\epsilon}_{br}}\bar{q}(z)E_y \tag{2.8}$$

We now solve equation (2.8) by the Green's function method [45]. Let us define the linear operator L as

$$L \equiv \frac{d^2}{dz^2} + k_b^2 \tag{2.9}$$

We write equation (2.8) in operator form as

$$LE_y = j\omega J_y - \frac{k_b^2}{\bar{\epsilon}_{br}}\bar{q}(z)E_y \tag{2.10}$$

We next define an inner product of V and U as

$$\langle V, U\rangle = \int_{-\infty}^{\infty} VU dz \tag{2.11}$$

We take the inner product of LE_y and the Green's function g, which is yet to be defined, to obtain

$$\langle g, LE_y\rangle = \langle Lg, E_y\rangle + \left[g\frac{dE_y}{dz} - E_y\frac{dg}{dz}\right]_{-\infty}^{\infty} \tag{2.12}$$

where the expressions on the right are obtained from integration by parts. The boundary conditions on E_y are

$$\lim_{z\to\pm\infty} E_y = 0 \tag{2.13}$$

Imposing the same boundary conditions on g eliminates the second expression on the right of equation (2.12). We therefore define the Green's function problem for g as follows:

$$Lg(z, z') = -\delta(z - z') \tag{2.14}$$

$$\lim_{z\to\pm\infty} g = 0 \tag{2.15}$$

The solution for E_y is then

$$E_y(z) = -j\omega\mu_o \int_{-\infty}^{\infty} J_y(z')g(z, z')dz' + \frac{k_b^2}{\bar{\epsilon}_{br}}\int_0^d \bar{q}(z')E_y(z')g(z, z')dz' \tag{2.16}$$

In the next section we will solve for the Green's function $g(z, z')$ explicitly.

2.3 Green's function

In the previous section, we defined the Green's function problem as

$$\begin{aligned} \frac{d^2g(z,z')}{dz^2} + k_b^2 g(z,z') &= -\delta(z-z') \\ \lim_{z\to\pm\infty} g(z,z') &= 0 \end{aligned} \tag{2.17}$$

where we have substituted the definition for the operator L. For $z \neq z'$, we have

$$\frac{d^2g(z,z')}{dz^2} + k_b^2 g(z,z') = 0 \tag{2.18}$$

The solution of equation (2.18), subject to boundary conditions in equation (2.17) is

$$g(z,z') = \begin{cases} Ae^{-jk_bz} & z > z', \\ Be^{jk_bz} & z < z' \end{cases} \tag{2.19}$$

where k_b is on the proper Riemann sheet with $\Im(k_b) < 0$. Continuity of g at $z = z'$ gives

$$B = Ae^{-2jk_bz'} \tag{2.20}$$

From the jump condition at $z = z'$, we obtain

$$A + Be^{2jk_bz'} = \frac{1}{jk_b}e^{jk_bz'} \tag{2.21}$$

Equations (2.20) and (2.21) can be solved simultaneously for A and B. Substituting the explicit solutions of A and B into equation (2.19) yields

$$g(z,z') = \frac{1}{2jk_b}e^{-jk_b|z-z'|} \tag{2.22}$$

which is the well-known one-dimensional Green's function for the one-dimensional Helmholtz equation with the appropriate boundary conditions.

We next substitute for $g(z,z')$ in the integral equation (2.16) to obtain

$$\begin{aligned} E_y(z) &= -j\omega\mu_o \frac{1}{2jk_b} \int_{-\infty}^{\infty} J_y(z') e^{-jk_b|z-z'|} dz' \\ &\quad + \frac{k_b}{2j\bar{\epsilon}_{br}} \int_0^d \bar{q}(z') E_y(z') e^{-jk_b|z-z'|} dz' \end{aligned} \tag{2.23}$$

For a plane sheet of current located at $z=-h$, $(h>0)$, we have $J_y(z) = J_o\delta(z+h)$. Substituting for $J_y(z)$ in equation (2.23) and performing the first integration yields

$$E_y(z) = -j\omega\mu_o \frac{1}{2jk_b} J_o e^{-jk_b h} e^{-jk_b z} + \frac{k_b}{2j\bar{\epsilon}_{br}} \int_0^d \bar{q}(z') E_y(z') e^{-jk_b|z-z'|} dz' \tag{2.24}$$

If we choose J_o such that $-j\omega\mu_o J_o e^{-jk_b h}/(2jk_b) = 1$, then equation (2.24) becomes

$$E_y(z) = e^{-jk_b z} + \frac{k_b}{2j\bar{\epsilon}_{br}} \int_0^d \bar{q}(z') E_y(z') e^{-jk_b|z-z'|} dz' \tag{2.25}$$

For convenience, the subscript $_r$ in ϵ_{br} will be dropped. Our final form of the one-dimensional integral equation is then

$$E_y(z) = e^{-jk_b z} + \frac{k_b}{2j\epsilon_b} \int_0^d \bar{q}(z') E_y(z') e^{-jk_b|z-z'|} dz' \tag{2.26}$$

We wish to state that nothing is new in this derivation. We include it for the sake of completeness and to establish notation.

2.4 Sigma formulation

We next reformulate the integral equation in terms of complex conductivity $(\bar{\sigma})$. We define complex conductivity $(\bar{\sigma})$ by $\bar{\sigma} = \sigma + j\epsilon\omega\epsilon_o$. From the integral equation,

we can write $\bar{q}(z) = (\epsilon_s - \epsilon_b) - j(\sigma_s - \sigma_b)/(\omega\epsilon_o)$ and $\bar{\epsilon_b} = \epsilon_b - j\sigma_b/(\omega\epsilon_o)$ as

$$\begin{aligned} \bar{q}(z) &= -j\frac{1}{\omega\epsilon_o}[(\sigma_s(z) - \sigma_b) + j\omega\epsilon_o(\epsilon_s - \epsilon_b)] = -j\frac{1}{\omega\epsilon_o}\bar{\sigma}(z) \\ \bar{\epsilon_b} &= -j\frac{1}{\omega\epsilon_o}(\sigma_b + j\omega\epsilon_o\epsilon_b) = -j\frac{1}{\omega\epsilon_o}\bar{\sigma_b} \end{aligned} \tag{2.27}$$

When we substitute these expressions into the integral equation we obtain

$$E_y(z) = e^{-jk_b z} + \frac{k_b}{2j\bar{\sigma_b}}\int_0^d \bar{\sigma}(z')g(z,z')E_y(z')dz' \tag{2.28}$$

which takes on the same form as the original equation with the complex permittivities replaced by complex conductivities. Equations (2.26) and (2.28) will be the centers of our investigation in the subsequent chapters.

CHAPTER 3

A Family of Localized Approximations

In this chapter we formulate different approximate solutions to the one-dimensional integral equation of the slab problem. We apply the localized approximate solution introduced by Habashy *et al.* [10] to compute the electric field within the slab and the scattered electric field. We develop two new localized approximations to the slab's total internal electric field based on the original Habashy approximation. These are denoted as the *Adopley* and the *Extended Habashy* approximations. We also develop an approximation called the *Habashy-Trantanella* approximation for the total internal electric field. The method combines the Habashy localized approximation with the technique employed by Trantanella *et. al.* [19]. We include a complete derivation of the Trantanella method which we have extended to include the complex permittivity cases. Finally, we investigate whether the various approximations can be obtained from a generalization of the localized approximation [20] beginning with the Extended Born approximation.

3.1 Habashy Approximation

In the Habashy approximation [10], the total electric field at the source point is approximated by the total electric field at the observation point for observation points limited to the source support. In this way we can rewrite the integral equation as

$$\begin{aligned} E_y(z) &= E_y^{in}(z) + \frac{k_b}{2j\bar{\epsilon}_b}\int_0^d \bar{q}(z')g(z,z')E_y(z)dz' \\ &+ \frac{k_b}{2j\bar{\epsilon}_b}\int_0^d \bar{q}(z')g(z,z')[E_y(z') - E_y(z)]dz' \end{aligned} \tag{3.1}$$

where

$$E_y^{in}(z) = e^{-jk_b z} \tag{3.2}$$

If we move the second term on the right to the left right and factor out the common $E_y(z)$ term, we obtain

$$\begin{aligned} E_y(z)\cdot\left[1 - \frac{k_b}{2j\bar{\epsilon}_b}\int_0^d \bar{q}(z')g(z,z')dz'\right] &= \frac{k_b}{2j\bar{\epsilon}_b}\int_0^d \bar{q}(z')g(z,z')[E_y(z') - E_y(z)]dz' \\ &+ E_y^{in}(z) \end{aligned} \tag{3.3}$$

We then solve for $E_y(z)$ as

$$E_y(z) = \Gamma(z)\cdot\left[E_y^{in}(z) + \frac{k_b}{2j\bar{\epsilon}_b}\int_0^d \bar{q}(z')g(z,z')[E_y(z') - E_y(z)]dz'\right] \tag{3.4}$$

where $\Gamma(z)$ is defined by

$$\Gamma(z) = \left[1 - \frac{k_b}{2j\bar{\epsilon}_b}\int_0^d \bar{q}(z')g(z,z')dz'\right]^{-1} \tag{3.5}$$

In the Habashy approximation, the internal electric field, $E_y(z)$ is given by

$$E_y(z) \approx \Gamma(z)\cdot E_y^{in}(z) \tag{3.6}$$

and the error introduced in this approximation is

$$\Gamma(z) \cdot \left[\frac{k_b}{2j\bar{\epsilon}_b} \int_0^d \bar{q}(z')g(z,z')[E_y(z') - E_y(z)]dz \right] \tag{3.7}$$

In order to extend the domain of validity and/or accuracy, we introduce two iterative techniques in the Habashy approximation. In the first case, which we call the Adopley approximation, we iterate the integral equation once before employing the localized approximation. In the second case, which we call the Extended Habashy approximation, we iterate the localized Habashy approximation once.

3.2 Adopley Approximation

Specifically, the internal field in the Adopley approximation is written as

$$E_y(z') = E_y^{in}(z') + \frac{k_b}{2j\bar{\epsilon}_b} \int_0^d \bar{q}(\xi)g(z',\xi)E_y(\xi)d\xi \tag{3.8}$$

When this is substituted back into the integral equation, we obtain

$$\begin{aligned} E_y(z) &= E_y^{in}(z) + \frac{k_b}{2j\bar{\epsilon}_b} \int_0^d \bar{q}(z')g(z,z') \left[E_y^{in}(z') \right. \\ &+ \left. \frac{k_b}{2j\bar{\epsilon}_b} \int_0^d \bar{q}(\xi)g(z',\xi)E_y(\xi)d\xi \right] dz' \end{aligned} \tag{3.9}$$

We incorporate the Habashy approximation by substituting the repeated approximations $E_y(\xi) \approx E_y(z') \approx E_y(z)$ into the second term on the right of equation (3.9) to obtain

$$\begin{aligned} E_y(z) &= E_y^{in}(z) + \frac{k_b}{2j\bar{\epsilon}_b} \int_0^d \bar{q}(z')g(z,z')E_y^{in}(z')dz' \\ &+ E_y(z) \left(\frac{k_b}{2j\bar{\epsilon}_b} \right)^2 \int_0^d dz' \int_0^d \bar{q}(z')g(z,z')\bar{q}(\xi)g(z',\xi)d\xi \end{aligned} \tag{3.10}$$

We then solve for $E_y(z)$ to obtain

$$E_y(z) = \left[E_y^{in}(z) + \frac{k_b}{2j\bar{\epsilon}_b}\int_0^d \bar{q}(z')g(z,z')E_y^{in}(z')dz'\right] \cdot \Gamma(z) \tag{3.11}$$

where $\Gamma(z)$ is given by

$$\Gamma(z) = \left[1 - \left(\frac{k_b}{2j\bar{\epsilon}_b}\right)^2 \int_0^d dz' \int_0^d \bar{q}(z')g(z,z')\bar{q}(\xi)g(z',\xi)d\xi\right]^{-1} \tag{3.12}$$

The error introduced is then given by

$$\Gamma(z) \cdot \left(\frac{k_b}{2j\bar{\epsilon}_b}\right)^2 \int_0^d dz' \int_0^d \bar{q}(z')g(z,z')\bar{q}(\xi)g(z',\xi)\left[E_y(\xi) - E_y(z)\right]d\xi \tag{3.13}$$

3.3 Extended Habashy approximation

For the Extended Habashy approximation we begin with the Habashy approximation by writing $E_y(z')$ as $\Gamma(z') \cdot E_y^{in}(z')$. When we substitute this into equation (3.4) we obtain

$$\begin{aligned} E_y(z) &= \Gamma(z) \cdot E_y^{in}(z) - \Gamma(z)^2 \cdot E_y^{in}(z)\left[\frac{k_b}{2j\bar{\epsilon}_b}\int_0^d \bar{q}(z')g(z,z')dz'\right] \\ &+ \Gamma(z) \cdot \left[\frac{k_b}{2j\bar{\epsilon}_b}\int_0^d \bar{q}(z')g(z,z')\Gamma(z') \cdot E_y^{in}(z')dz'\right] \end{aligned} \tag{3.14}$$

From the definition of $\Gamma(z)$ in the Habashy approximation, we have

$$\Gamma(z)^{-1} \cdot [1 - \Gamma(z)] = -\frac{k_b}{2j\bar{\epsilon}_b}\int_0^d \bar{q}(z')g(z,z')dz' \tag{3.15}$$

We incorporate this into the previous equation to obtain a more compact form as

$$\begin{aligned} E_y(z) &= \Gamma(z) \cdot E_y^{in}(z)\left[2 - \Gamma(z)\right] \\ &+ \frac{k_b}{2j\bar{\epsilon}_b}\Gamma(z)\int_0^d \bar{q}(z')g(z,z')\Gamma(z') \cdot E_y^{in}(z')dz' \end{aligned} \tag{3.16}$$

3.4 Habashy-Trantanella approximations

In judging our results, we shall make comparisons with the original Trantanella method which we have extended to the case of complex conductivity. We also extend the localized approximation to the Trantanella model. These will be used in the numerical simulations for comparisons against the other approximations and the exact solution from transmission-line theory.

3.4.1 Trantanella Approximation

Briefly in the Trantanella method, the internal electric field assumes the form

$$E_y(z') = Ae^{-jk_b z'} + B\frac{k_b}{2j\bar{\epsilon}_b}\int_0^d \bar{q}(\xi)e^{-jk_b\xi}e^{-jk_b|z'-\xi|}d\xi \tag{3.17}$$

where A and B are constants determined from the continuity of the tangential fields at the boundary $z = 0$. This expression is substituted into the integral equation to obtain

$$\begin{aligned} E_y(z) = e^{-jk_b z} &+ \frac{k_b}{2j\bar{\epsilon}_b}\int_0^d \bar{q}(z')e^{-jk_b|z-z'|}\Big[Ae^{-jk_b z'} \\ &+ B\frac{k_b}{2j\bar{\epsilon}_b}\int_0^d \bar{q}(\xi)e^{-jk_b\xi}e^{-jk_b|z'-\xi|}d\xi\Big]\,dz' \end{aligned} \tag{3.18}$$

For $z < 0 < z'$, we can rewrite equation (3.18) as

$$\begin{aligned} E_y(z) = e^{-jk_b z} &+ \frac{k_b}{2j\bar{\epsilon}_b}e^{jk_b z}\Big[A\int_0^d \bar{q}(z')e^{-2jk_b z'} \\ &+ B\frac{k_b}{2j\bar{\epsilon}_b}\int_0^d \bar{q}(z')e^{-jk_b z'}dz'\int_0^d \bar{q}(\xi)e^{-jk_b\xi}e^{-jk_b|z'-\xi|}d\xi\Big] \end{aligned} \tag{3.19}$$

In the above equation, we can express the last integration of the double integral as

$$\begin{aligned}\int_0^d \bar{q}(\xi)e^{-jk_b\xi}e^{-jk_b|z'-\xi|}d\xi &= e^{-jk_bz'}\int_0^{z'}\bar{q}(\xi)d\xi - e^{jk_bz'}\int_0^{z'}\bar{q}(\xi)e^{-2jk_b\xi}d\xi \\ &+ e^{jk_bz'}\int_0^d \bar{q}(\xi)e^{-2jk_b\xi}d\xi \end{aligned} \tag{3.20}$$

Define $Q(2k_b)$ and q_{av} as

$$\begin{aligned} Q(2k_b) &\equiv \int_0^d \bar{q}(\xi)e^{-2jk_b\xi}d\xi \\ dq_{av} &\equiv \int_0^d \bar{q}(z)dz \end{aligned}$$

We use equation (3.20) to evaluate equation (3.18) as

$$\begin{aligned} E_y(z) &= e^{-jk_bz} + \frac{k_b}{2j\bar{\epsilon}_b}e^{jk_bz}\left[AQ(2k_b) + Bdq_{av}\frac{k_b}{2j\bar{\epsilon}_b}Q(2k_b)\right. \\ &+ \left. B\frac{k_b}{2j\bar{\epsilon}_b}\int_0^d \bar{q}(z')dz'\left(\int_0^{z'}\bar{q}(\xi)e^{-2jk_b\xi}d\xi - e^{-2jk_bz'}\int_0^{z'}\bar{q}(\xi)d\xi\right)\right] \end{aligned} \tag{3.21}$$

At this point, Trantanella made the assumption that in the double integrals the slab profile $q(z)$ can be approximated by its average value. The double integrals are then readily evaluated to obtain

$$E_y(z) = e^{-jk_bz} + \frac{k_b}{2j\bar{\epsilon}_b}e^{jk_bz}\left[AQ(2k_b) + B\left(\frac{k_b}{2j\bar{\epsilon}_b}dq_{av}Q(2k_b) + \chi\right)\right] \tag{3.22}$$

where χ is given by

$$\chi = \frac{k_bd}{2\bar{\epsilon}_b}q_{av}^2e^{jk_bd}\left(\cos(k_bd) - \frac{\sin(k_bd)}{k_bd}\right) \tag{3.23}$$

The constants A and B are evaluated by matching the internal and external tangential fields at the boundary $z = 0$. From the expression for the internal electric field, we

have for $z' < \xi$

$$E_y(z') = Ae^{-jk_b z'} + B\left(\frac{k_b}{2j\bar{\epsilon}_b}e^{jk_b z'}Q(2k_b)\right) \tag{3.24}$$

Matching the tangential electric and magnetic fields at $z = z' = 0$ yields the following two equations:

$$\begin{aligned} A + B\left(\frac{k_b}{2j\bar{\epsilon}_b}Q(2k_b)\right) &= 1 + \frac{k_b}{2j\bar{\epsilon}_b}\left[AQ(2k_b) + B\left(\frac{k_b}{2j\bar{\epsilon}_b}dq_{av}Q(2k_b) + \chi\right)\right] \\ B\left(\frac{k_b}{2j\bar{\epsilon}_b}Q(2k_b)\right) - A &= \frac{k_b}{2j\bar{\epsilon}_b}\left[AQ(2k_b) + B\left(\frac{k_b}{2j\bar{\epsilon}_b}dq_{av}Q(2k_b) + \chi\right)\right] - 1 \end{aligned} \tag{3.25}$$

We compute A and B to be

$$A = 1 \tag{3.26}$$

$$B = \frac{Q(2k_b)}{Q(2k_b)\left(1 - dq_{av}\frac{k_b}{2j\bar{\epsilon}_b}\right) - \chi} \tag{3.27}$$

Using expressions for A and B, we can write $E_y(z)$ for $z < 0$ as

$$E_y(z) = e^{-jk_b z} + \frac{k_b}{2j\bar{\epsilon}_b}e^{jk_b z}\frac{Q^2(2k_b)}{Q(2k_b)\left(1 - \frac{k_b}{2j\bar{\epsilon}_b}dq_{av}\right) - \chi} \tag{3.28}$$

This completes the formal derivation of the Trantanella formulation. The major approximation in the Trantanella formulation is assuming the same propagation constant for the slab and background media.

3.4.2 Localized Extension

We now combine the Habashy approximation with the Trantanella method [18]. We approximate the internal field for an incident plane wave by

$$E_y(z) = \Gamma(z) \cdot \left[Ae^{-jk_b z} + Be^{jk_b z} \right] \tag{3.29}$$

where A and B are constants to be determined. The external field then becomes

$$E_y(z) = e^{-jk_b z} + \frac{k_b}{2j\bar{\epsilon}_b} e^{jk_b z} \int_0^d \bar{q}(z')\Gamma(z')e^{-jk_b z'} \left(Ae^{-jk_b z} + Be^{jk_b z} \right) dz' \tag{3.30}$$

for $z < z'$. We next evaluate the constants A and B from the continuity of the tangential fields at the slab boundary. Matching the tangential fields at the boundary $z = 0$, we obtain

$$1 + A \cdot Q_g(2k_b) + B \cdot Q_g(0) = \Gamma(0) \cdot (A + B) \tag{3.31}$$

$$\begin{aligned} -1A \cdot Q_g(2k_b) + B \cdot Q_g(0) &= \Gamma(0) \cdot (B - A) \\ &+ \frac{1}{jk_b}[A + B] \cdot \frac{d}{dz}\Gamma(z)|_{z=0} \end{aligned} \tag{3.32}$$

for the electric and magnetic fields respectively. From the definition of $\Gamma(z)$ we compute its derivative with respect to z and obtain

$$\begin{aligned} \frac{1}{jk_b}\frac{d}{dz}\Gamma(z)|z = 0 &= \frac{k_b}{2j\bar{\epsilon}_b}\Gamma(0)^2 \int_0^d \bar{q}(z')e^{-jk_b z'}dz' \\ &= GF(q) \end{aligned} \tag{3.33}$$

where $F(q)$, G and $Q_g(\cdot)$ are defined by

$$F(q) = \int_0^d \bar{q}(z')e^{-jk_b z'}dz'$$

$$
\begin{aligned}
G &= \Gamma(0)^2 \frac{k_b}{2j\bar{\epsilon}_b} \\
Q_g(\alpha k_b) &= \int_0^d \bar{q}(z')\Gamma(z')e^{-j\alpha k_b z'} dz'
\end{aligned}
\tag{3.34}
$$

We then rewrite equation (3.32) as

$$
\Gamma(0)\cdot(-A+B) + GF(q)\cdot(A+B) = -1 + A\cdot Q_g(2k_b) + B\cdot Q_g(0) \tag{3.35}
$$

We can solve for A and B from the two equations above to obtain

$$
A = \frac{\chi_a}{\chi_a\left[\Gamma(0) - \frac{1}{2}GF(q)\right] - \frac{1}{2}GF(q)\chi_b} \tag{3.36}
$$

$$
B = \frac{\chi_b}{\chi_a\left[\Gamma(0) - \frac{1}{2}GF(q)\right] - \frac{1}{2}GF(q)\chi_b} \tag{3.37}
$$

where

$$
\chi_a = \Gamma(0) - Q_q(0) + \frac{1}{2}GF(q) \tag{3.38}
$$

$$
\chi_b = Q_g(2k_b) - \frac{1}{2}GF(q) \tag{3.39}
$$

We again note that the propagation constant for the slab region is the same as that of the homogeneous background.

3.5 Generalized Local Approximation

It is important to know whether some of the above approximations can be extracted from a generalized local approximation of the Extended Born approximation [20]. We shall present the generalized local approximation and then show that the

various approximations derived above are just special cases. In the formulation, we adopt the following generic form of the integral equation:

$$E(z) = E_b(z) + \int_0^d \bar{\sigma}(z')G(z,z')E(z')dz' \tag{3.40}$$

where $G(z,z')$ is the Green function and the support of $\bar{\sigma}(z)$ is $(0,d)$. In this notation, the Green function $G(z,z')$ for the one-dimensional problem is

$$G(z,z') = \frac{k_b}{2j\bar{\sigma}_b} e^{-k_b|z-z'|} \tag{3.41}$$

The Extended Born approximations are accomplished by repeated iteration of the integral equation, namely,

$$E(z) = \sum_0^{N-1} E_n(z) + e_N(z) \tag{3.42}$$

where $E_n(z)$ and $e_N(z)$ are

$$E_n(z) = \int_0^d \bar{\sigma}(z')G(z,z')E_{n-1}(z')dz' \tag{3.43}$$

$$\begin{aligned} e_N(z) &= \int_0^d \bar{\sigma}(z_1)G(z,z_1)dz_1 \int_0^d \bar{\sigma}(z_2)G(z_1,z_2)dz_2 \cdots \\ &\cdot \int_0^d \bar{\sigma}(z_{N-1})G(z_{N-2},z_{N-1})dz_{N-1} \int_0^d \bar{\sigma}(z_N)G(z_{N-1},z_N)E(z_N)dz_N \end{aligned} \tag{3.44}$$

with $E_0(z) = E_b(z)$. Only the first $N-1$ terms in the summation are kept with $e_N(z)$ defining the residual error. $e_N(z)$, the residual error, can alternately be expressed as

$$e_n(z) = \int_0^d \bar{\sigma}(z')G(z,z')e_{n-1}(z')dz' \tag{3.45}$$

with $e_0(z) = E(z)$. We may apply the localized approximation to equation (3.44) or equation (3.45) to derive two different results as follows:

3.5.1 First Approximation

We apply the localized approximation repeatedly to equation (3.44) such that

$$E(z_N) \approx E(z_{N-1}) \approx \cdots \approx E(z_2) \approx E(z_1) \approx E(z) \tag{3.46}$$

and we obtain

$$e_N(z) \;=\; \Lambda_N(z) \cdot E(z) \tag{3.47}$$

where $\Lambda_N(z)$ is the N-tuple integral given by

$$\begin{aligned} \Lambda_N \;=\; & \int_0^d \bar{\sigma}(z_1) G(z, z_1) dz_1 \int_0^d \bar{\sigma}(z_2) G(z_1, z_2) dz_2 \cdots \\ & \cdot \int_0^d \bar{\sigma}(z_{N-1}) G(z_{N-2}, z_{N-1}) dz_{N-1} \int_0^d \bar{\sigma}(z_N) G(z_{N-1}, z_N) dz_N \end{aligned} \tag{3.48}$$

Substituting equation (3.47) into equation (3.42), we get for the internal electric field

$$E^{int}(z) \approx \Gamma_N(z) \cdot \sum_0^{N-1} E_n(z) \tag{3.49}$$

where

$$\Gamma_N(z) = [1 - \Lambda_N(z)]^{-1} \tag{3.50}$$

For $N = 1$ we note that

$$\Gamma_1(z) = \left[1 - \int_0^d \bar{\sigma}(z') G(z, z') dz'\right]^{-1} \tag{3.51}$$

and the internal electric field becomes

$$E^{int}(z) \approx \Gamma_1(z) \cdot E_b(z) \tag{3.52}$$

which is the Habashy approximation. For $N = 2$ we we note that

$$\sum_{0}^{N-1} E_n(z) = E_b(z) + \int_0^d \bar{\sigma}(z')G(z,z')E_b(z')dz' \tag{3.53}$$

$$\Gamma_2(z) = \left[1 - \int_0^d \bar{\sigma}(z')G(z,z')dz' \int_0^d \bar{\sigma}(z'')G(z',z'')dz''\right]^{-1} \tag{3.54}$$

and we obtain the internal electric field as

$$E^{int}(z) \approx \Gamma_2(z) \cdot \left[E_b(z) + \int_0^d \bar{\sigma}(z')G(z,z')E_b(z')dz'\right] \tag{3.55}$$

which is the Adopley approximation.

3.5.2 Second Approximation

We can effect the localized approximation on equation (3.45) as

$$e_n(z) \approx \Omega(z) \cdot e_{n-1}(z) \tag{3.56}$$

where

$$\Omega(z) = \int_0^d \bar{\sigma}(z')G(z,z')dz' \tag{3.57}$$

The residual error $e_N(z)$ becomes

$$e_N(z) \approx [\Omega(z)]^N \cdot E(z) \tag{3.58}$$

Again substituting equation (3.58) into equation (3.42) we obtain for the internal electric field

$$E^{int}(z) \approx \Gamma_N(z) \cdot \sum_{0}^{N-1} E_n(z) \tag{3.59}$$

where

$$\Gamma_N(z) = \left[1 - [\Omega(z)]^N\right]^{-1} \tag{3.60}$$

Once again we note that for $N = 1$, this approximation yields the Habashy approximation. For $N = 2$, we note that

$$\Gamma_2(z) = \left[1 - [\Omega(z)]^2\right]^{-1} \tag{3.61}$$

which we can write in terms of $\Gamma_1(z)$ as

$$\Gamma_2(z) = \frac{[\Gamma_1(z)]^2}{2\Gamma_1(z) - 1} \tag{3.62}$$

since

$$\int_0^d \bar{\sigma}(z')G(z,z')dz' = \left[\frac{\Gamma_1(z) - 1}{\Gamma_1(z)}\right] \tag{3.63}$$

The internal electric field becomes

$$E^{int}(z) \approx \left[\frac{[\Gamma_1(z)]^2}{2\Gamma_1(z) - 1}\right] \cdot \left[E_b(z) + \int_0^d \bar{\sigma}(z')G(z,z')E_b(z')dz'\right] \tag{3.64}$$

This is not the same as the expressions in the Extended-Habashy approximation derived above. It will therefore be left for future work.

3.6 Limitations

Before we conclude this chapter, we wish to comment on the limitations of the approximate solutions presented above. The conditions for the use of the Habashy approximation are; (1) the total field within the slab is smoothly varying; and (2) the

Green function has a singularity or is sharply peaked at $r = r'$ [17], where r and r' are the observation and source points, respectively. For multidimensional problems, the Green function fulfills the singularity condition. Exclusive of extremely sharp discontinuities in complex conductivity profiles, a smoothly varying internal field is not an unreasonable assumption. In the one-dimensional case, the dominant part of the Greens function $e^{-jk_b|z-z'|}$ is nonsingular at $z = z'$. The best we can hope for is a localized maximum at $z = z'$. This is true for $e^{-jk_b|z-z'|}$, if $\Im(k_b) \ll 0$. We can therefore infer from the above analysis that the Habashy approximation will be most effective for systems with very lossy homogeneous background medium.

The next approximate solution presented is the Adopley model. The iteration before the localized approximation is the Born approximation, well known to be very effective for electrically small systems with low complex permittivity contrast between homogeneous background medium and scatterer. Hence we expect the Adopley model to be more accurate for very low loss systems but with a lower frequency range than the Habashy approximation.

In the Extended-Habashy approximation, part of the error term neglected in the Habashy model has been included. Thus we expect the Extended-Habashy approximation to give better accuracy than the Habashy approximation under similar conditions. In the case of the Habashy-Trantanella approximation, we would generally predict better results from the more complete modeling of the wave phenomenon within the slab.

In the next two chapters we present complete solutions of the integral equation for piecewise constant and linear profiles of slab complex conductivities, using the various approximations presented above. We shall present numerical simulations after the derivations in the following chapter.

CHAPTER 4

Piecewise Constant Profile

In this chapter we present solutions of the integral equation for piecewise constant profiles of the slab complex conductivity ($\bar{\sigma}$). The equations derived in this chapter will be used for the numerical simulations of the internal total electric field and the scattered external electric field at the boundaries of the slab. We first present the exact analytical solution using transmission line theory.

For piecewise constant profile we partition the slab into N-elements not necessarily even. This is illustrated in Figure 4.1. We define the piecewise constant complex conductivity function of the slab to be

$$\bar{\sigma}(z) = \sum_{n=1}^{N} \bar{\sigma}_n f_n(z) \tag{4.1}$$

where

$$f_n(z) = \begin{cases} 1; & z \in (z_{n-1}, z_n) \\ 0; & otherwise \end{cases} \tag{4.2}$$

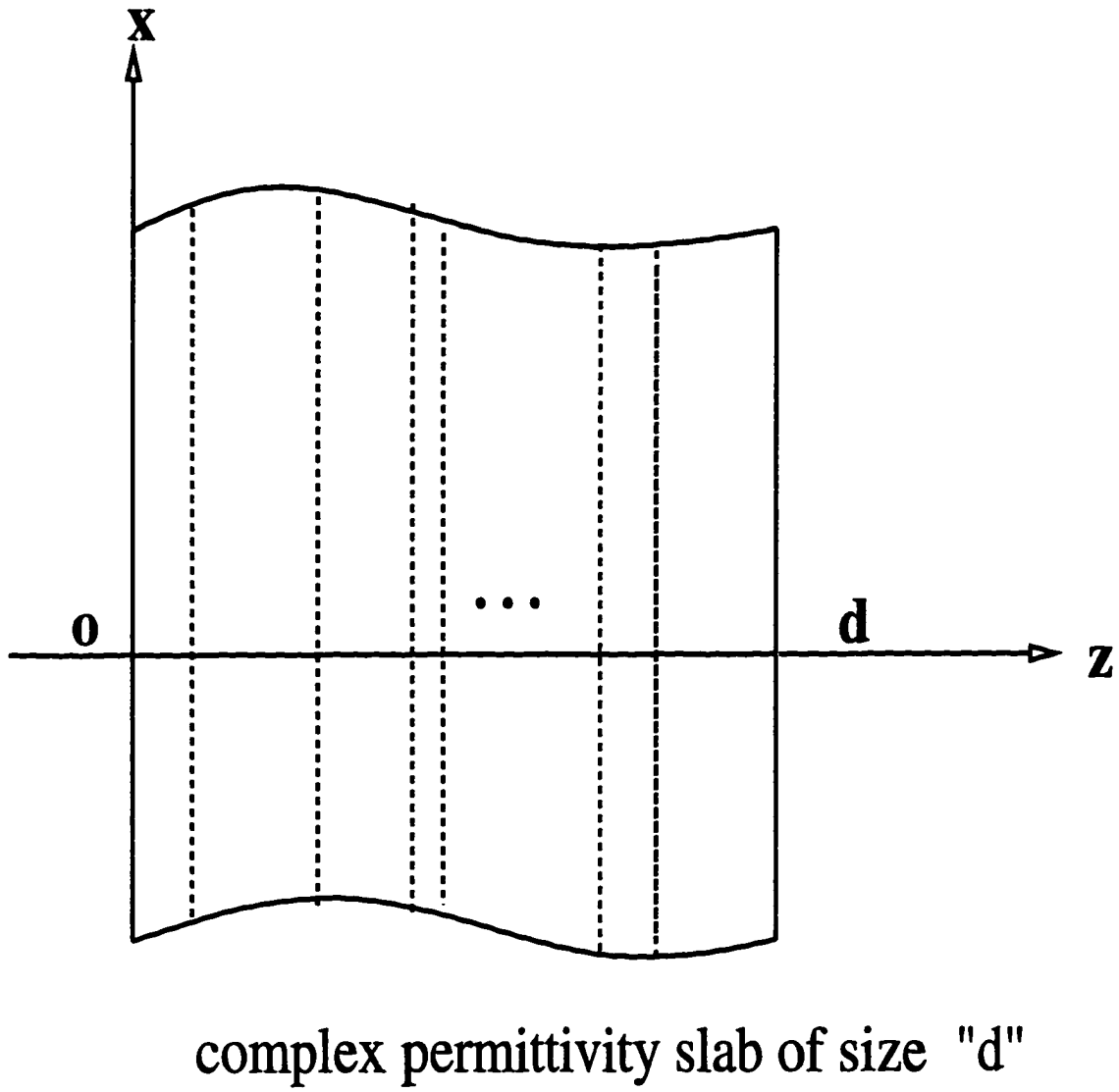

Figure 4.1: Partitioned Slab of Nonuniform Size

4.1 Analytical Solution

We present the transmission line solution of the fields inside a slab of constant complex conductivity profile from a uniform plane wave of unit amplitude normally incident at the boundary $z = 0$. The electric field is defined for each region as

$$E_y(z) = \begin{cases} e^{-jk_b z} + Re^{jk_b z} & ; z < 0 \\ T_s e^{-jk_s z} + R_s e^{jk_s z}; & z \in (0, d) \\ Te^{-jk_b z}; & z > d \end{cases} \tag{4.3}$$

The complex characteristic impedance of the background and slab media are η_b and η_s respectively. Matching the tangential fields at the boundary $z = 0$ we obtain

$$\begin{aligned} 1 + R &= T_s + R_s \\ \frac{\eta_s}{\eta_b}(1 - R) &= T_s - R_s \end{aligned} \tag{4.4}$$

Adding and subtracting the two equations in (4.4), we obtain

$$\begin{aligned} T_s &= \frac{1}{2}\left[1 + \frac{\eta_s}{\eta_b}\right] + \frac{1}{2}R\left[1 - \frac{\eta_s}{\eta_b}\right] \\ R_s &= \frac{1}{2}\left[1 - \frac{\eta_s}{\eta_b}\right] + \frac{1}{2}R\left[1 + \frac{\eta_s}{\eta_b}\right] \end{aligned} \tag{4.5}$$

Also from matching the tangential fields at the boundary $z = d$, we have

$$T_s e^{-jk_s d} + R_s e^{jk_s d} = Te^{-jk_s d} \tag{4.6}$$

from which we obtain T as

$$T = T_s + R_s e^{2jk_s d} \tag{4.7}$$

where the solutions for T_s and R_s are given in equation (4.5). In the above analysis, the solutions are derived in terms of R. The solution for R can be derived from transmission line theory as follows: The slab is taken as transmission line of length d and characteristic impedance of η_s [21]. The load at $z = d$ is the characteristic impedance of the homogeneous background medium η_b. We compute the input impedance at $z = 0$ to be

$$Z_{in} = \eta_s \frac{\eta_b + j\eta_s \tan(k_s d)}{\eta_s + j\eta_b \tan(k_s d)} \tag{4.8}$$

which then becomes the load impedance for the incident region with characteristic impedance η_b. We then compute the reflection coefficient R as

$$R = \frac{Z_L - \eta_b}{Z_L + \eta_b} \tag{4.9}$$

where $Z_L = Z_{in}$ which is given in equation (4.8) above. In the case of N slabs, the above process is repeated until the desired region is reached. This then gives the exact analytic solution for the slab problem from transmission line theory. This solution is used as the bench-mark against which the performance of the various localized approximations are evaluated.

4.2 Habashy Approximation

For the Habashy approximation, the internal electric field is

$$E_y(z) \approx \Gamma(z) \cdot E_y^{in}(z) \tag{4.10}$$

where for a plane wave incidence, $E_y^{in}(z) = e^{-jk_b z}$ and

$$\Gamma(z)^{-1} = 1 - \frac{k_b}{2j\bar{\sigma}_b}\int_0^d \bar{\sigma}(z')g(z,z')dz' \tag{4.11}$$

In the case of the piecewise constant profile, the expression for $\Gamma(z)$ depends on the partition element in which z is located. We identify z on the m^{th} element by denoting $\Gamma(z)$ as $\Gamma_m(z)$. Hence

$$\begin{aligned}\Gamma_m(z)^{-1} = 1 \;-\; & \frac{k_b}{2j\bar{\sigma}_b}\left\{e^{-jk_b z}\sum_{n=1}^{m-1}\bar{\sigma}_n\int_{z_{n-1}}^{z_n} e^{jk_b z'}dz'\right. \\ & \left. +\; e^{jk_b z}\sum_{n=m+1}^{N}\bar{\sigma}_n\int_{z_{n-1}}^{z_n} e^{-jk_b z'}dz' + \bar{\sigma}_m\int_{z_{m-1}}^{z_m} e^{-jk_b|z-z'|}dz'\right\}\end{aligned} \tag{4.12}$$

After performing the above elementary integrations, we obtain

$$\begin{aligned}\Gamma_m(z)^{-1} \;=\; & 1 + \frac{1}{2\bar{\sigma}_b}\left\{\left[\sum_{n=1}^{m-1}\bar{\sigma}_n\left(e^{jk_b z_n} - e^{jk_b z_{n-1}}\right) - \bar{\sigma}_m e^{jk_b z_{m-1}}\right]e^{-jk_b z}\right. \\ & \left. -\; \left[\sum_{n=m+1}^{N}\bar{\sigma}_n\left(e^{-jk_b z_n} - e^{-jk_b z_{n-1}}\right) + \bar{\sigma}_m e^{-jk_b z_m}\right]e^{jk_b z} + 2\bar{\sigma}_m\right\}\end{aligned} \tag{4.13}$$

The scattered electric field for $z < 0$ is therefore given by

$$E_y^s(z) \;\approx\; \frac{k_b}{2j\bar{\sigma}_b}e^{jk_b z}\sum_{n=1}^{N}\bar{\sigma}_n\int_{\Delta n} e^{-2jk_b z'}\Gamma_n(z')dz' \tag{4.14}$$

where $\Gamma_n(z)$ is defined above and $\Delta n = z_n - z_{n-1}$. We next derive the expressions for the scattered waves of the Adopley model.

4.3 Adopley Model

In the Adopley approximation, the scattered electric field for $z < 0$ is given by

$$E_y^s(z) \;\approx\; \frac{k_b}{2j\bar{\sigma}_b}e^{jk_b z}\int_o^d \bar{\sigma}e^{-jk_b z'}\bar{E}(z')\Gamma(z')dz' \tag{4.15}$$

where $\bar{E}(z)$ and $\Gamma(z)$ are defined as:

$$\begin{aligned}\bar{E}(z) &= e^{-jk_b z} + \frac{k_b}{2j\bar{\sigma}_b}\int_0^d \bar{\sigma}(z')e^{-jk_b|z-z'|}e^{-jk_b z}dz' \\ \Gamma(z)^{-1} &= 1 - \left(\frac{k_b}{2j\bar{\sigma}_b}\right)^2 \int_0^d \bar{\sigma}(z')e^{-jk_b|z-z'|}dz' \int_0^d \bar{\sigma}(\xi')e^{-jk_b|z'-\xi|}d\xi\end{aligned}$$

for plane wave incidence. When we adopt the piecewise constant profile for $\bar{\sigma}$, we identify z on the m^{th} partition element by placing a subscript on $\bar{E}(z)$. Hence $\bar{E}_m(z)$ means that z is located on the m^{th} partition element. Similarly for $\Gamma(z)$, $\Gamma_p(z)$ means z is located on p^{th} partition element. This system of subscripting will be the standard for all quatities in the piecewise profile analysis. Thus we have

$$\begin{aligned}\bar{E}_m(z) &= e^{-jk_b z} + \frac{k_b}{2j\bar{\sigma}_b}\left\{e^{-jk_b z}\sum_{n=1}^{n=m-1}\bar{\sigma}_n\int_{z_{n-1}}^{z_n}dz' + \bar{\sigma}_m e^{-jk_b z}\int_{z_{m-1}}^{z}dz'\right. \\ &+ \left.\bar{\sigma}_m e^{jk_b z}\int_z^{z_{m+1}} e^{-2jk_b z}dz' + e^{jk_b z}\sum_{n=m+1}^{N}\bar{\sigma}_n\int_{z_{n-1}}^{z_n} e^{-2jk_b z}dz'\right\} \qquad (4.16)\end{aligned}$$

When we evaluate the integrals in the above equation, we obtain

$$\begin{aligned}\bar{E}_m(z) &= \left\{1 - \frac{j}{4\bar{\sigma}_b}\left[2\sum_{n=1}^{n=m-1}\bar{\sigma}_n k_b(z_n - z_{n-1}) + \bar{\sigma}_m(2k_b[z - z_{n-1}] - j)\right]\right\}e^{-jk_b z} \\ &+ \frac{1}{4\bar{\sigma}_b}\left[\sum_{n=m+1}^{N}\bar{\sigma}_n\left(e^{-2jk_b z_n} - e^{-2jk_b z_{n-1}}\right) + \bar{\sigma}_m e^{-2jk_b z_m}\right]e^{jk_b z} \qquad (4.17)\end{aligned}$$

If we substitute the expression for $\bar{\sigma}$ into the Γ expression, we get

$$\Gamma(z)^{-1} = 1 - \left(\frac{k_b}{2j\bar{\sigma}_b}\right)^2 \sum_{n=1}^{N}\bar{\sigma}_n\int_{z_{n-1}}^{z_n} e^{-jk_b|z-z'|}dz' \sum_{m=1}^{N}\bar{\sigma}_m\int_{z_{m-1}}^{z_m} e^{-jk_b|z'-\xi|}d\xi \qquad (4.18)$$

With z on the p^{th}-element, we can write Γ as

$$\Gamma_p(z)^{-1} = 1 + \left(\frac{k_b}{2\bar{\sigma}_b}\right)^2 \left[e^{-jk_b z}\sum_{n=1}^{p-1}\bar{\sigma}_n\int_{z_{n-1}}^{z_n} e^{jk_b z'}dz'\left(\sum_{m=1}^{N}\bar{\sigma}_m\int_{z_{m-1}}^{z_m} e^{-jk_b|z'-\xi|}d\xi\right)\right.$$

$$
\begin{aligned}
&+ \bar{\sigma}_p e^{-jk_b z} \int_{z_{p-1}}^{z} e^{jk_b z'} dz' \left(\sum_{m=1}^{N} \bar{\sigma}_m \int_{z_{m-1}}^{z_m} e^{-jk_b|z'-\xi|} d\xi \right) \\
&+ \bar{\sigma}_p e^{jk_b z} \int_{z}^{z_p} e^{-jk_b z'} dz' \left(\sum_{m=1}^{N} \bar{\sigma}_m \int_{z_{m-1}}^{z_m} e^{-jk_b|z'-\xi|} d\xi \right) \\
&+ e^{jk_b z} \sum_{n=p+1}^{N} \bar{\sigma}_n \int_{z_{n-1}}^{z_n} e^{-jk_b z'} dz' \left(\sum_{m=1}^{N} \bar{\sigma}_m \int_{z_{m-1}}^{z_m} e^{-jk_b|z'-\xi|} d\xi \right) \Bigg] \qquad (4.19)
\end{aligned}
$$

We note that the second integration in each term is the same one evaluated for Γ in the Habashy model. Thus we have for the second integration,

$$
\begin{aligned}
\sum_{m=1}^{N} \bar{\sigma}_m \int_{z_{m-1}}^{z_m} e^{-jk_b|z'-\xi|} d\xi = \Bigg\{ &\left[\sum_{m=1}^{n-1} \bar{\sigma}_m \left(e^{jk_b z_m} - e^{jk_b z_{m-1}} \right) - \bar{\sigma}_n e^{jk_b z_{n-1}} \right] e^{-jk_b z} \\
&+ 2\bar{\sigma}_n - \left[\sum_{m=n+1}^{N} \bar{\sigma}_m \left(e^{-jk_b z_m} - e^{-jk_b z_{m-1}} \right) + \bar{\sigma}_n e^{-jk_b z_n} \right] e^{jk_b z} \Bigg\} \frac{1}{jk_b} \qquad (4.20)
\end{aligned}
$$

where z' is on the n^{th}-element. In order to track the analysis, we make the following substitutions:

$$
\begin{aligned}
Q_{Ln} &= \sum_{m=1}^{n-1} \bar{\sigma}_m \left(e^{jk_b z_m} - e^{jk_b z_{m-1}} \right) - \bar{\sigma}_n e^{jk_b z_{n-1}} \\
Q_{Un} &= \sum_{m=n+1}^{N} \bar{\sigma}_m \left(e^{-jk_b z_m} - e^{-jk_b z_{m-1}} \right) + \bar{\sigma}_n e^{-jk_b z_n} e^{jk_b z} \qquad (4.21)
\end{aligned}
$$

We can then write $\Gamma_p(z)$ as

$$
\begin{aligned}
\Gamma_p(z)^{-1} &= 1 + \left(\frac{k_b}{2\bar{\sigma}_b} \right)^2 \left(\frac{1}{jk_b} \right) \times \\
&\Bigg[e^{-jk_b z} \sum_{n=1}^{p-1} \bar{\sigma}_n \int_{z_{n-1}}^{z_n} e^{jk_b z'} dz' \left(Q_{Ln} e^{-jk_b z'} + 2\bar{\sigma}_n - Q_{Un} e^{jk_b z'} \right) \\
&+ \bar{\sigma}_p e^{-jk_b z} \int_{z_{p-1}}^{z} e^{jk_b z'} dz' \left(Q_{Lp} e^{-jk_b z'} + 2\bar{\sigma}_p - Q_{Up} e^{jk_b z'} \right) \\
&+ \bar{\sigma}_p e^{jk_b z} \int_{z}^{z_p} e^{-jk_b z'} dz' \left(Q_{Lp} e^{-jk_b z'} + 2\bar{\sigma}_p - Q_{Up} e^{jk_b z'} \right) \\
&+ e^{jk_b z} \sum_{n=p+1}^{N} \bar{\sigma}_n \int_{z_{n-1}}^{z_n} e^{-jk_b z'} dz' \left(Q_{Ln} e^{-jk_b z'} + 2\bar{\sigma}_n - Q_{Un} e^{jk_b z'} \right) \Bigg] \qquad (4.22)
\end{aligned}
$$

We performed the integrations to obtain

$$\begin{aligned}
[\Gamma_p(z)]^{-1} &= 1 - \left(\frac{\bar{\sigma}_p}{\sigma_b}\right)^2 - \frac{1}{8\sigma_b^2}\left(\sum_{m=1}^{p-1} \bar{\sigma}_m F_{m1}(\bar{\sigma}) + \bar{\sigma}_p F_{p1}\right) e^{-jk_b z} \\
&+ \frac{1}{8\sigma_b^2}\left(\sum_{m=p+1}^{N} \bar{\sigma}_m F_{m2}(\bar{\sigma}) + \bar{\sigma}_p F_{p2}\right) e^{jk_b z} \qquad (4.23)
\end{aligned}$$

where

$$\begin{aligned}
F_{m1}(\bar{\sigma}) &= 2jk_b\Delta_m Q_{Lm} + 4\bar{\sigma}_m\left(e^{jk_b z_m} - e^{jk_b z_{m-1}}\right) \\
&- Q_{Um}\left(e^{2jk_b z_m} - e^{2jk_b z_{m-1}}\right) \\
F_{m2}(\bar{\sigma}) &= 2jk_b\Delta_m Q_{Um} + Q_{Lm}\left(e^{-2jk_b z_m} - e^{-2jk_b z_{m-1}}\right) \\
&+ 4\bar{\sigma}_m\left(e^{-jk_b z_m} - e^{-jk_b z_{m-1}}\right) \\
F_{p1}(\bar{\sigma}) &= \left(1 + 2jk_b\Delta_{p-1}\right) Q_{Lp} + Q_{Up} e^{2jk_b z_{p-1}} - 4\bar{\sigma}_p e^{jk_b z_{p-1}} \\
F_{p2}(\bar{\sigma}) &= \left(1 + 2jk_b\Delta_p\right) Q_{Up} + Q_{Lp} e^{-2jk_b z_p} + 4\bar{\sigma}_p e^{-jk_b z_p} \qquad (4.24)
\end{aligned}$$

We also define the following quantities in the above expressions as

$$\begin{aligned}
\Delta_m &= z_m - z_{m-1} \\
\Delta_{p-1} &= z - z_{p-1} \\
\Delta_p &= z_p - z
\end{aligned}$$

This completes the derivation of the necessary equations for the piecewise constant profile of the Adopley model. The external electric field is then given by

$$E_y^s(z) \approx \frac{k_b}{2j\bar{\sigma}_b} e^{jk_b z} \sum_{n=1}^{N} \bar{\sigma}_n \int_{\Delta n} e^{-jk_b z'} \bar{E}_n(z') \Gamma_n(z') dz' \qquad (4.25)$$

where $\bar{E}_n(z')$ and $\Gamma_n(z')$ are defined above.

4.4 Extended Habashy Approximation

In the case of the Extended Habashy model, we only need to compute Γ which is the same for the Habashy model. The approximation for the external electric field is therefore

$$\begin{aligned} E_y^s(z) &\approx \frac{k_b}{2j\bar{\sigma}_b} e^{jk_b z} \sum_{n=1}^{N} \bar{\sigma}_n \int_{\Delta n} e^{-jk_b z'} \bar{E}_n(z') dz' \quad \text{for} \quad z < 0 \\ E_y^s(z) &\approx \frac{k_b}{2j\bar{\sigma}_b} e^{-jk_b z} \sum_{n=1}^{N} \bar{\sigma}_n \int_{\Delta n} e^{jk_b z'} \bar{E}_n(z') dz' \quad \text{for} \quad z > d \end{aligned} \tag{4.26}$$

where $\bar{E}_p(z)$ is given by

$$\begin{aligned} \bar{E}_p(z) &= \Gamma_p(z) \cdot \left(e^{-jk_b z}[2 - \Gamma_p(z)] + \frac{k_b}{2j\bar{\sigma}_b} e^{-jk_b z} \sum_{n=1}^{p-1} \bar{\sigma}_n \int_{\Delta n} \Gamma_n(z') dz' \right. \\ &+ \frac{k_b}{2j\bar{\sigma}_b} e^{jk_b z} \sum_{n=p+1}^{N} \bar{\sigma}_n \int_{\Delta n} e^{-2jk_b z'} \Gamma_n(z') dz' \\ &+ \left. \frac{k_b}{2j\bar{\sigma}_b} \bar{\sigma}_p \int_{\Delta_p} e^{-jk_b z'} e^{-jk_b |z - z'|} \Gamma_p(z') dz' \right) \end{aligned} \tag{4.27}$$

$\Gamma_n(z)$ is the same as for the Habashy approximation.

4.5 Trantanella Approximation

In case of the Trantanella formulation, we needed to compute $Q(2k_b)$ and q_{av} only. These we readily evaluate and find

$$\begin{aligned} q_{av} &= \frac{1}{d} \sum_{n=1}^{N} \bar{\sigma}_n \Delta_n \\ Q(2k_b) &= \frac{j}{2k_b} \sum_{n=1}^{N} \bar{\sigma}_n \left(e^{-2jk_b z_n} - e^{-2jk_b z_{n-1}} \right) \end{aligned}$$

Thus for the piecewise constant complex conductivity profile the Trantanella approximation for ($z < 0$) is given by

$$E_y(z) = e^{-jk_b z} + \frac{k_b}{2j\epsilon_b} e^{jk_b z} \frac{Q^2(2k_b)}{Q(2k_b)\left(1 - \frac{k_b}{2j\epsilon_b} dq_{av}\right) - \chi} \tag{4.28}$$

where $Q(2k_b)$ and q_{av} are defined above. This then completes the piecewise constant profile derivations. These equations are used in the inversion formulations in subsequent chapters.

CHAPTER 5

Linear Profile

We now introduce the linear profile by the following definition:

$$\bar{\sigma} = \beta z \tag{5.1}$$

where β can accept complex values. We will first compute, the $\Gamma_n(z)$ of the Habashy model followed by evaluation of $\bar{E}_n(z')$ and $\Gamma_n(z')$ from the Adopley model. As was the case for the piecewise constant profile, results for the Trantanella and the Extended Habashy formulation will be available from these computations.

5.1 Analytical Solution

In our numerical simulations conducted in the next chapter, the performance of the various approximations will be compared against the exact solutions for piecewise constant and linear profiles of slab complex permittivity. We therefore present a solution of the differential equation governing wave propagation in a slab of linear complex permittivity profile. The differential equation governing wave propagation within the slab is given by

$$\frac{d^2}{dz^2}E_y(z) = -\omega^2\mu_o\bar{\epsilon}(z)E_y(z) \tag{5.2}$$

where $\bar{\epsilon}(z) = \bar{\epsilon}_b + q(z)$. As noted earlier, $\bar{\epsilon}_b = \epsilon_b - j\sigma_b/(\omega\epsilon_o)$ is the homogeneous background complex permittivity and $q(z) = \bar{\alpha}z$ is the difference between the slab and homogeneous background complex permittivities. We then rewrite the differential equation as

$$\frac{d^2}{dz^2}E_y(z) = -k_b^2[\hat{\epsilon}_b + \hat{\alpha}z]E_y(z) \tag{5.3}$$

In the above equation, $k_b^2 = \omega^2\epsilon_b\epsilon_o\mu_o$, $\hat{\epsilon}_b = 1 - j\sigma_b/(\omega\epsilon_o\epsilon_b)$ and $\hat{\alpha} = \alpha_e - j\alpha_s/(\omega\epsilon_o\epsilon_b)$. Here α_e is the linear slope of the slab dielectric constant (ϵ_s) and α_s is the linear slope of the slab conductivity (σ_s). Let us denote $k_b^2[\hat{\epsilon}_b + \hat{\alpha}z]$ by x, then from the chain rule we have

$$\alpha_o\hat{\alpha}\frac{d}{dx} = \frac{d}{dz} \tag{5.4}$$

where $\alpha_o \equiv k_b^2$ is used for convenience. The differential equation then becomes

$$(\alpha_o\hat{\alpha})^2\frac{d^2}{dx^2}E_y(x) = -xE_y(x) \tag{5.5}$$

Let $x = \beta\xi$ where β is an unknown parameter to be determined. We can apply the chain rule again to obtain

$$\frac{d}{dx} = \frac{1}{\beta}\frac{d}{d\xi} \tag{5.6}$$

and our differential equation becomes

$$\frac{d^2}{d\xi^2}E_y(\xi) = -\frac{\beta^3}{(\alpha_o\hat{\alpha})^2}\xi E_y(\xi) \tag{5.7}$$

We note from the above differential equation that if $\beta = (\alpha_o\hat{\alpha})^{(2/3)}$ then the differential equation becomes

$$\frac{d^2}{d\xi^2}E_y(\xi) = -\xi E_y(\xi) \tag{5.8}$$

which is one form of the Riccati equation ($y' = y^2 + x$ with a transformation $y(x) = -v'(x)/v(x)$) [48]. It has solutions

$$E_y(\xi) = C_1 Ai(-\xi) + C_2 Bi(-\xi) \tag{5.9}$$

where Ai and Bi are *Airy* functions of the first and second kind respectively. The constants C_1 and C_2 will be evaluated using transmission-line theory for a plane wave at normal incidence. We evaluate ξ from the various transformations as a function of z to be

$$\xi = \alpha_o^{1/3}[\hat{\epsilon}_b\hat{\alpha}^{-2/3} + \hat{\alpha}^{1/3}z] \tag{5.10}$$

where all the other parameters are as previously defined. We define the following quantities

$$k_s = (\alpha_o\hat{\alpha})^{1/3} \tag{5.11}$$

$$z_o = \alpha_o^{1/3}\hat{\epsilon}_b\hat{\alpha}^{-2/3} \tag{5.12}$$

$$z_d = z_o + k_s d \tag{5.13}$$

The exact solution can then be expressed as

$$E_y(z) = C_1 Ai(-z_o - k_s z) + C_2 Bi(-z_o - k_s z) \tag{5.14}$$

The electric field outside the slab is given by

$$E_y(z) = e^{-jk_b z} + Re^{jk_b z} \quad \text{for} \quad z < 0 \tag{5.15}$$

$$E_y(z) = Te^{-jk_b z} \quad \text{for} \quad z > d \tag{5.16}$$

where R and T are the reflection and transmission coefficients respectively. We match the tangential fields at the boundaries to obtain

$$1 + R = C_1 Ai(-z_o) + C_2 Bi(-z_o) \tag{5.17}$$

$$1 - R = -j\left(\frac{k_s}{k_b}\right)[C_1 Ai'(-z_o) + C_2 Bi'(z_o)] \tag{5.18}$$

$$Te^{-jk_b d} = C_1 Ai(-z_d) + C_2 Bi(-z_d) \tag{5.19}$$

$$Te^{-jk_b d} = -j\left(\frac{k_s}{k_b}\right)[C_1 Ai'(-z_d) + C_2 Bi'(z_d)] \tag{5.20}$$

From the last two equations we compute C_2 as

$$C_2 = -C_1 \frac{Ai(-z_d) + j\left(\frac{k_s}{k_b}\right) Ai'(-z_d)}{Bi(-z_d) + j\left(\frac{k_s}{k_b}\right) Bi'(-z_d)} \tag{5.21}$$

Upon adding the first two equations and substituting for C_2 we find C_1 to be

$$C_1 = 2\frac{Bi(-z_d) + j\left(\frac{k_s}{k_b}\right) Bi'(-z_d)}{A_o B_d - A_d B_o} \tag{5.22}$$

where

$$A_o B_d = \left[Ai(-z_o) - j\left(\frac{k_s}{k_b}\right) Ai'(-z_o)\right]\left[Bi(-z_d) + j\left(\frac{k_s}{k_b}\right) Bi'(-z_d)\right] \tag{5.23}$$

$$\tag{5.24}$$

and

$$A_d B_o = \left[Ai(-z_d) + j\left(\frac{k_s}{k_b}\right) Ai'(-z_d)\right]\left[Bi(-z_o) - j\left(\frac{k_s}{k_b}\right) Bi'(-z_o)\right] \tag{5.25}$$

These are the equations used in the exact simulation for the linear profile.

5.2 Habashy Approximation

Adopting the linear profile of complex conductivity, we obtain for $\Gamma(z)$

$$\Gamma(z)^{-1} = 1 - \frac{k_b}{2j\bar{\sigma}_b}\beta \int_0^d z' e^{-jk_b|z-z'|} dz' \tag{5.26}$$

which can be written as

$$\Gamma(z)^{-1} = 1 - \frac{k_b}{2j\bar{\sigma}_b}\beta \left[e^{-jk_b z} \int_0^z z' e^{jk_b z'} dz' + e^{jk_b z} \int_z^d z' e^{-jk_b z'} dz' \right] \tag{5.27}$$

We evaluate the integrals and find

$$\Gamma(z)^{-1} = 1 - \frac{1}{2j\bar{\sigma}_b k_b}\beta \left[\left(1 + (k_b)^2 Q(k_b)\right) e^{jk_b z} - e^{-jk_b z} - 2jk_b z \right] \tag{5.28}$$

where

$$Q(k_b) = \int_0^d z e^{-jk_b z} dz = \frac{1}{(k_b)^2} \left[(1 + jk_b d) e^{-jk_b d} - 1 \right] \tag{5.29}$$

The scattered external electric field for $z < 0$ is then

$$E_y^s(z) \approx \frac{k_b}{2j\bar{\sigma}_b}\beta e^{jk_b z} \int_0^d z' e^{-j2k_b z'} \Gamma(z') dz' \tag{5.30}$$

5.3 Adopley Approximation

In the Adopley Approximation, the external scattered electric field is

$$E_y^s(z) \approx \frac{k_b}{2j\bar{\sigma}_b}\beta e^{jk_b z} \int_0^d z' e^{-jk_b z'} \bar{E}(z') \Gamma(z') dz' \quad \text{for} \quad z < 0 \tag{5.31}$$

$$E_y^s(z) \approx \frac{k_b}{2j\bar{\sigma}_b}\beta e^{-jk_b z} \int_0^d z' e^{jk_b z'} \bar{E}(z') \Gamma(z') dz' \quad \text{for} \quad z > d \tag{5.32}$$

where

$$\bar{E}_y(z) = e^{-jk_b z} + \frac{k_b}{2j\bar{\sigma}_b}\beta \int_0^d z' e^{-jk_b z'} e^{-jk_b|z-z'|} dz' \tag{5.33}$$

and

$$\Gamma(z) = 1 + \left(\frac{k_b\beta}{2\bar{\sigma}_b}\right)^2 \int_0^d z' e^{-jk_b|z-z'|} dz' \int_0^d \xi e^{-jk_b|z'-\xi|} d\xi \tag{5.34}$$

Since the above integrations are similar to the ones performed in the Habashy approximation, we resist from going through the algebra and present only the results. Performing the integrations we obtain $\bar{E}_y(z)$ and $\Gamma(z)$ as:

$$\begin{aligned}
\bar{E}_y(z) &= \left[1 + j\frac{\beta}{8k_b\bar{\sigma}_b}\left(1 + 2jk_bz - 2(k_bz)^2\right)\right] e^{-jk_bz} \\
&- j\frac{\beta}{8k_b\bar{\sigma}_b}\left[1 + 2jk_bd\right] e^{-2jk_bd} e^{jk_bz} \qquad (5.35) \\
\Gamma(z)^{-1} &= \left(\frac{\beta}{2k_b\bar{\sigma}_b}\right)^2 \left\{ e^{-jk_bz}\left(\frac{1}{4}\bar{Q}(k_b)\left[(1 - 2jk_bz)e^{2jk_bz} - 1\right]\right.\right. \\
&+ 2j\left[2j - \left(2k_bz + 2j - j(k_bz)^2\right)e^{jk_bz}\right] - \frac{1}{2}(k_bz)^2\Big) \\
&+ e^{jk_bz}\left(\frac{1}{2}\bar{Q}(k_b) - 2j\left[2j + \left(2k_bd + j(k_bd)^2 - 2j\right)e^{-jk_bd}\right]\right. \\
&- (k_b)^2 Q(2k_b) - \frac{1}{4}\left[1 - (1 + 2jk_bz)e^{-2jk_bz}\right] \\
&+ \left.\left. 2j\left[2j + \left(2k_bz + j(k_bz)^2 - 2j\right)e^{-jk_bz}\right] - \frac{1}{2}(k_bz)^2\bar{Q}(k_b)\right)\right\} \qquad (5.36)
\end{aligned}$$

where $\bar{Q}(k_b)$ and $Q(2k_b)$ are defined as

$$\bar{Q}(k_b) = 1 + (k_b)^2 \int_0^d z e^{-jk_bz} dz = (1 + jk_bd)e^{-jk_bd} \tag{5.37}$$

$$Q(2k_b) = \int_0^d z e^{-2jk_bz} dz = \frac{1}{(2k_b)^2}\left[(1 + 2jk_bd)e^{-2jk_bd} - 1\right] \tag{5.38}$$

This then defines the Adopley approximation for the linear profile.

5.4 Extended Habashy Approximation

As was the case in the previous profile, the expressions for the Extended Habashy approximation can easily be extracted from the Habashy model. Hence we obtain

$$\begin{aligned} E_y^s(z) &\approx \frac{k_b}{2j\bar{\sigma}_b}\beta e^{jk_b z}\int_0^d z' e^{-jk_b z'}\bar{E}(z')dz' \quad \text{for} \quad z<0 \\ E_y^s(z) &\approx \frac{k_b}{2j\bar{\sigma}_b}\beta e^{-jk_b z}\int_0^d z' e^{jk_b z'}\bar{E}(z')dz' \quad \text{for} \quad z>d \end{aligned} \tag{5.39}$$

where $\bar{E}(z)$ is given by

$$\begin{aligned} \bar{E}(z) &= \Gamma(z)\cdot\left(e^{-jk_b z}(2-\Gamma(z)) + \frac{k_b}{2j\bar{\sigma}_b}\beta e^{-jk_b z}\int_0^z z'\Gamma(z')dz'\right. \\ &+ \left.\frac{k_b}{2j\bar{\sigma}_b}\beta e^{jk_b z}\int_z^d z' e^{-2jk_b z'}\Gamma(z')dz'\right) \end{aligned} \tag{5.40}$$

where $\Gamma(z)$ is the same for the Habashy approximation above.

5.5 Trantanella Approximation

As was the case for the piecewise constant profile, we only need to compute q_{av} and $Q(2k_b)$ for the Trantanella approximation. From the definitions of q_{av} and $Q(2k_b)$ we obtain the following results:

$$q_{av} = \frac{1}{d}\beta\int_0^d z dz = \frac{1}{2}\beta d \tag{5.41}$$

$$Q(2k_b) = \beta\int_0^d z e^{-2jk_b z}dz = \frac{1}{4k_b^2}\left[(1+2jk_b d)e^{-2jk_b d}-1\right] \tag{5.42}$$

We use these results for q_{av} and $Q(2k_b)$ in the expressions for the electric fields.

A major limitation to the Trantanella Approximation is that, $Q(2k_b)$ cannot be accurately computed in multi-dimensions.

CHAPTER 6

Numerical Simulations

In this chapter, we perform our numerical investigation on the accuracy of the various approximations in modeling the internal electric field. The study is limited to two complex conductivity profiles, viz; the piecewise constant profile and the linear profile. Figure 6.1 shows the different types of piecewise constant profiles we investigated. These are characterized as: "Constant" or "Uniform", "Left-Step", "Right-Step" and "Inclusion". The points $z = 0$ and $z = d$ are referred to as the *measurement boundaries.* Also the actual space occupied by the slab profile within the measurement boundaries we refer to as the *slab region.* For the "Uniform" profile, the slab region coincides with the measurement boundaries. In the "Left-Step" profile, the slab region extends from the left measurement boundary, $z = 0$ to $z = d/2$, while for the "Right-Step" profile, the slab region extends from $z = d/2$ to the right measurement boundary at $z = d$. The "Inclusion" profile is located symmetrically between the measurement boundaries. Apart from the "Uniform" profile, all profile sizes are $d/2$ where d is the distance between the measurement boundaries in meters.

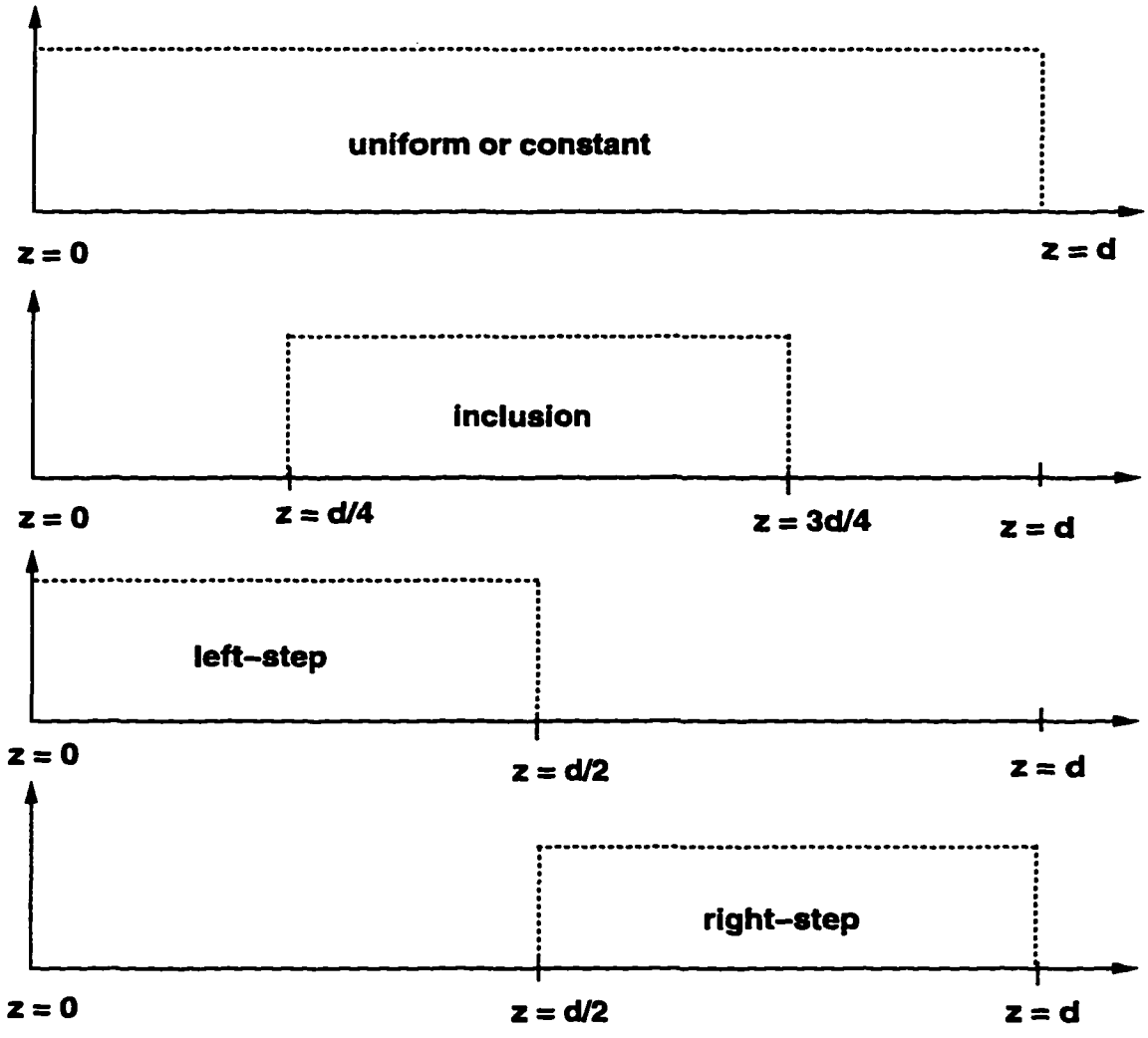

Slab Profile Types

Figure 6.1: Types of the Piecewise Constant Conductivity Profile of the Slab

We investigate the effects of homogeneous background loss-tangent, frequency and conductivity contrasts on model accuracies. The first part of the numerical investigations involves the uniform piecewise constant profile. The numerical simulations are compared against exact closed-form solutions from transmission-line theory. Each individual model has been tested at three distinct regions of loss-tangent for the slab. The first test is for a slab of very high loss-tangent when conduction currents dominate energy propagation. The second test is for a slab of moderate values of loss-tangent when conduction and displacement currents are of equal strength. Finally we tested a slab of very small loss-tangent when displacement currents dominate energy propagation.

The numerical investigation of the linear profile is performed on both lossless and lossy systems. In the lossless system, we an perform absolute comparison against the exact solution from transmission-line theory as computed in the previous chapter. For the lossy system we consider only comparative evaluations among the different models. This is the result of our inability to locate a reliable routine to generate consistent and accurate numerical values for the *Airy* functions of complex arguments. Below are some of the results of our numerical investigations.

6.1 Constraints on the Background Medium

Before we present our numerical results, we digress to examine the physical implications of the complex conductivity slab profile and characteristic properties required

of the homogeneous background medium to effectively model field propagation in a lossy slab. From contraction theory, it can be shown that a necessary requirement is that the homogeneous background medium must be complex for accurate simulation of the internal electric field using iterative methods.

6.2 Piecewise Constant Profiles

The numerical simulations for the piecewise constant profiles are for the internal total electric fields and the external scattered fields on the boundaries of the slab. We first present results on the internal total electric fields.

6.2.1 Internal Electric field

The first set of numerical investigations is on the uniform profile. The numerical simulation is for the total internal electric field inside the slab. The width of the slab is 1.0 meter. The loss-tangents for both the background and the slab are given on the individual plots. Also provided are the permittivities and conductivities of both background and slabs. In Figure 6.2 we perform a check on all models, by allowing the slab and the homogeneous background medium to have the same complex permittivity profiles. As expected the results are exact. All parameters used are defined on the figures. In Figure 6.3, the parameters are selected to obtain a loss-tangent of 1.8 for the slab and 1.8×10^{-3} for the homogeneous background medium. The dielectric constant of both the homogeneous background medium and the slab

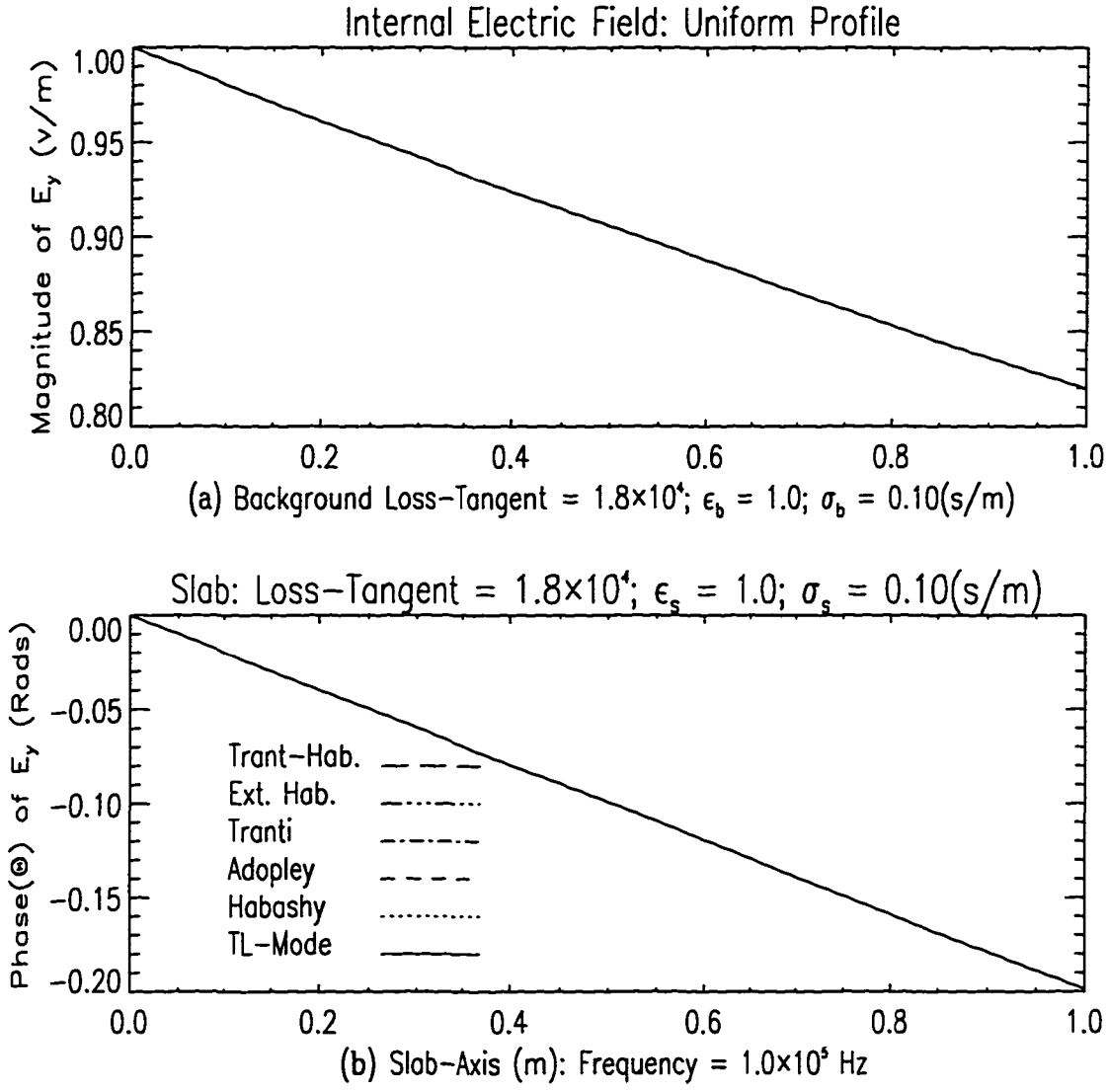

Figure 6.2: Magnitude and Phase Plots of Internal Electric Field.

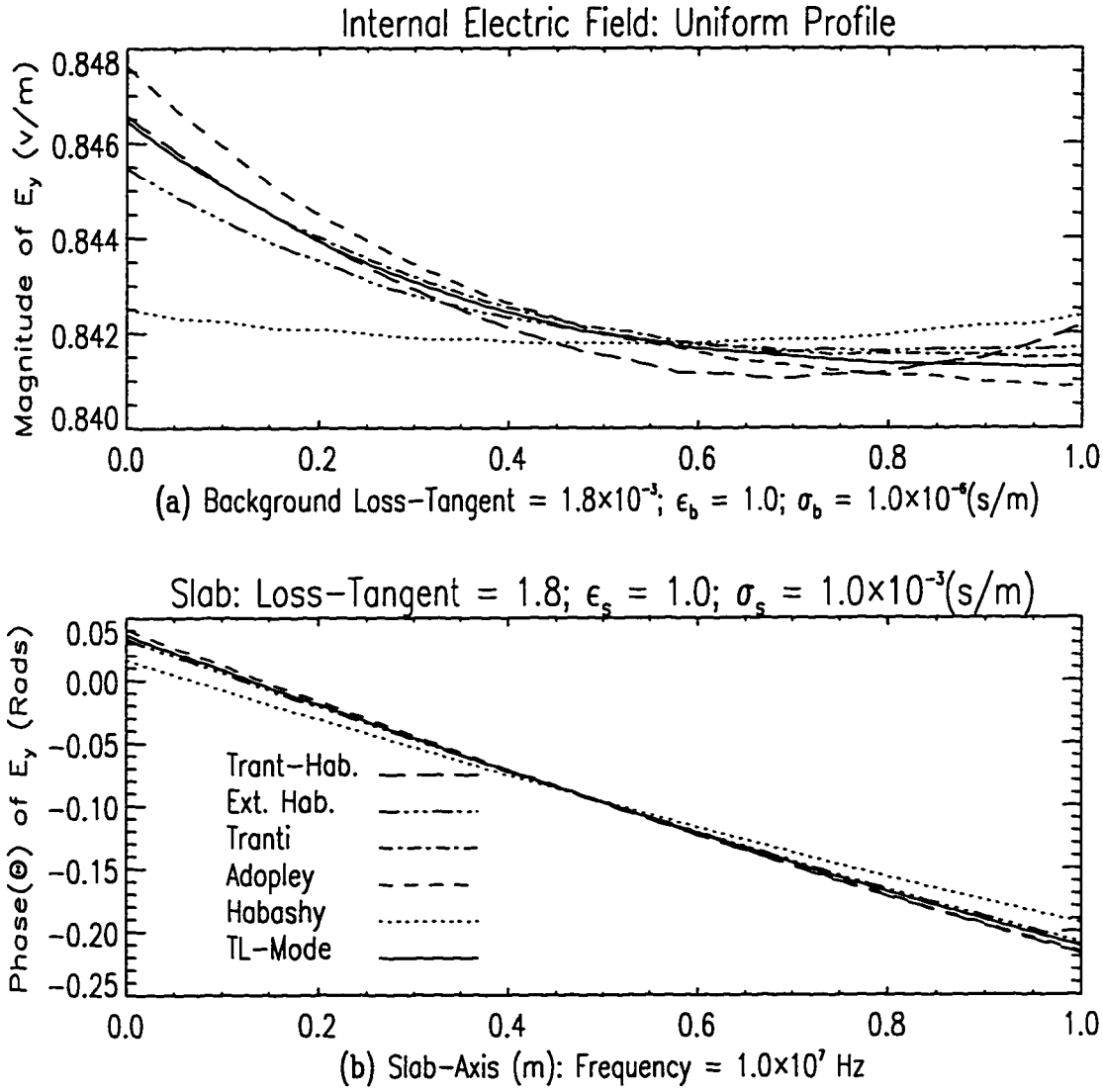

Figure 6.3: Effect of Background and Slab Loss-Tangents on Electric Field Accuracies

is 1.0. This gives a complex conductivity contrast of 10^3 between the homogeneous background medium and the slab. We note that the Habashy model provides the least accurate results. It underpredicts both the magnitude and phase of the electric field at the incident edge of the slab, while overpredicting at the transmission edge. The Trantanella model gives the best result, with perfect match at $z = 0$. We note also that the Extended Habashy model gives much better results than the Habashy model. These results are consistent with the predictions. In Section 6.1 we noted that the accuracy of the Habashy approximation for lossy systems demands that $\sigma_b \gg 0$. This condition is violated. The Adopley model gives slightly better results than the Habashy model. This is because of the Born approximation incorporated into the Adopley model. However the complex conductivity contrast is beyond the effective range of the Born approximation as given in [16]. The final trace is for the Trantanella-Habashy model. It is observed to give very accurate predictions at the leading edge of the slab. But the accuracy falls off as we approach the slab trailing edge. This is because in the formulation we computed the constant parameters using the tangential fields at the leading edge.

In Figure 6.4, we reverse the relative magnitude of the loss-tangents of the slab and homogeneous background medium from that of Figure 6.3. The Trantanella-Habashy model is the least accurate for the magnitude plots. In the phase plots, the Habashy model produced the least accurate results. From careful examination of Figures 6.3 and 6.4, we note that the sign of the errors for the Habashy models in Figure 6.3 are

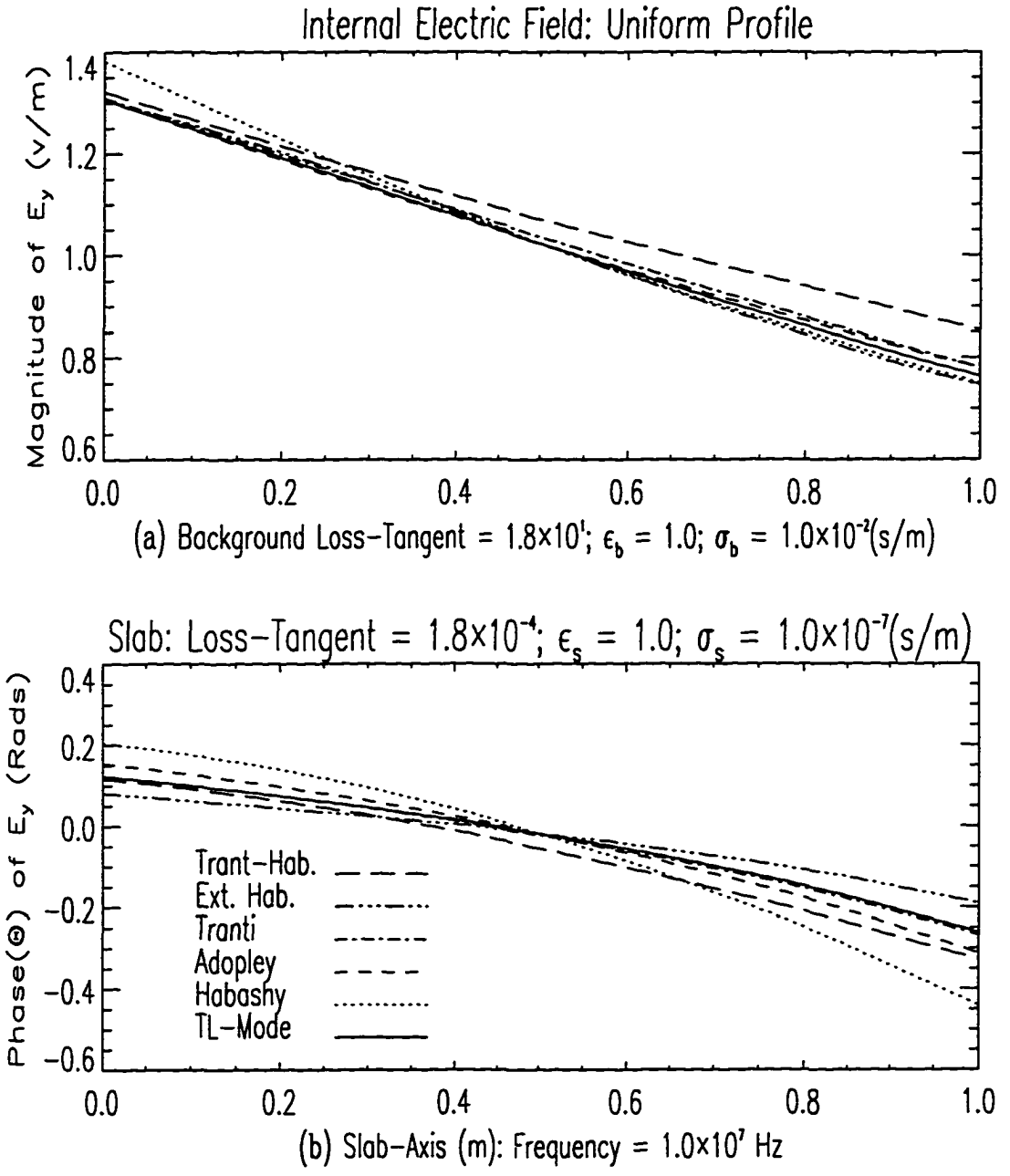

Figure 6.4: Effect of Relative Magnitude of Loss-Tangents on Electric Field Accuracies

the negative of those of Figure 6.4 at both the leading and trailing edges of the slab. We see that when the homogeneous background medium is less conductive than the slab, the Habashy model predicts lower values at the leading edge of the slab and higher values at the trailing edge in both magnitude and phase. The exact opposite is true if the homogeneous background medium is more conductive than the slab. As we expect, the Extended Habashy model is consistently more accurate than the Habashy model as predicted in Chapter 2.

In Figure 6.5 we increased the homogeneous background medium conductivity to 5.0 and that of the slab to 10.0. The frequency of simulation is also decreased from $10.0MHz$ to $0.10MHz$. The dielectric constants of the two media are kept at 1.0 without any change. We note the decrease in complex conductivity contrast from 10^3 to 2.0. In Figure 6.6, we use the same parameters as Figure 6.5, except that we reverse the conductivity contrast. The Habashy model shows better accuracy than the Adopley model for magnitude plots in Figure 6.5. In Figure 6.6 the magnitudes plots are more accurate for the Adopley model than the Habashy model as we reverse the conductivity contrast. As was noted earlier, the Extented Habashy results are more accurate for both magnitude and phase plots in Figures 6.5 and 6.6 than the Habashy results. In the phase plots of Figure 6.6, the Adopley model in fact gave more accurate results than the Trantanella model. The Trantanella-Habashy model continues to predict accurate results at the leading edge of the slab, but its prediction at the trailing edge is very poor. It seems to be a general trend for the Adopley

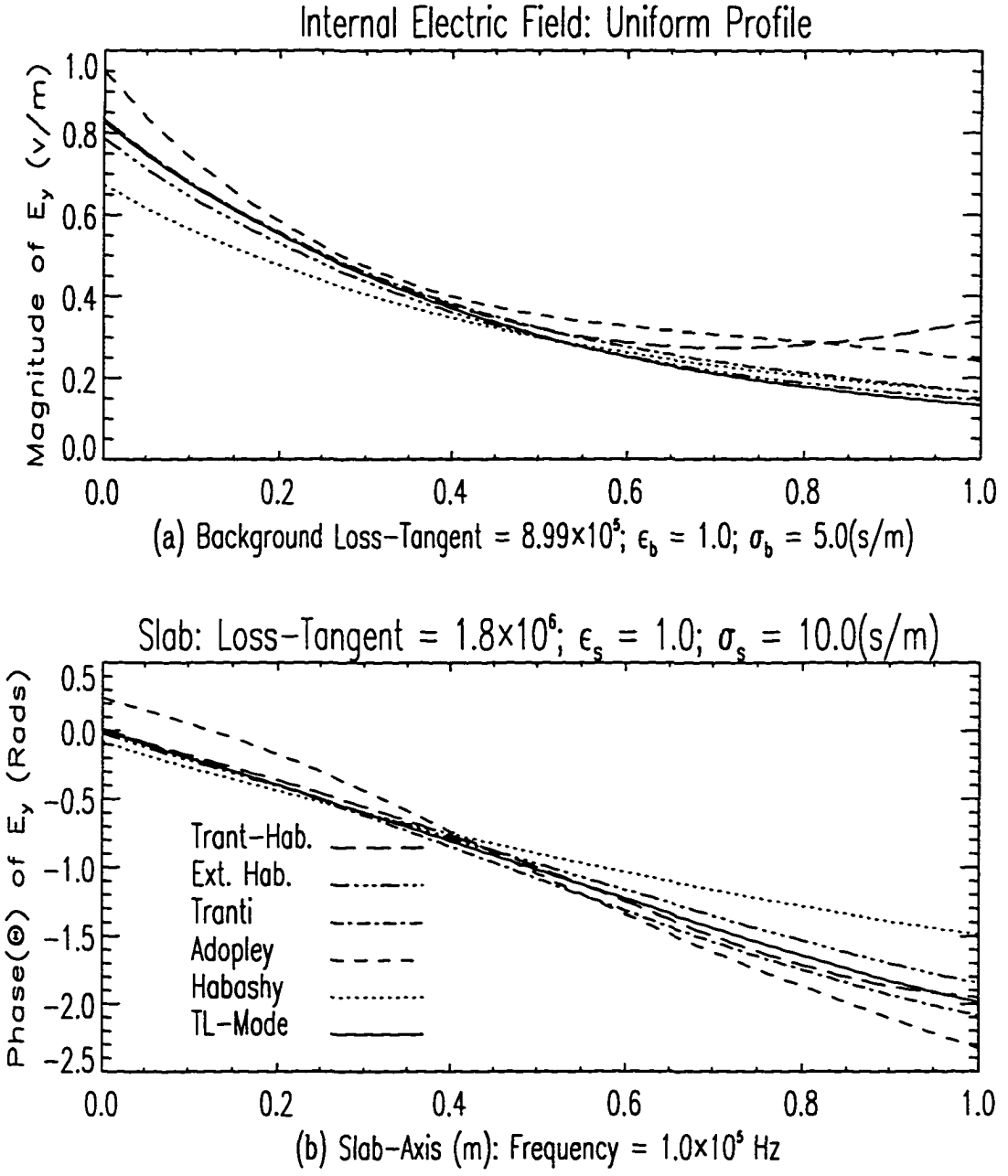

Figure 6.5: Effect of Absolute Magnitude of Loss-Tangents on Electric Field Accuracies

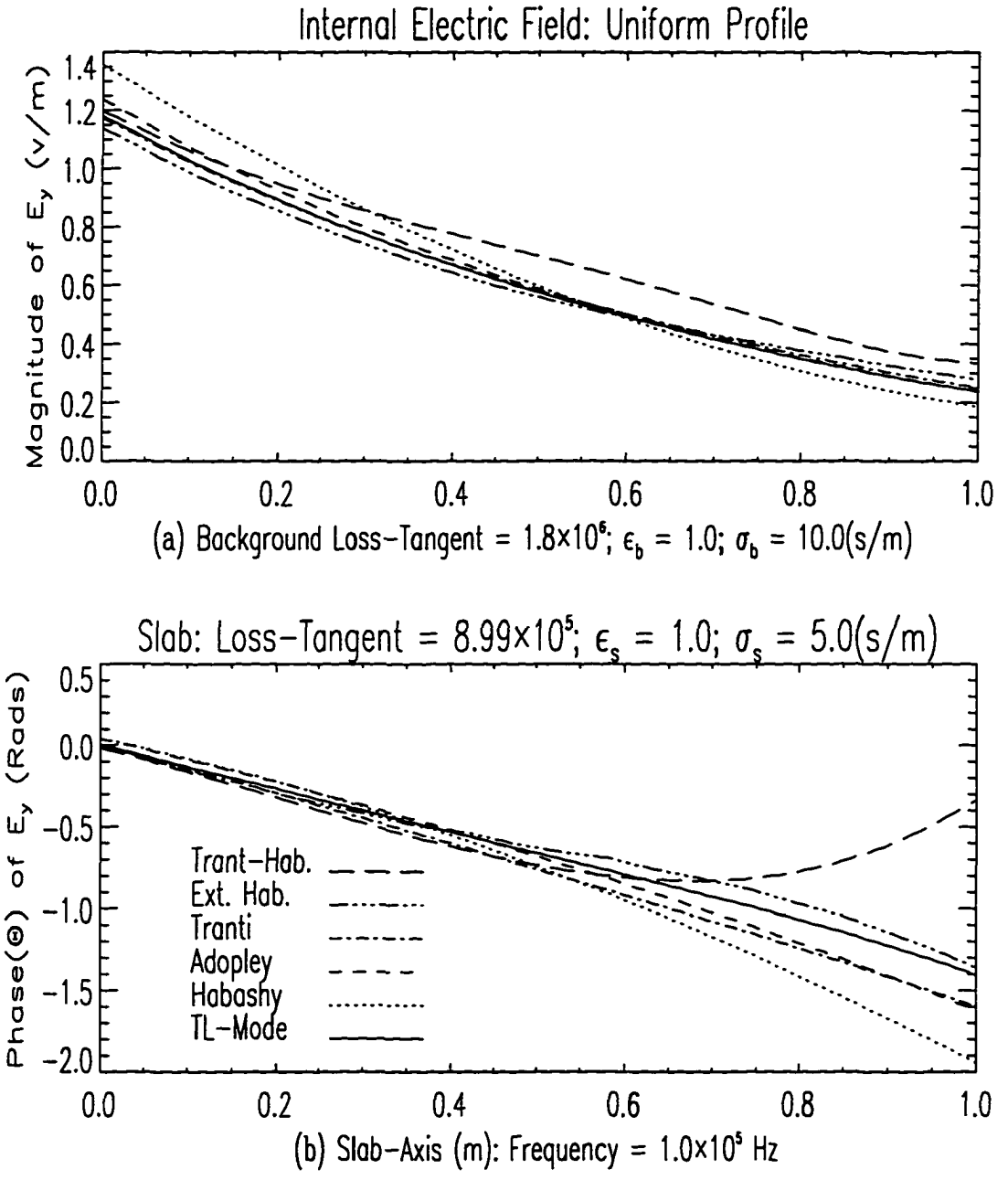

Figure 6.6: Effect of Relative Magnitude of Background Loss-Tangents on Electric Field Accuracies

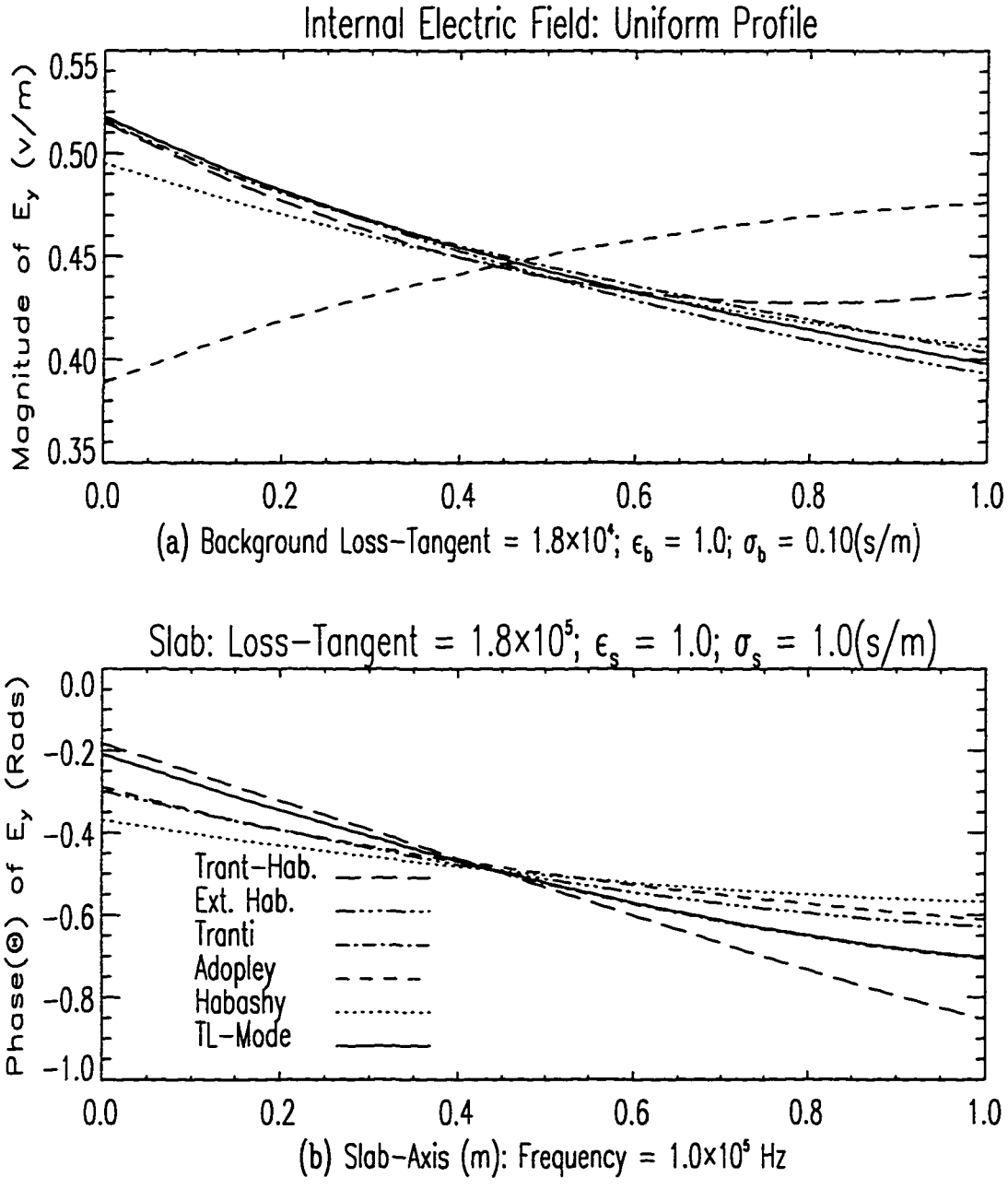

Figure 6.7: Effect of Slab Conductivity Contrast on Electric Field Accuracies

model to outperform the Habashy model when the homogeneous background medium is more conductive than the slab. In Figure 6.7 we set the background conductivity to $0.10s/m$ and that of the slab to $1.0s/m$. This increases the conductivity contrast between the slab and the background to 10.0. This is beyond the Born approximation. This produces very poor results of the Adopley model in the magnitude plots. However, the phase information from the Adopley model is competitive with the other models. The best results are provided by the Extended Habashy and Trantanella models. The magnitude and phase predictions from the Trantanella-Habashy model were consistently inferior to those of the Trantanella model for all the plots considered. Thus in subsequent investigations we have removed the Trantanella-Habashy model.

In the next set of investigations we simulate the boundary electric field using both the internal and the external approximate formulations. Of particular interest is the frequency range within which the internal formulations can be used to effectively simulate the boundary electric field. This stems from our observation that, apart from the Extended Habashy model, the expressions for the internal fields are available to us in an exact closed-form, unlike the external formulation which requires numerical integration. The use of the internal expression for the boundary field would therefore cut the computation cost in our inversion algorithm. At the same time we expect reduction in numerical noise from less computation. In Figure 6.8, we plotted the

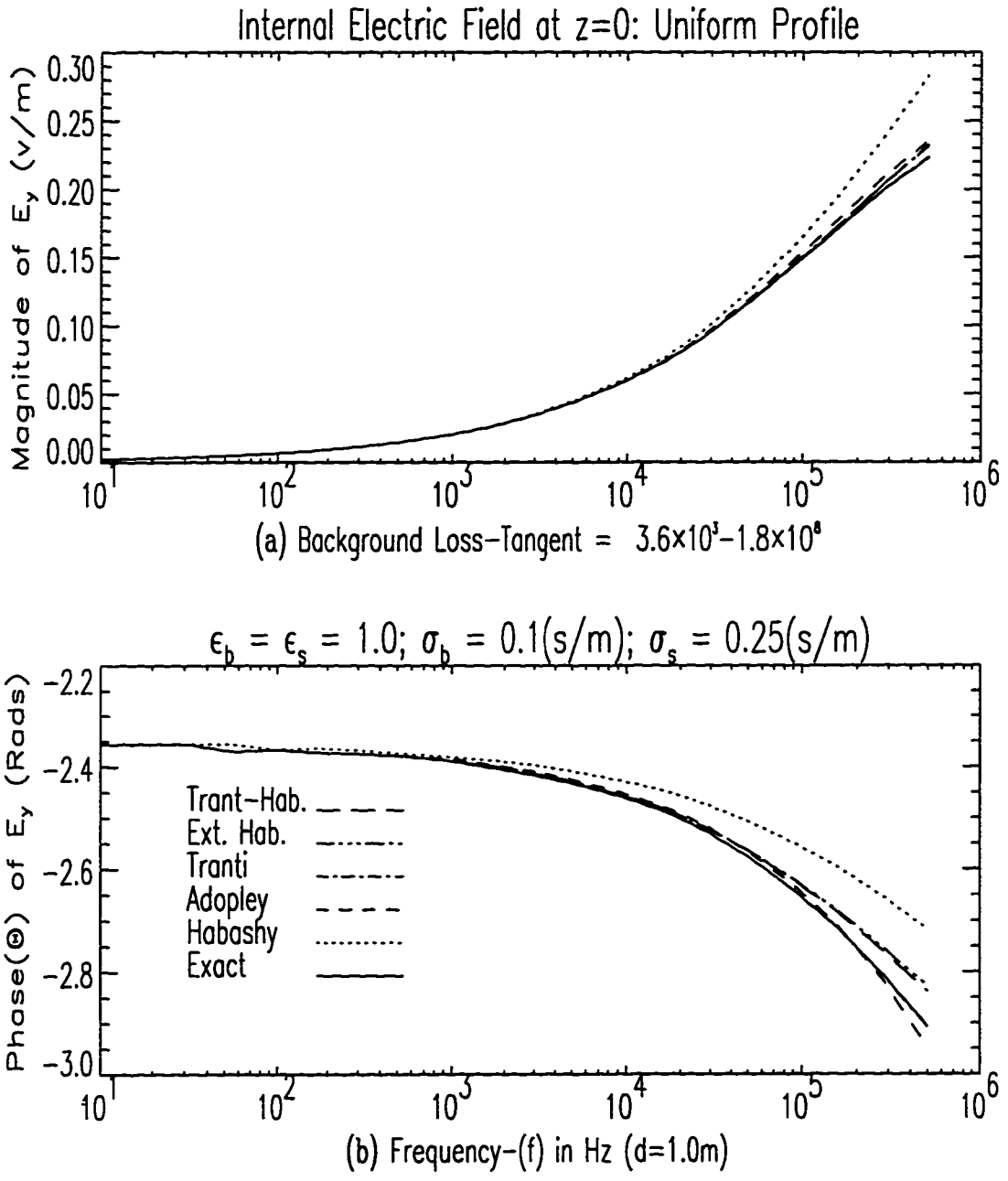

Figure 6.8: Frequency Dependence of Accuracies of the Electric Field

computed electric field at the boundary $z = 0$ as a function of frequency using the internal formulation. The dielectric constant and the conductivity of the homogeneous background are 1.0 and $0.10s/m$ respectively. The slab profile is the uniform type, with dielectric constant of 1.0 and conductivity of $0.25s/m$. The gives a complex conductivity contrast of 2.5. The range of the background loss-tangent is given on the figure to be 3.6×10^3 to 1.8×10^8. The maximum frequency of simulation is $0.5MHz$. Within acceptable numerical errors, we observe very good agreement from all models for frequencies below $0.1MHz$ except the Habashy model. The phase information from the Habashy model is poor. It is of interest to note that apart from the Trantanella model, the Adopley model gave the best phase information. It is also of interest to notice that even though the Trantanella-Habashy model was derived by matching tangential fields at the incident boundary ($z = 0$), the Adopley model still gave better results. In Figure 6.9 we increased the conductivity contrast from 2.5 to 10.0 by increasing the conductivity of the slab from $0.25s/m$ to $1.0s/m$. We observe a drop in the frequency range for accurate simulation. The Trantanella formulation gives the best results in field magnitude information. However we notice a rapid degradation in phase information at frequencies above $0.317MHz$. The magnitude information is better for the Habashy model compared to the Adopley model. This is in contrast to the results of Figure 6.8. Generally, we observed from our numerical

simulations that for high conductivity contrasts, the Habashy model predicted better results at least in the field magnitude information. This is consistent with our expectations from Chapter 2.

In many practical situations, the exact location of the slab boundary is not available as a priori information. In the next set of investigations, we therefore placed the slab boundary at points that are not necessarily the physical boundary of the slab; indeed we allowed for the extension of the background media into the slab region. In Figure 6.10, the background extends midway into the slab. This is the "Right-Step" profile type shown in Figure 6.1. The background and the slab parameters are the same as used in Figure 6.8. We note accurate field prediction from all models except the Habashy model, within the frequency ranges considered. Also comparing the results of Figure 6.10 against that of Figure 6.8, we note that the results of Figure 6.10 are more accurate. This is expected from the fact that the effective slab size is smaller in Figure 6.10. However we notice a divergence in phase information from the Adopley model. The Habashy model showed increasing error at the higher frequencies particularly in the magnitude plot.

Figure 6.11 shows the results of the "inclusion" slab profile where the slab is located symmetrically within the measurement boundaries. The parameters for the background and the slab are the same as those of Figure 6.10. The Habashy model gave poor results with error in predicted values increasing with frequency. The rest of the models predicted almost perfect results in the magnitude information. In the

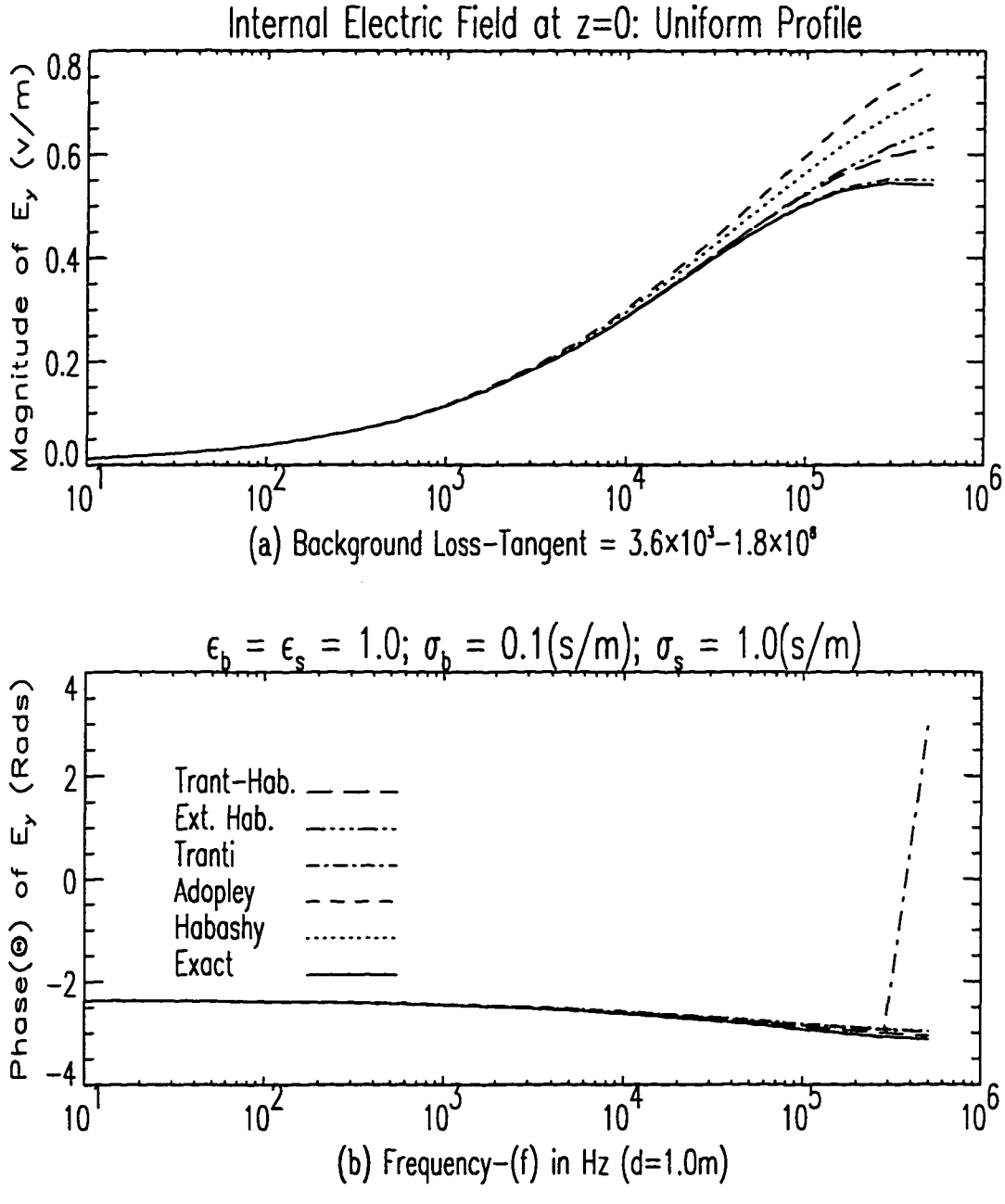

Figure 6.9: Effect of Slab Conductivity Contrast on Frequency Dependence

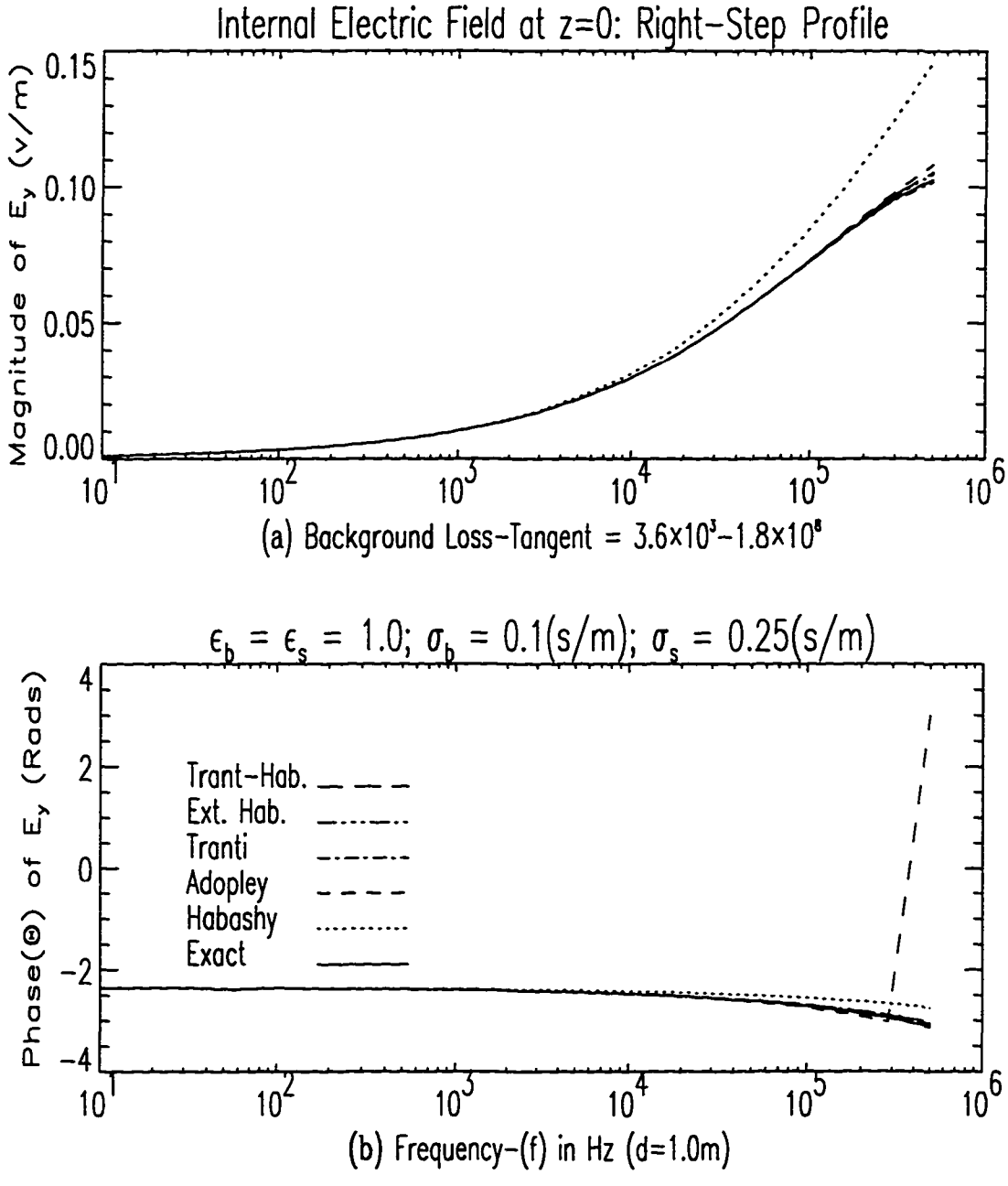

Figure 6.10: Effect of Measurement Boundaries on Frequency Dependence

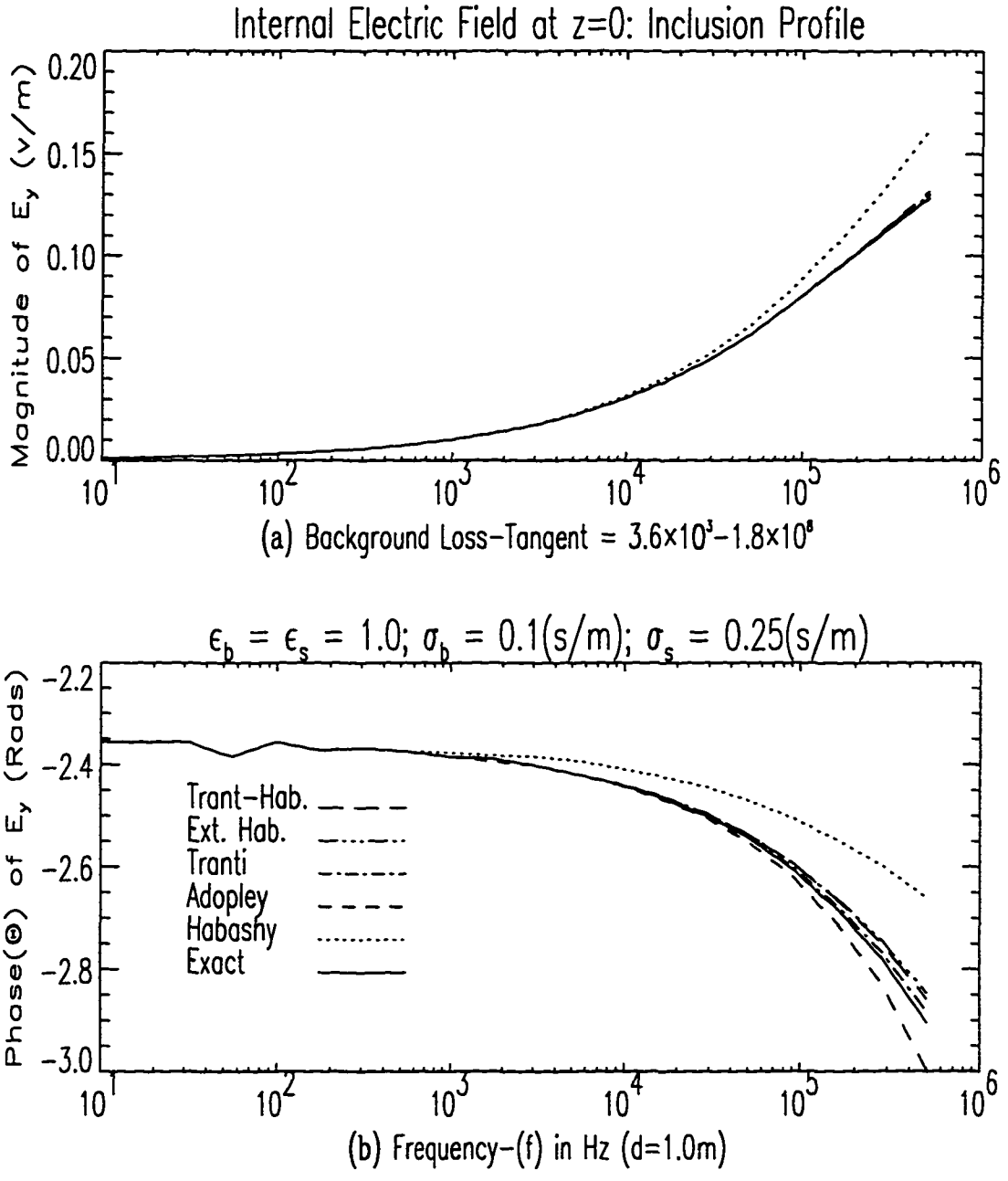

Figure 6.11: Effect of Measurement Boundaries on Frequency Dependence

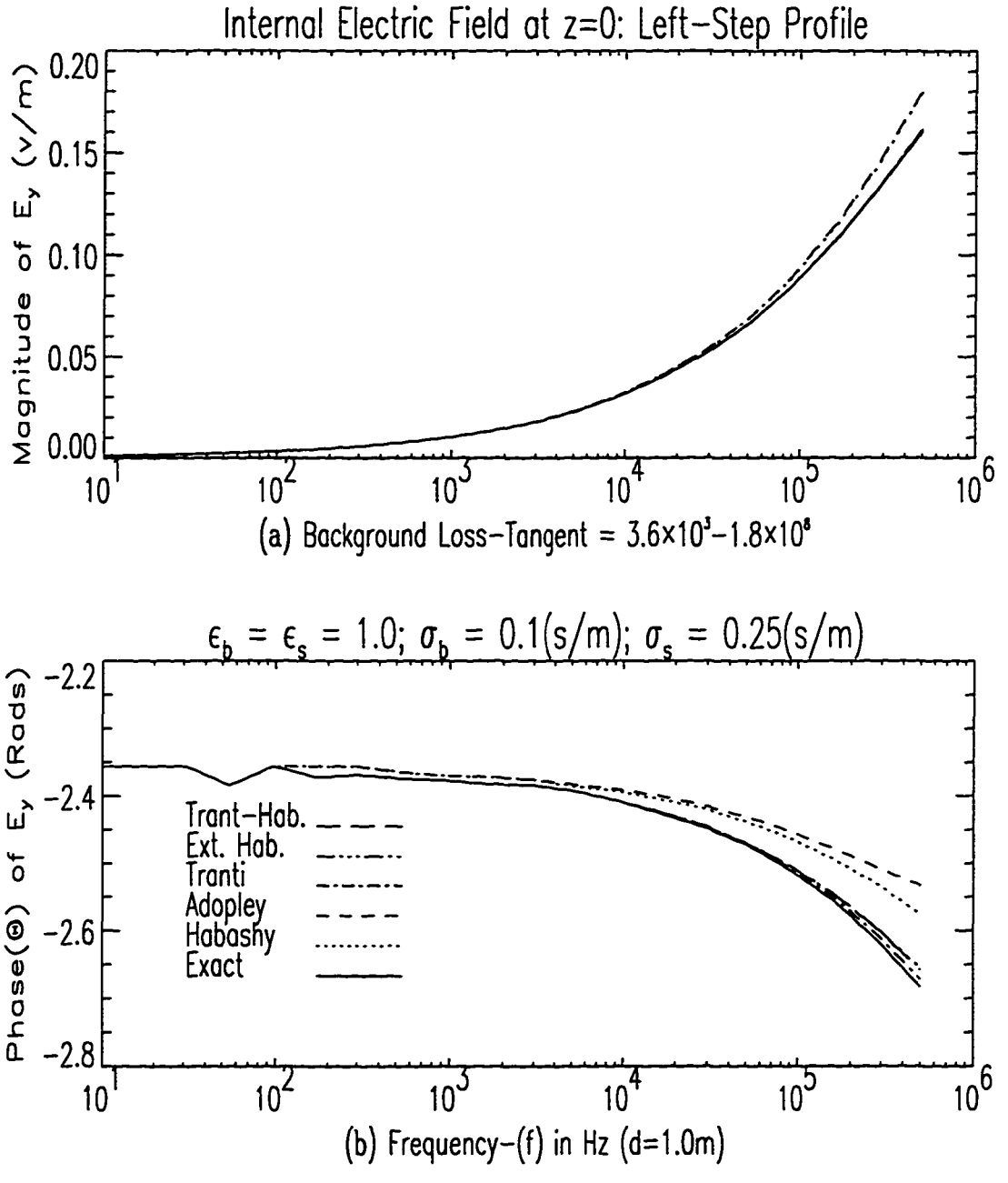

Figure 6.12: Effect of Measurement Boundaries on Frequency Dependence

phase plot, the Adopley model shows some deviations for frequencies above $0.1MHz$. Once again as expected, the results are better than those of the uniform profile.

The results of a "left-step" profile are shown in Figure 6.12 where the slab extends from the incident edge ($z = 0$) and ends midway in the measurement region. The parameters used are the same as those for the previous profiles. While the Habashy model shows a slight improvement in the magnitude plots, we notice a decrease in accuracy for the Adopley model. The phase information from the Adopley and Habashy models are very poor. In this particular case, we can consider the phase information lost for the two models. It appears to be generally true from Figure 6.12 and from extensive numerical investigations that when the observation point at $z = 0$ coincides with the slab boundary and there is a discontinuity within the slab, the phase information from the Adopley model is usually very poor.

6.2.2 External Scattered Electric Field

The next set of numerical simulations is for the electric field at the boundaries $z = 0$ and $z = d$ using the external formulation. We computed the integrals of the approximations numerically using 10-point Gaussian quadrature. In Figure 6.13 we plot the magnitude and phase of the scattered electric fields at the boundary $z = 0$. The parameters for the homogeneous background and the slab media are the same as those employed in Figure 6.8. The maximum frequency of simulation however is increased to $1.0MHz$. We notice much higher accuracy from the external formulation.

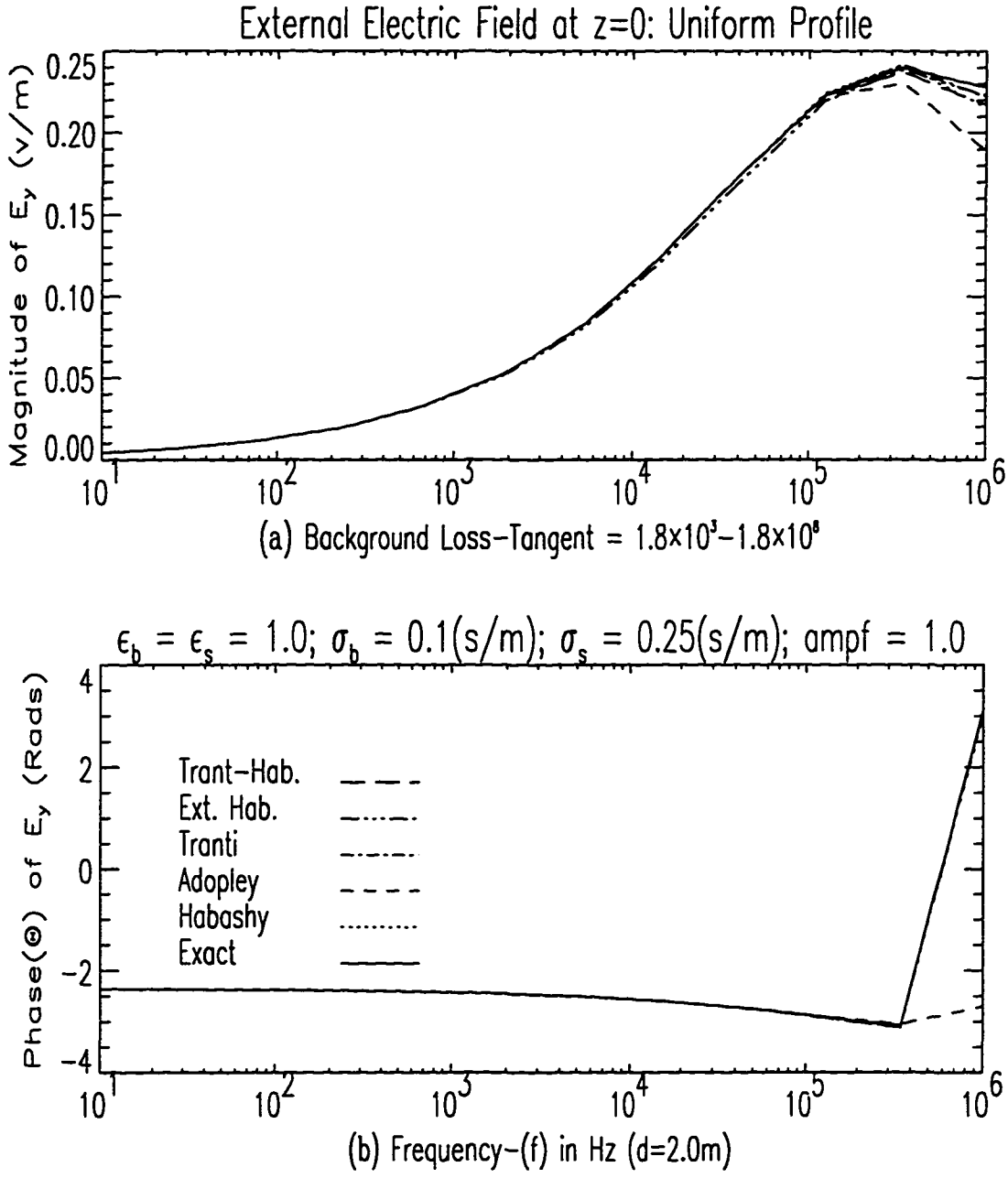

Figure 6.13: Accuracy of Approximations

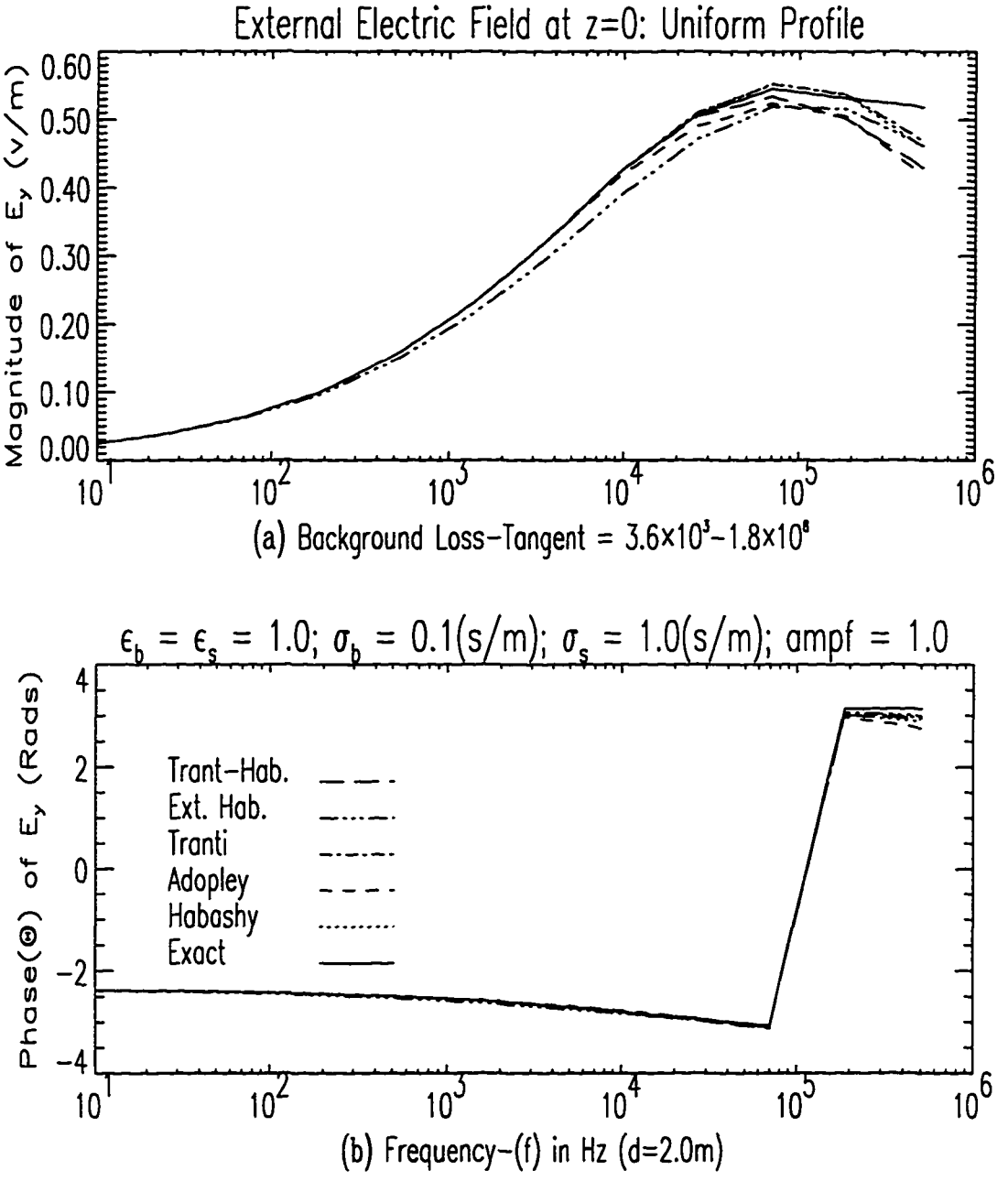

Figure 6.14: Effect of Complex σ Contrast on Electric Field Accuracy

All the models were very accurate in the magnitude plots except the Adopley model, which shows some error at frequencies above $3.1623 \times 10^5 Hz$. The Adopley model also shows phase error above the same frequency of $3.1623 \times 10^5 Hz$. The rest of the models gave perfect phase information. In Figure 6.14 we simulated the scattered field at $z = 0$ using the same parameters as in Figure 6.9. As was noted from the internal field simulations at $z = 0$, the accuracy of the Adopley model decreases with increase in complex conductivity contrast. We note from this particular plot that the Habashy and Trantanella models gave the best information both on magnitude and phase. It is of interest to note that the Habashy model actually performed better than the Extended Habashy model. This is contrary to what was predicted in Chapter 2. However we note that the Extended Habashy model is the only model without an analytical closed-form solution for the internal fields. Thus the repeated numerical integration in the Extended Habashy model has amplified the numerical noise, compromising its accuracy.

Apart from uniform slab partitioning, we also used what we called "uneven element" partitioning in addition to uniform partitioning. Contrary to uniform partitioning in which each partition element is of the same size, in the "uneven element" partitioning the $(n+1)^{th}$ element size is α *times* the n^{th} element size for $n = 1, 2 \cdots N$, where α is a fixed constant called *amplification factor*. We note that when the amplification factor is 1, we recover the uniform partitioning. The effect of amplification

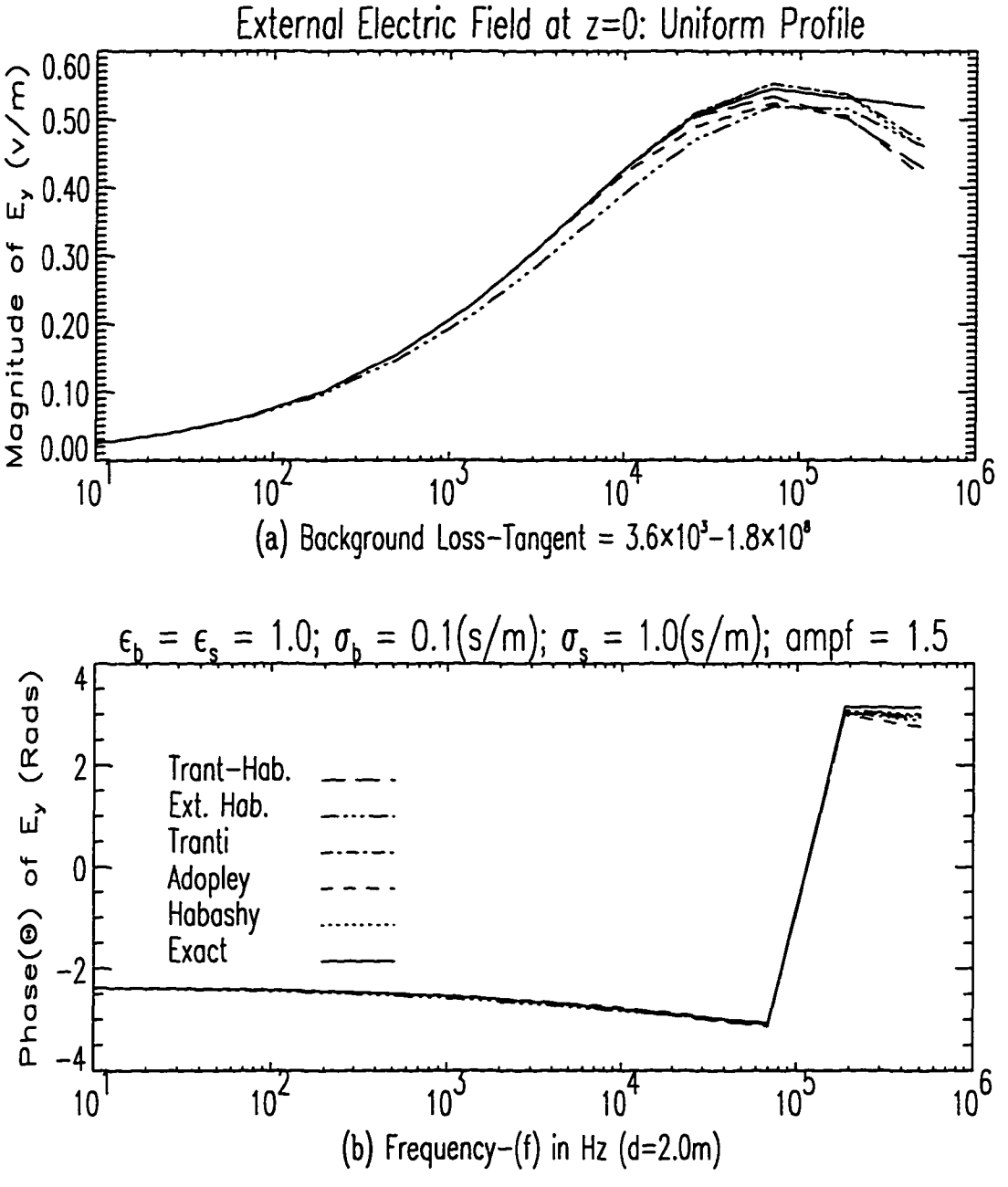

Figure 6.15: Effect of Slab Element Size on Electric Field Accuracy

factor in the "uneven element" partitioned slab is shown in Figure 6.15. The homogeneous background and slab parameters are the same as those of Figure 6.14. The element amplification factor is set at 1.5. There is no noticeable difference between the plots in Figures 6.14 and 6.15. However, from other numerical investigations the element amplification factors tend to increase model accuracies for "uniform" profiles. We wish to state that the uneven partitioning was restricted to "uniform" profiles only. This is because, it was very difficult to fix the slab profile boundaries at the same z locations as we vary the *amplification factor* for the other profile types. The amplification factor used is selected from numerical experimentations. It is generally true that very high amplification factor values tend to initial instability in the models.

All the investigations we conducted next are for the uniform element partitioning where the element amplification factor is 1.0. Results from "Left-Step", "Right-Step" and "Inclusion" profiles are shown in Figures 6.16, 6.17 and 6.18, respectively. The parameters used are the same as those for Figure 6.10 with the exception that d in the external field investigations is twice the d used for the internal fields. The profile size is $1/2d$ as shown in Figure 6.1. As shown in the plots, the accuracies are better for both magnitude and phase information than the corresponding "Uniform" profile. This is predicted by the theory from the effective smaller profile size. Of particular interest are the predictions from the Trantanella and Trantanella-Habashy model. It is surprising that even though these two approximations were formulated by matching the tangential fields at the boundary $z = 0$, they were least accurate for the

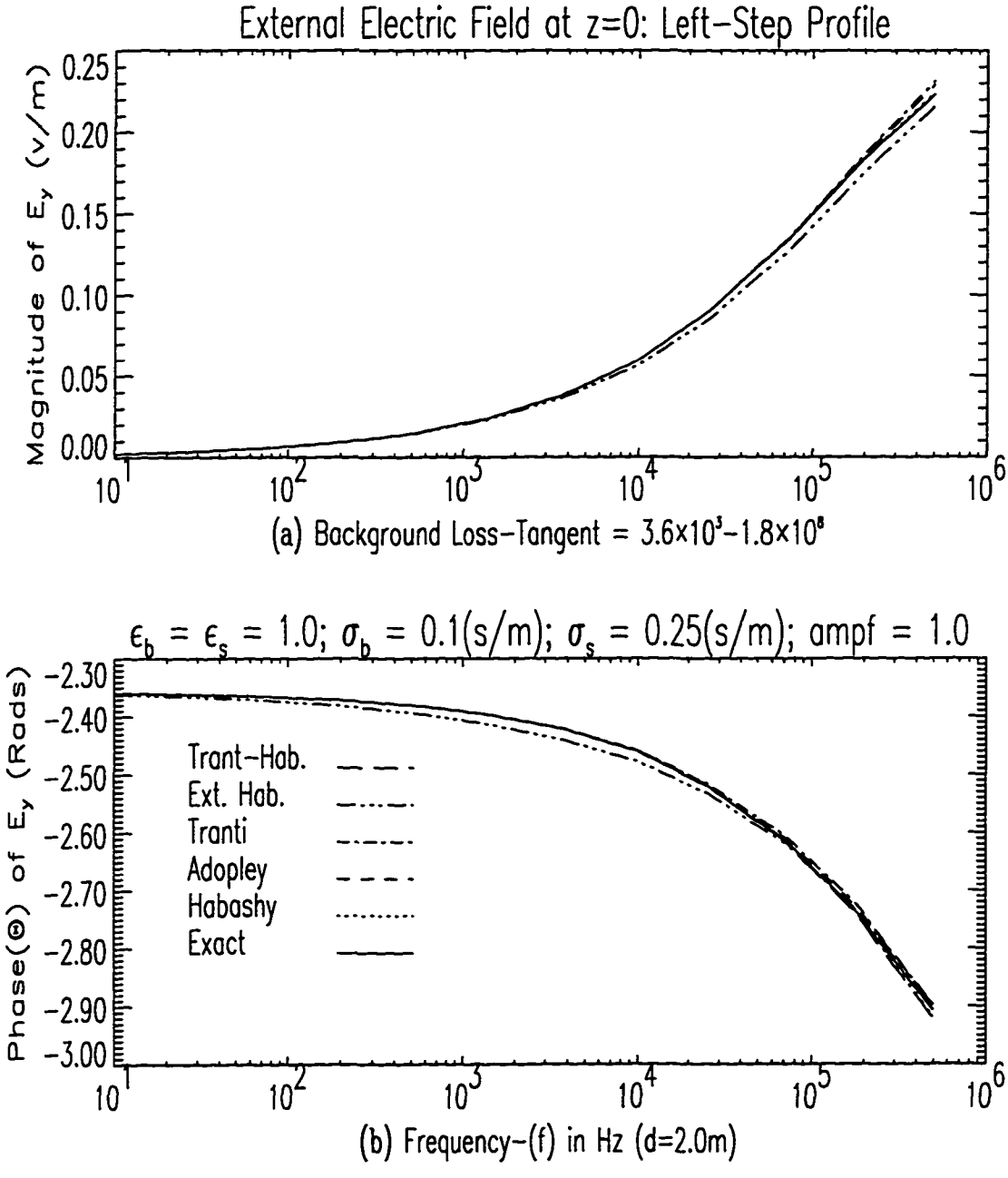

Figure 6.16: Effect of Slab Element Size on Electric Field Accuracy ($z = 0$)

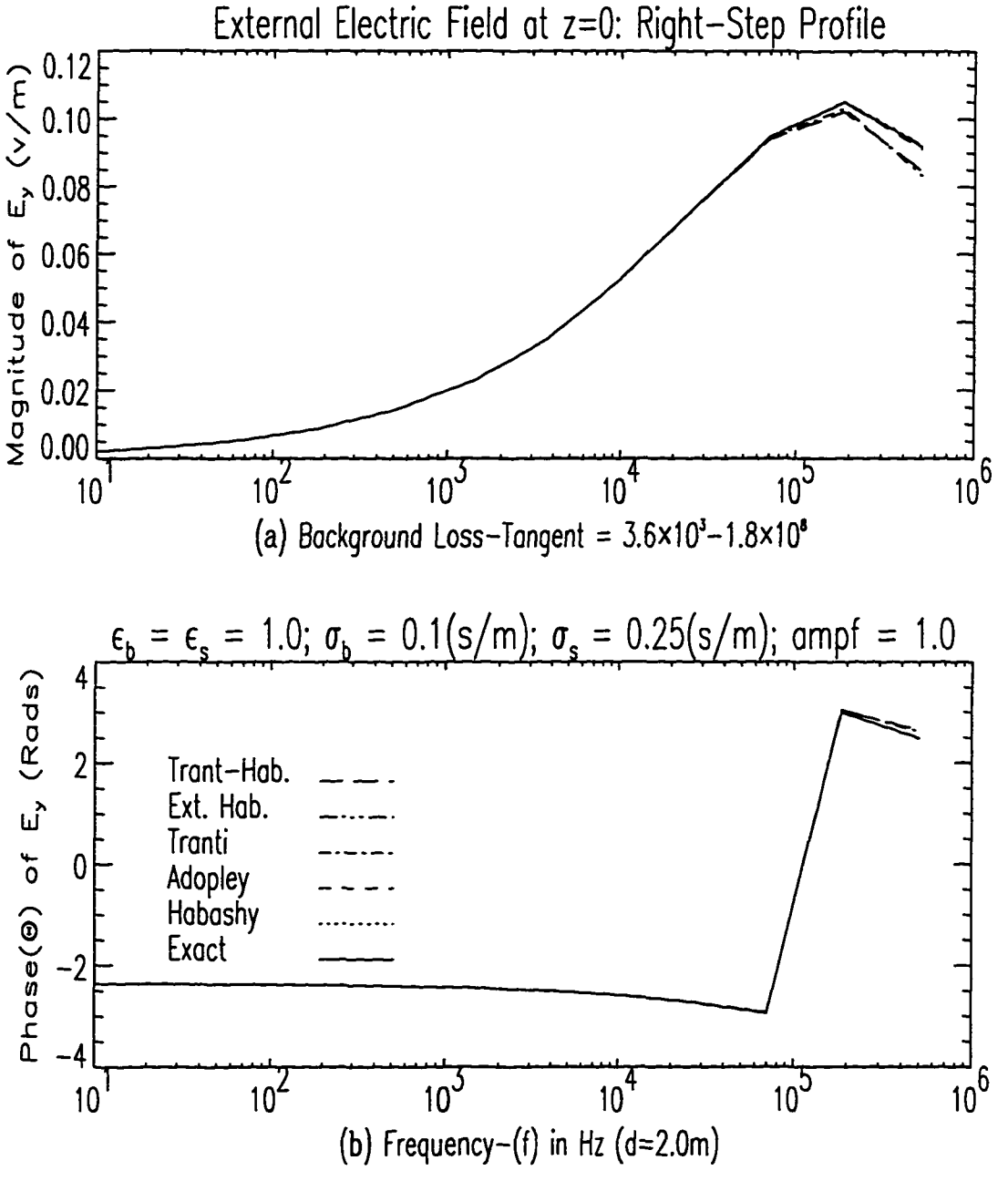

Figure 6.17: Effect of Slab Element Size on Electric Field Accuracy ($z = 0$)

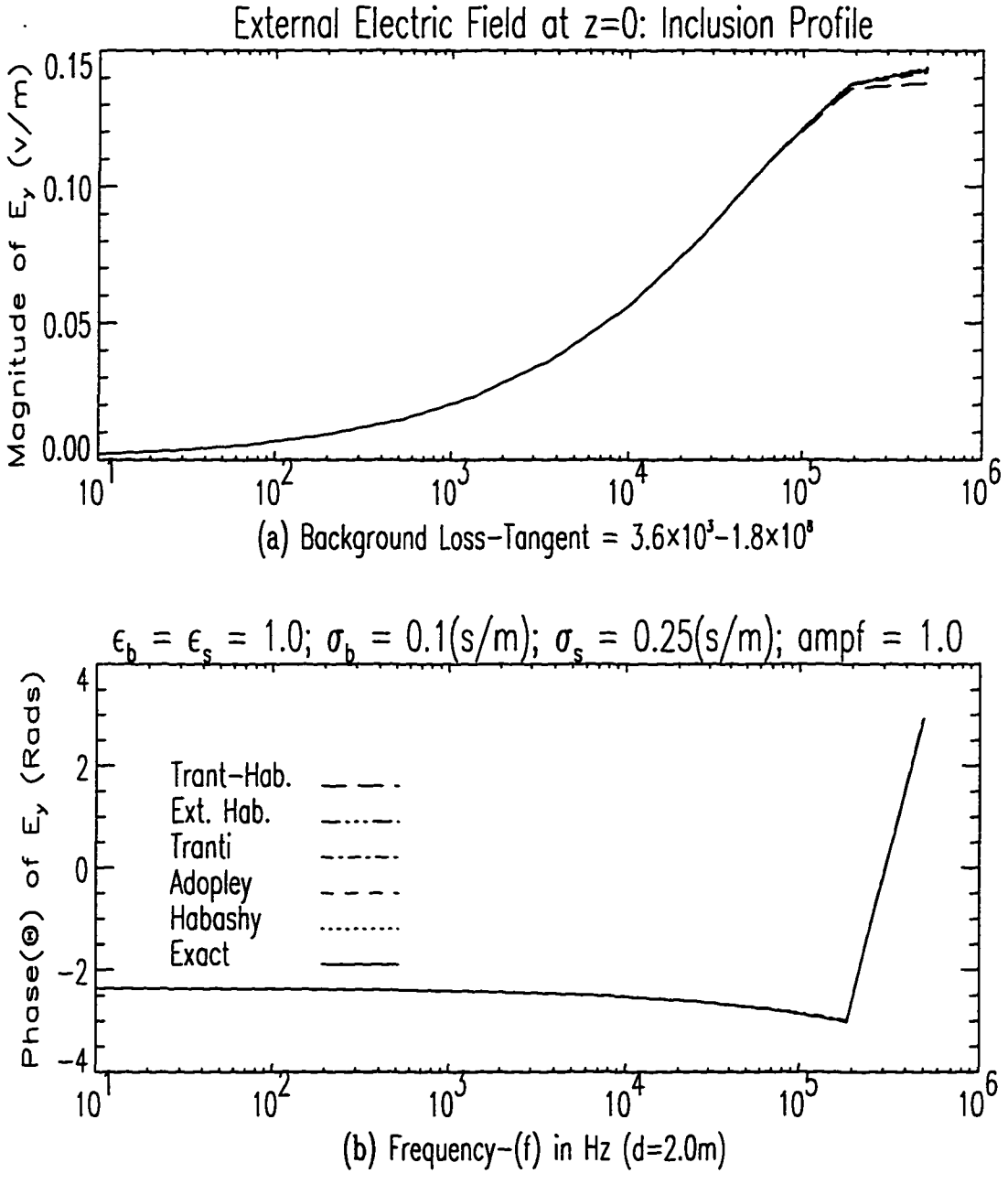

Figure 6.18: Effect of Slab Element Size on Electric Field Accuracy ($z = 0$)

"Right-Step" profile. Our only possible explanation is the fact that the measurement boundary at $z = 0$ is not the actual slab boundary which is halfway between the measurement boundaries, $z = 0$ and $z = d$.

The results from a reverse "Left-Step" profile are shown in Figure 6.19. The homogeneous background parameters are the same as before. For this particular profile, the background extends halfway into the measurement region and ends at $z = d/2$. The measurement region from $z = d/2$ to $z = d$ has conductivity of $0.05s/m$ which is below the background value of $0.10s/m$. Apart from the Trantanella and the Trantanella-Habashy models, all models predicted perfect results for both magnitude and phase information. The Trantanella model shows instability for frequencies above $3.1623 \times 10^5 Hz$. From numerical investigation, we found that, for this particular set of parameters,

$$Q(2k_b)\left(1 - \frac{k_b}{2j\epsilon_b} dq_{av}\right) - \chi \tag{6.1}$$

in equation 3.28 of the Trantanella approximation assumes a minimum value in magnitude at the frequency of $2.26^6 Hz$. This is a direct consequence of the basic assumption made by Trantanella that the slab profile can be approximated by its average values in the double integral computation. This allowed Trantanella to evaluate the double integrals analytically. The last two plots on the piecewise constant profile are shown in Figures 6.20 and 6.21. The parameters employed are those of Figures 6.13 and 6.14 respectively. The only difference is that the fields are computed at the boundary $z = d$. In Figure 6.20 where the complex conductivity contrast is only

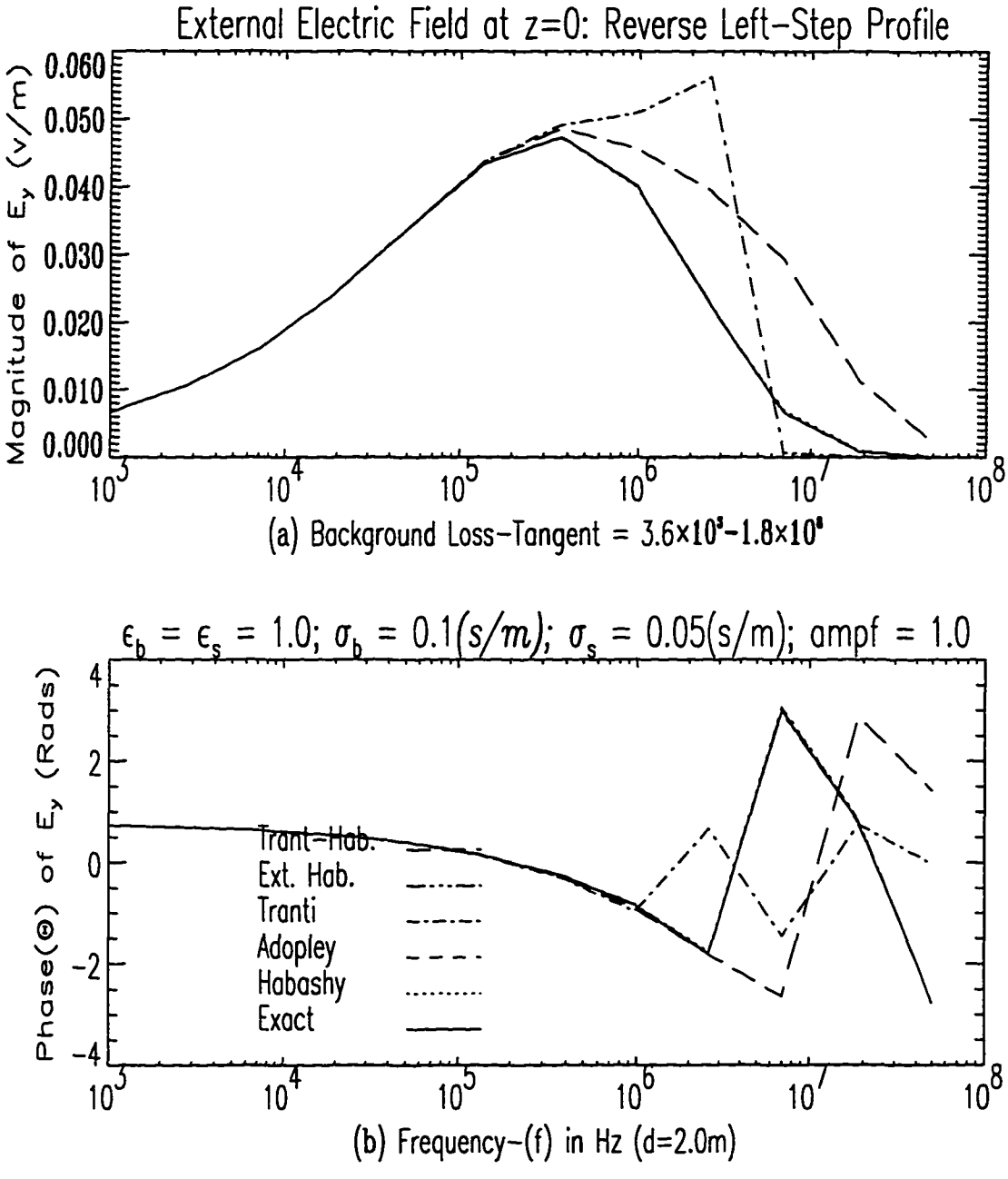

Figure 6.19: Effect of Relative Position of Observation Point and Slab Boundary on Electric Field Accuracy ($z = 0$)

2.5 all the models predicted very good results. However as the complex conductivity contrast is increased to 10.0, all models begin to show some error at high frequencies. The Habashy model, emerges as the best model, outperforming the Extended Habashy.

6.3 Linear Profiles

The last set of plots are for the linear conductivity profile. The plots will be for the total internal field and the scattered external field on the slab boundaries. Because of computation difficulties in evaluating *Airy* functions with complex arguments, we shall perform absolute comparisons for the approximations only for the lossless slab. For the lossy slab, the comparisons will be limited to relative evaluation of the approximations.

6.3.1 Internal Electric Field

In the first group of these simulation results, shown in Figures 6.22-6.26, we limit ourselves to the lossless slab cases only. These are compared against the exact closed-form solution. It is of no surprise to note in Figure 6.22 that the Habashy formulation produced the least accurate results, especially in the field magnitude plots. For $\epsilon -$ slope of 0.5, all approximations except the Habashy model predict the internal electric field very accurately both in magnitude and phase. When $\epsilon-$slope is increased to 1.0 we observe a slight decrease in accuracy for the Extended Habashy model in

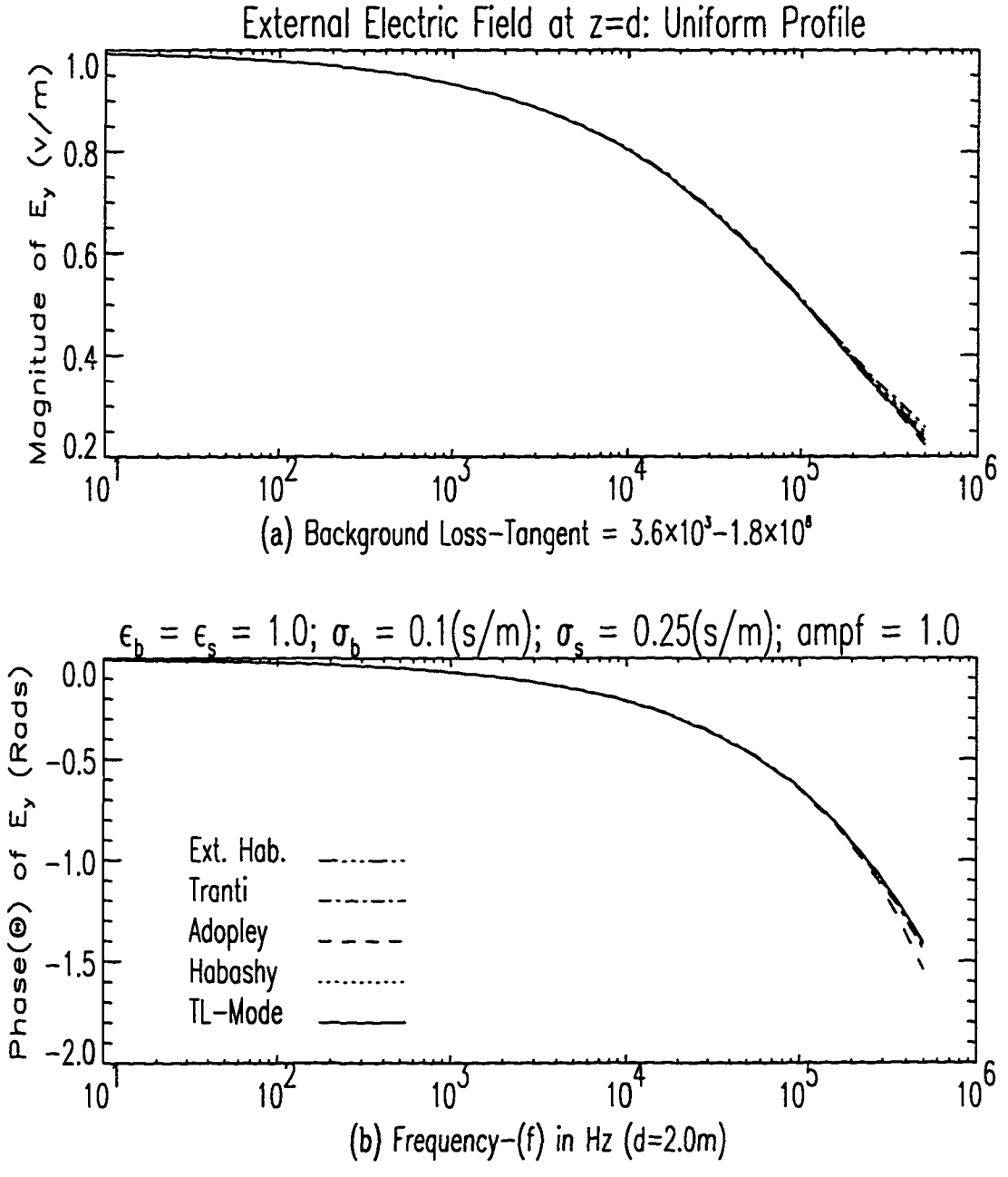

Figure 6.20: Effect of Relative Position of Observation Point and Slab Boundary on Electric Field Accuracy ($z = d$)

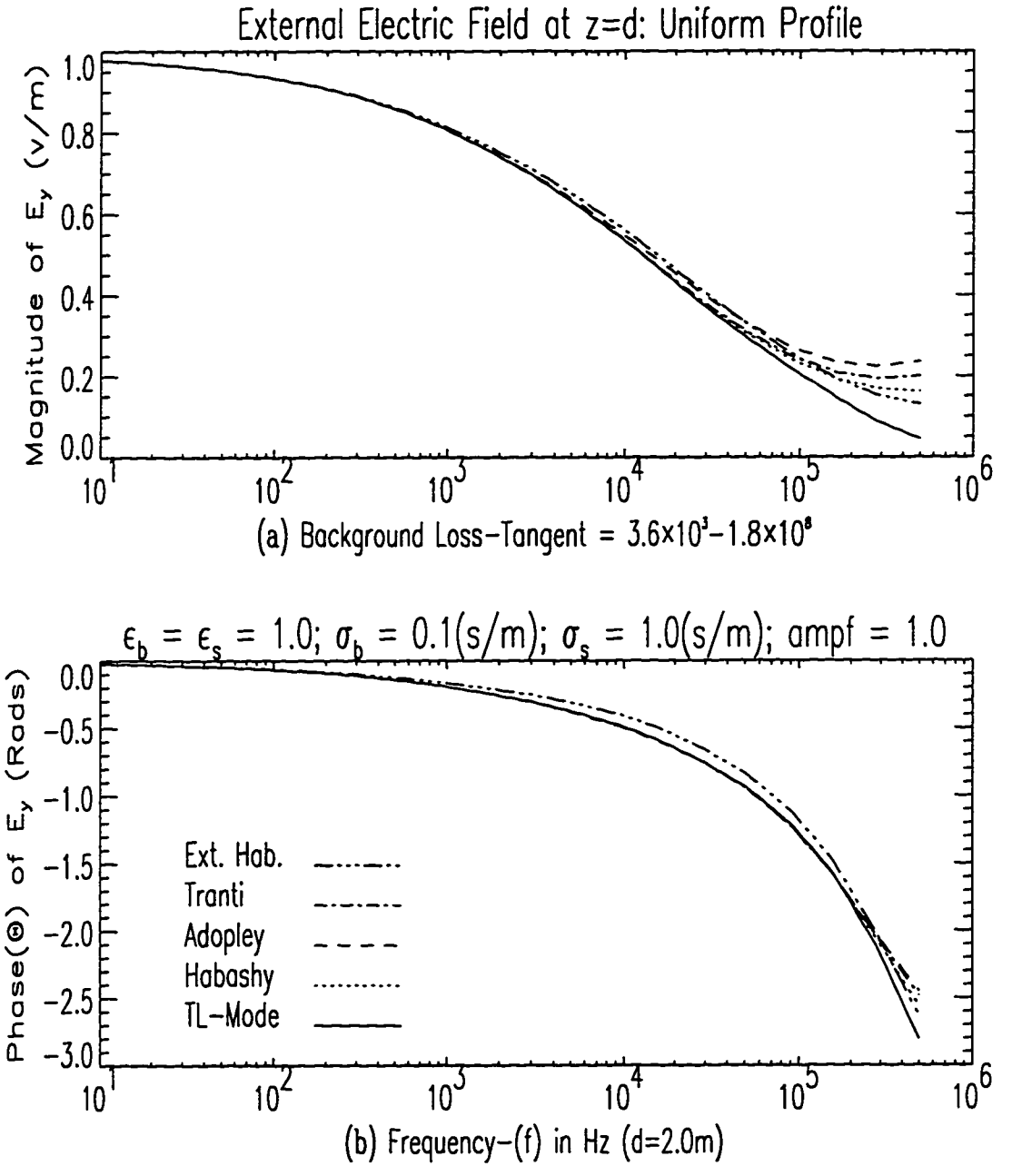

Figure 6.21: Effect of Position of Observation Point and Slab Boundary on Electric Field Accuracy ($z = d$)

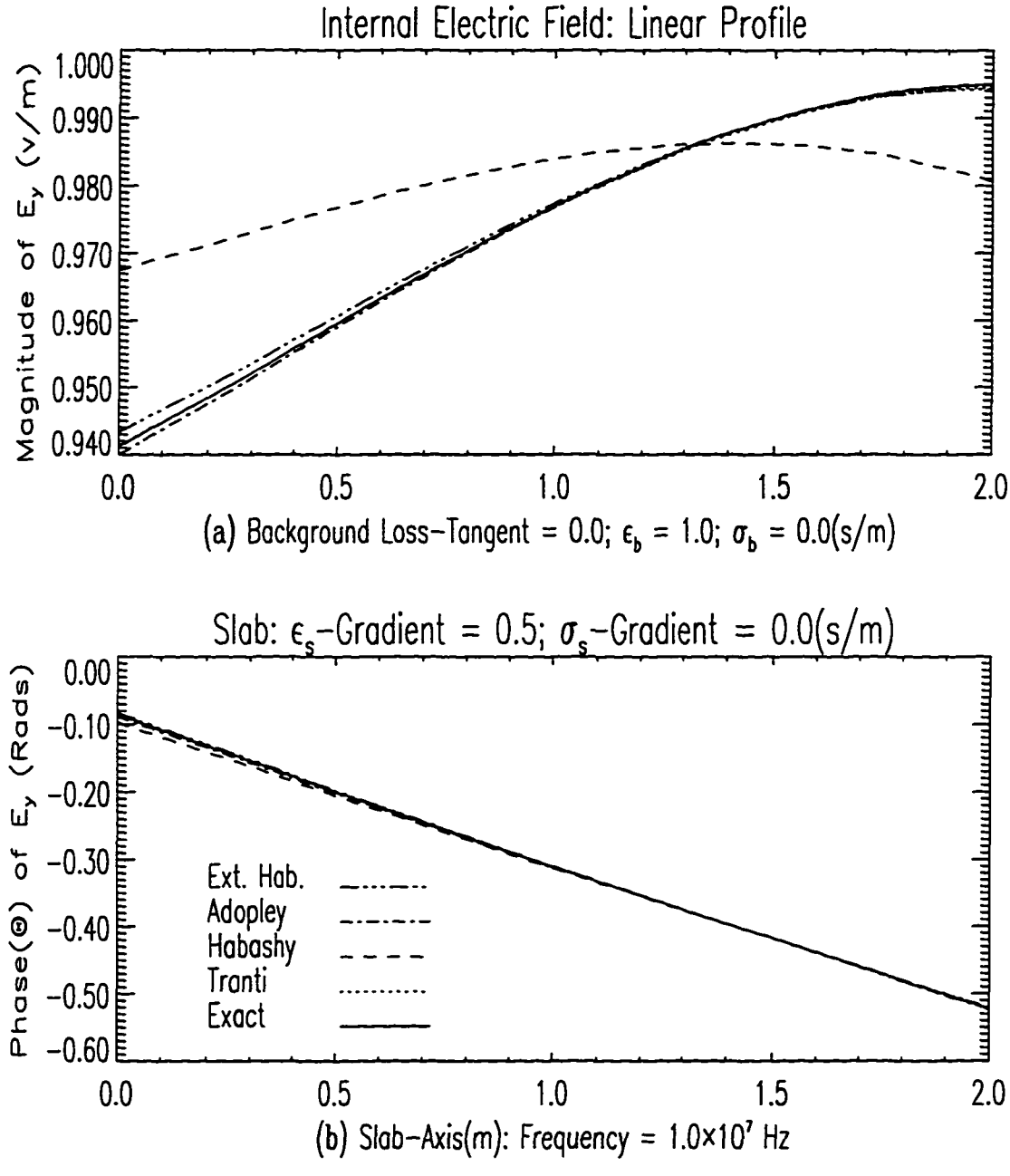

Figure 6.22: Magnitude and Phase Plots of Internal Electric Field in Lossless Slab with Linear Profile

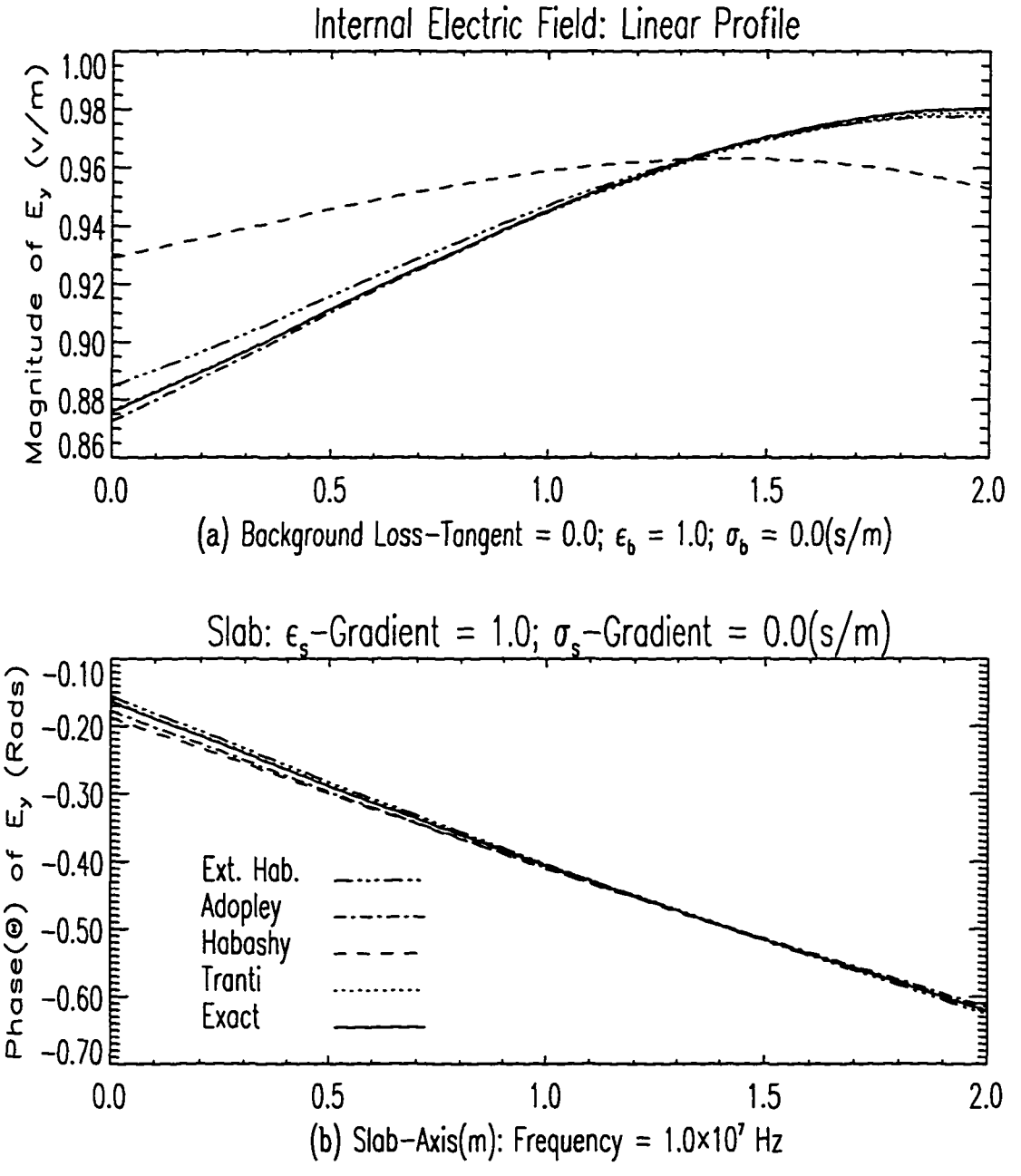

Figure 6.23: Effect of Increasing Dielectric Constant Gradient on Internal Electric Field

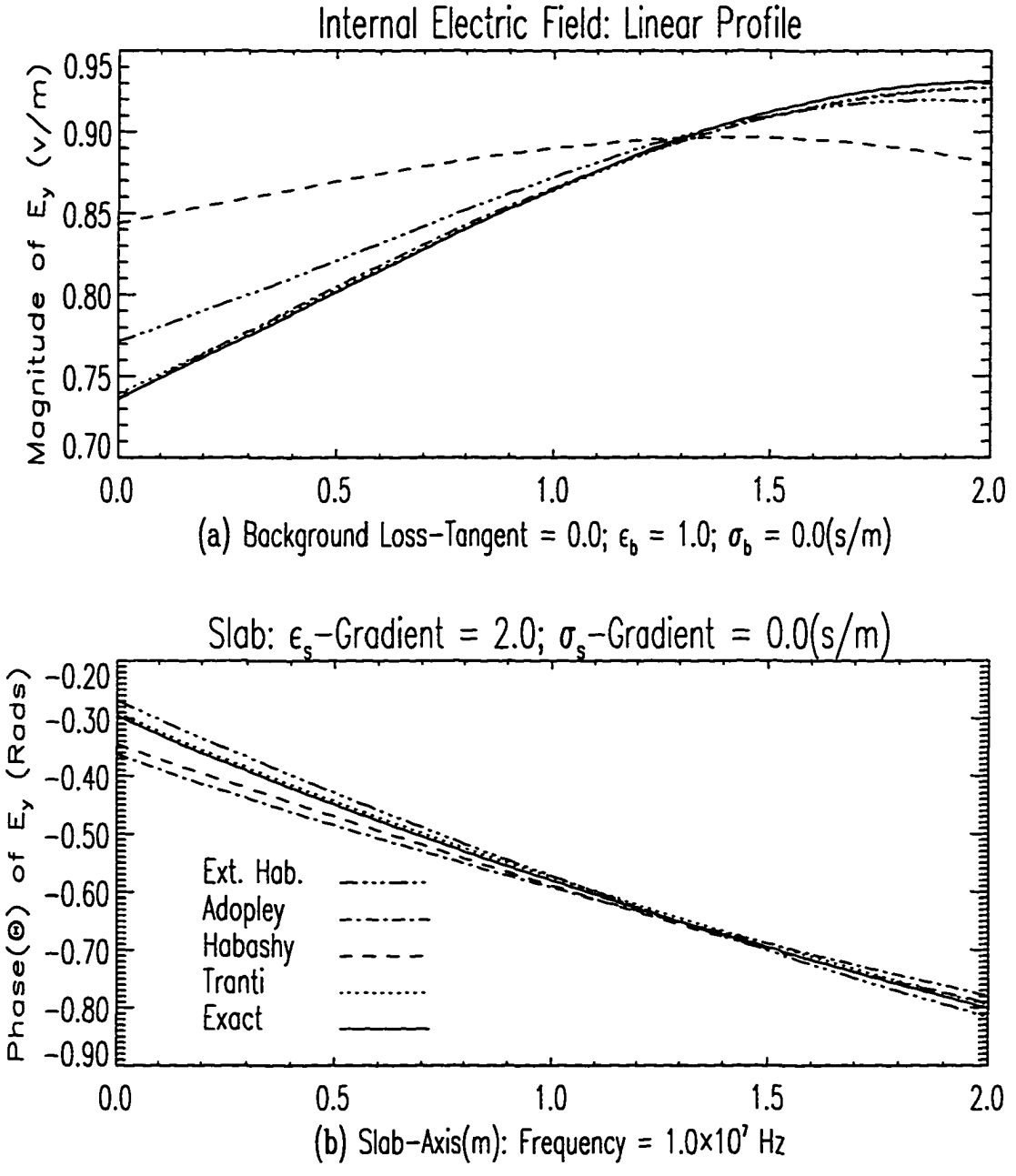

Figure 6.24: Effect of Large Dielectric Constant Gradient on Internal Electric Field

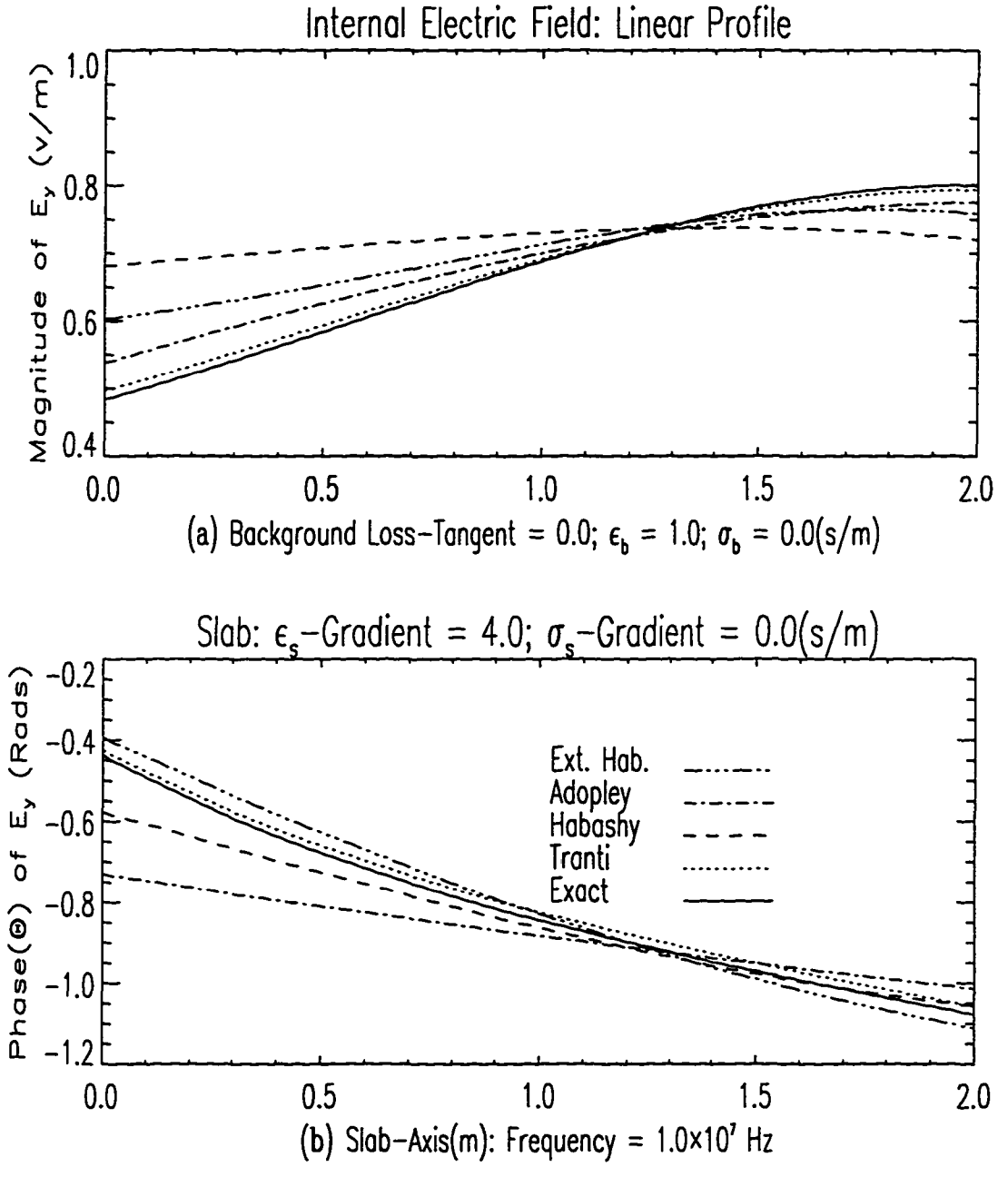

Figure 6.25: Effect of Doubling Dielectric Constant Gradient on Internal Electric Field

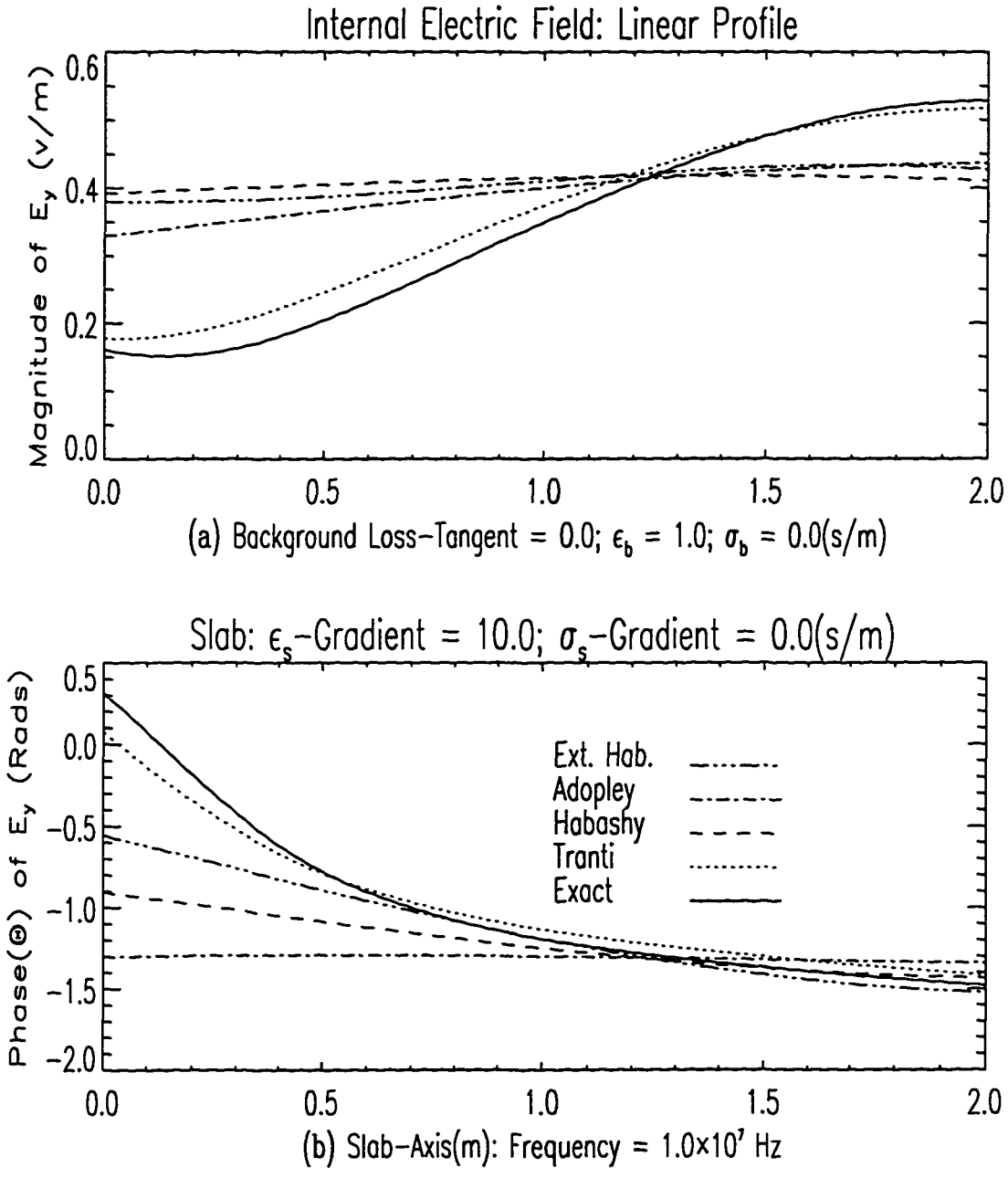

Figure 6.26: Effect of Very High Dielectric Constant Gradient on Internal Electric Field

the case of the magnitude plots. The phase plots show a relatively consistent degree of accuracy. From Figure 6.24 we observe a noticeable amount of degradation in accuracy for the phase plots of the Adopley model. However we also note a high degree of accuracy for the magnitude plot for the Adopley model. The higher phase error may be attributed to numerical computations since the phase is more sensitive to noise than the magnitude. When the $\epsilon -$ slope is further doubled to 4.0 we note appreciable degradation in accuracy for the magnitude plots in all models except the Trantanella model. The Adopley approximation shows the least accuracy in the phase plots. In Figure 6.26, we increase the $\epsilon -$ slope to 10.0. We note a general breakdown for all models except the Trantanella model which consistently predicts relatively very accurate results for both magnitude and phase plots.

6.3.2 External Scattered Electric Field

Our next group of plots deals with the complex slope for the lossy slab. We remark that we were unable to generate satisfactory results using the exact formulation for complex arguments of the *Airy* functions. Also we were unsuccessful in locating tabulated results of the *Airy* functions with complex argument that we could verify our computations against. We have therefore elected to perform a relative comparison between the various approximations for the lossy-slab cases. These results are shown in Figures 6.27-6.34. In these figures the Extended Habashy model always predicts higher values for both magnitude and phase than the Habashy model at

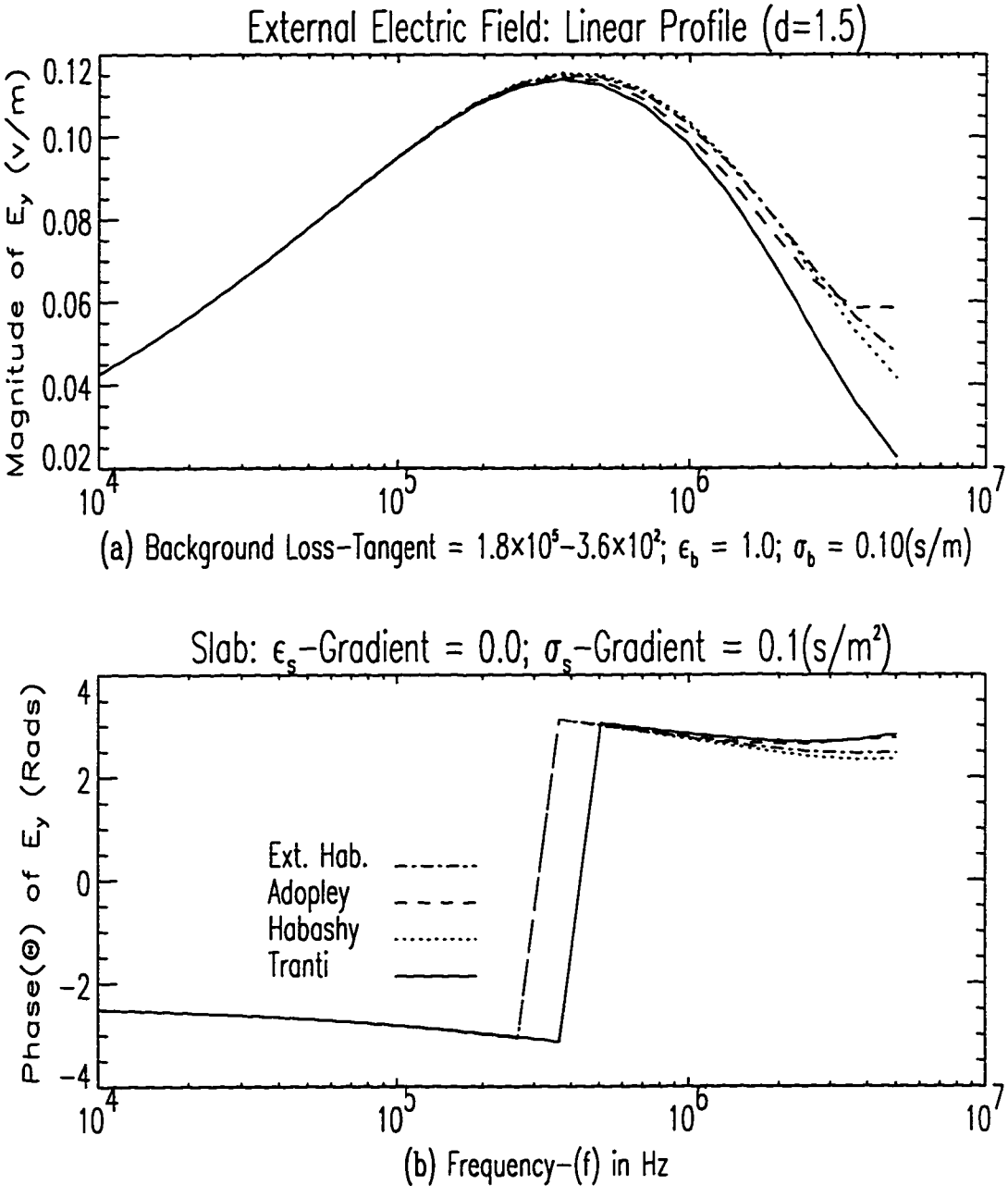

Figure 6.27: Relative Performance of Different Models for Conductivity Gradient (Electric Field at $z = 0$)

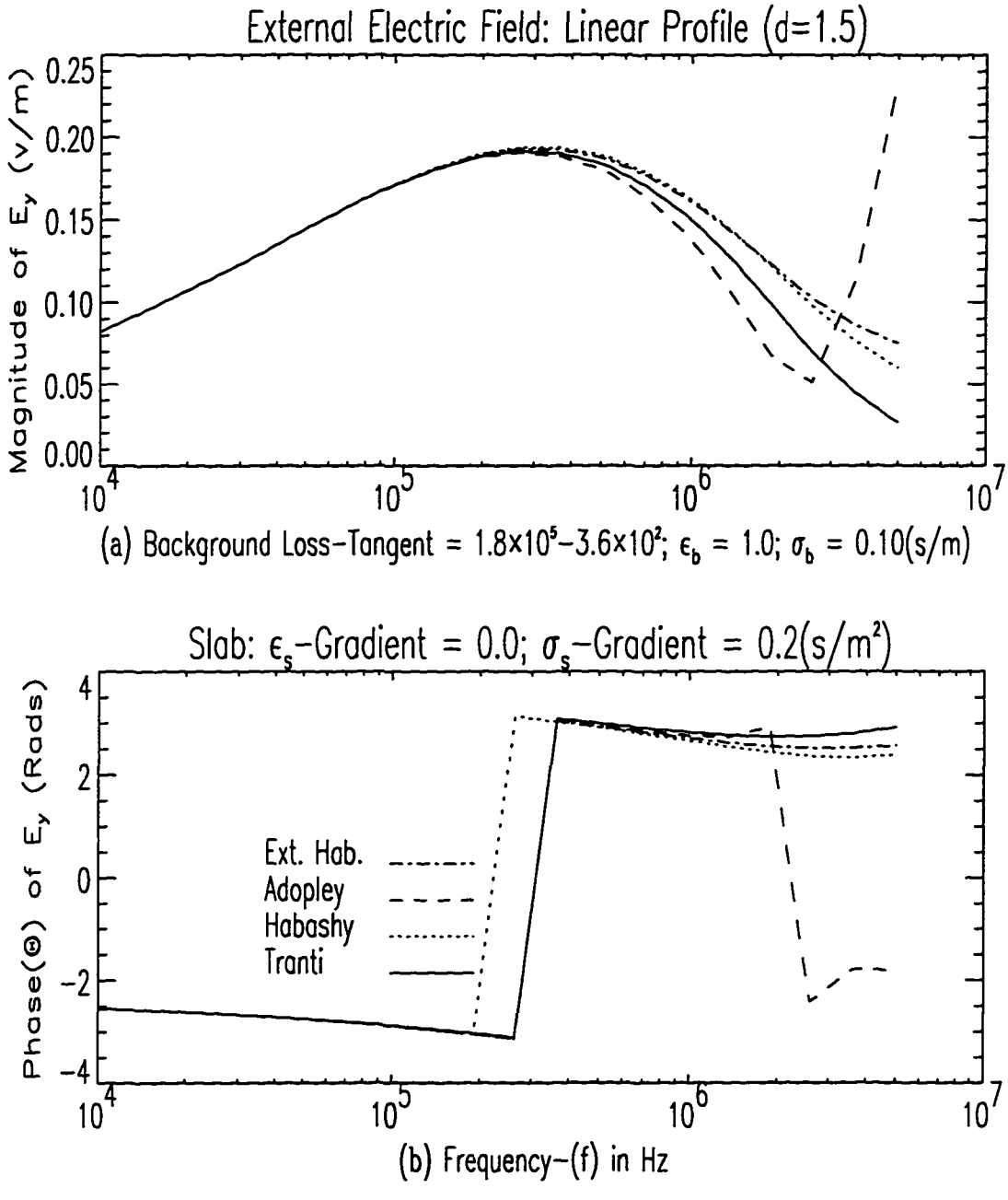

Figure 6.28: Relative Performance of Different Models for Increasing Conductivity Gradient (Electric Field, $z = 0$)

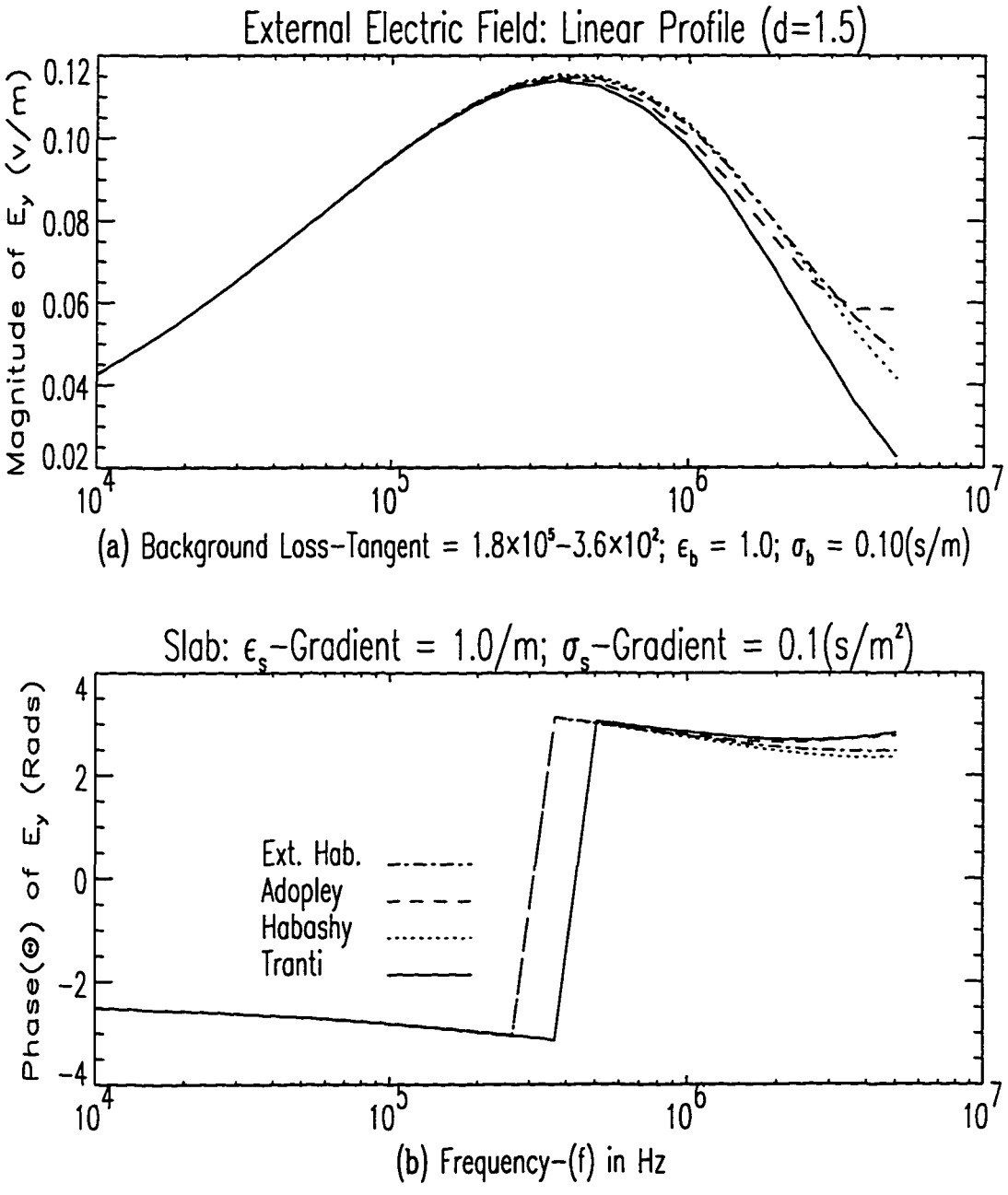

Figure 6.29: Effect of Dielectric Constant Gradient on Electric Field ($z = 0$)

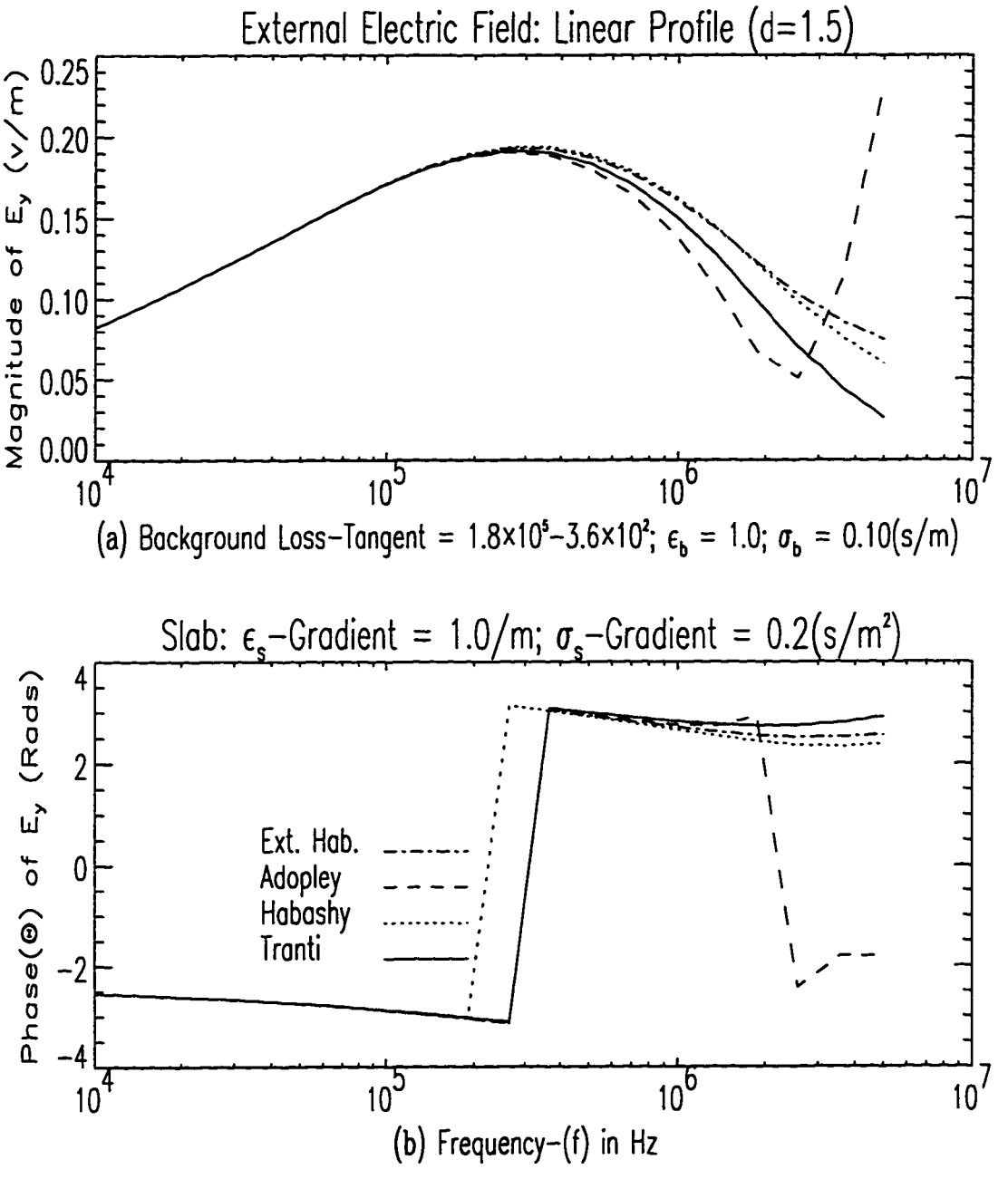

Figure 6.30: Effect of Dielectric Constant Gradient on Electric Field ($z = 0$)

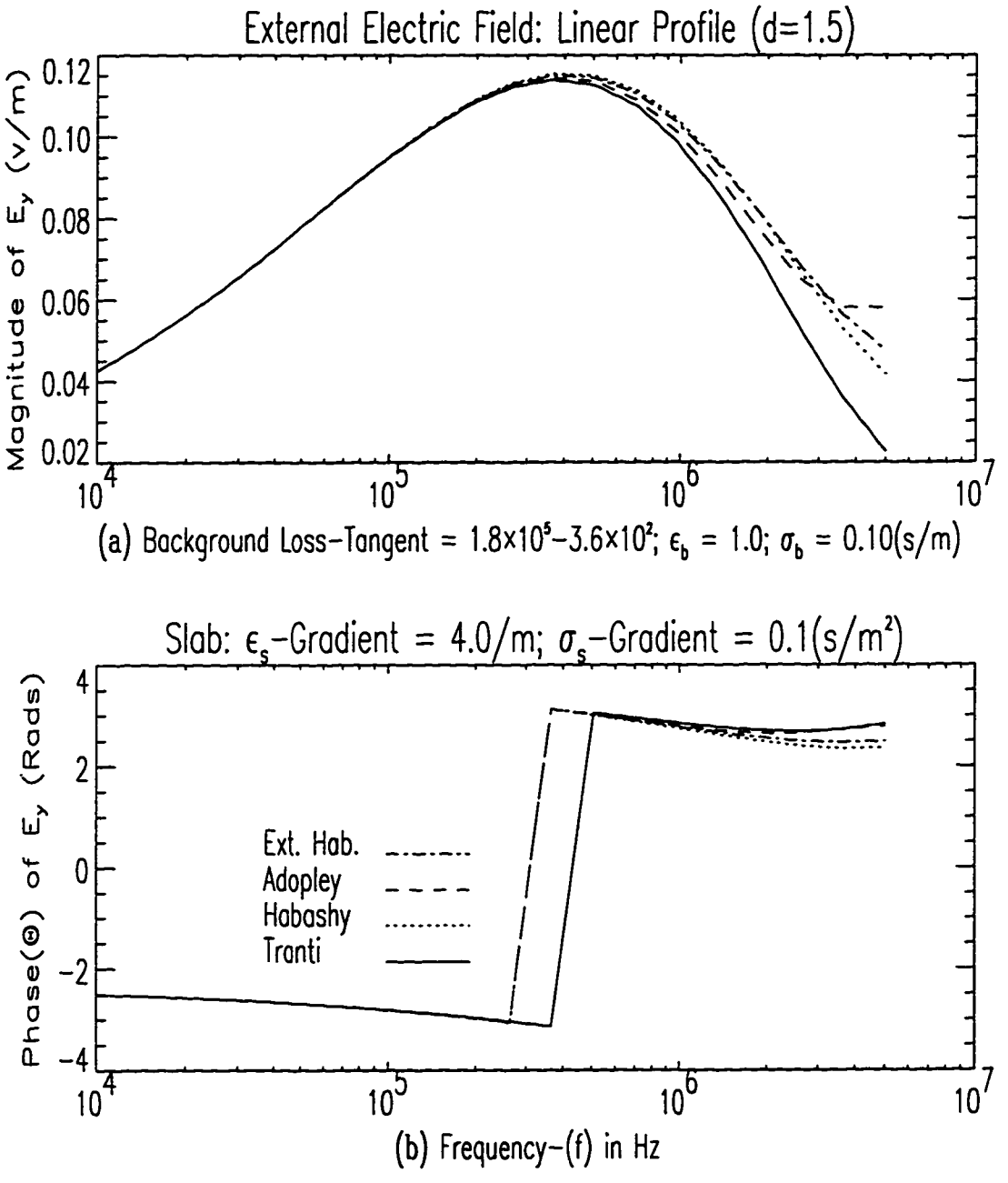

Figure 6.31: Effect of Increasing Dielectric Constant Gradient on Electric Field ($z = d$)

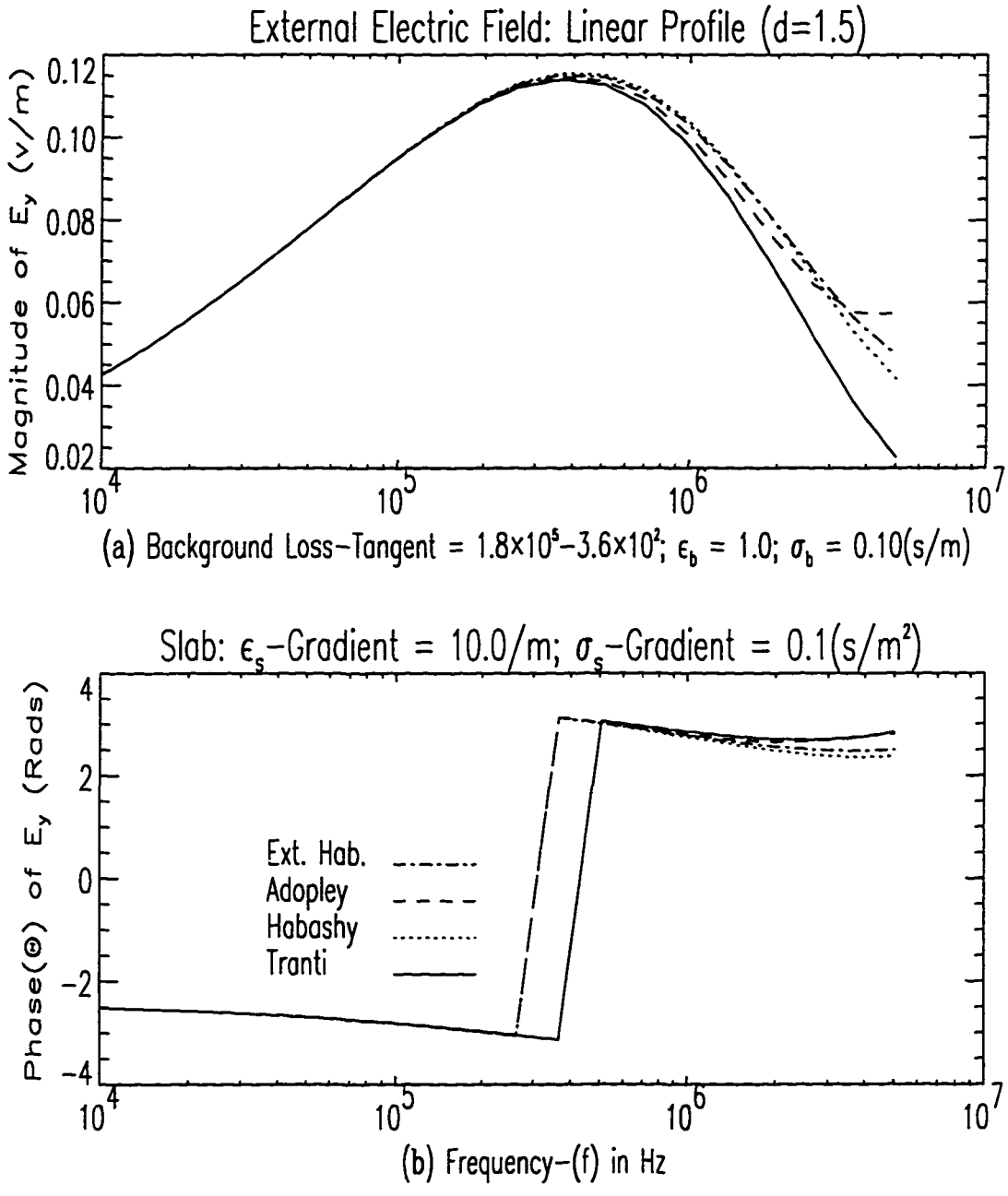

Figure 6.32: Effect of Large Dielectric Constant Gradient on Electric Field ($z = 0$)

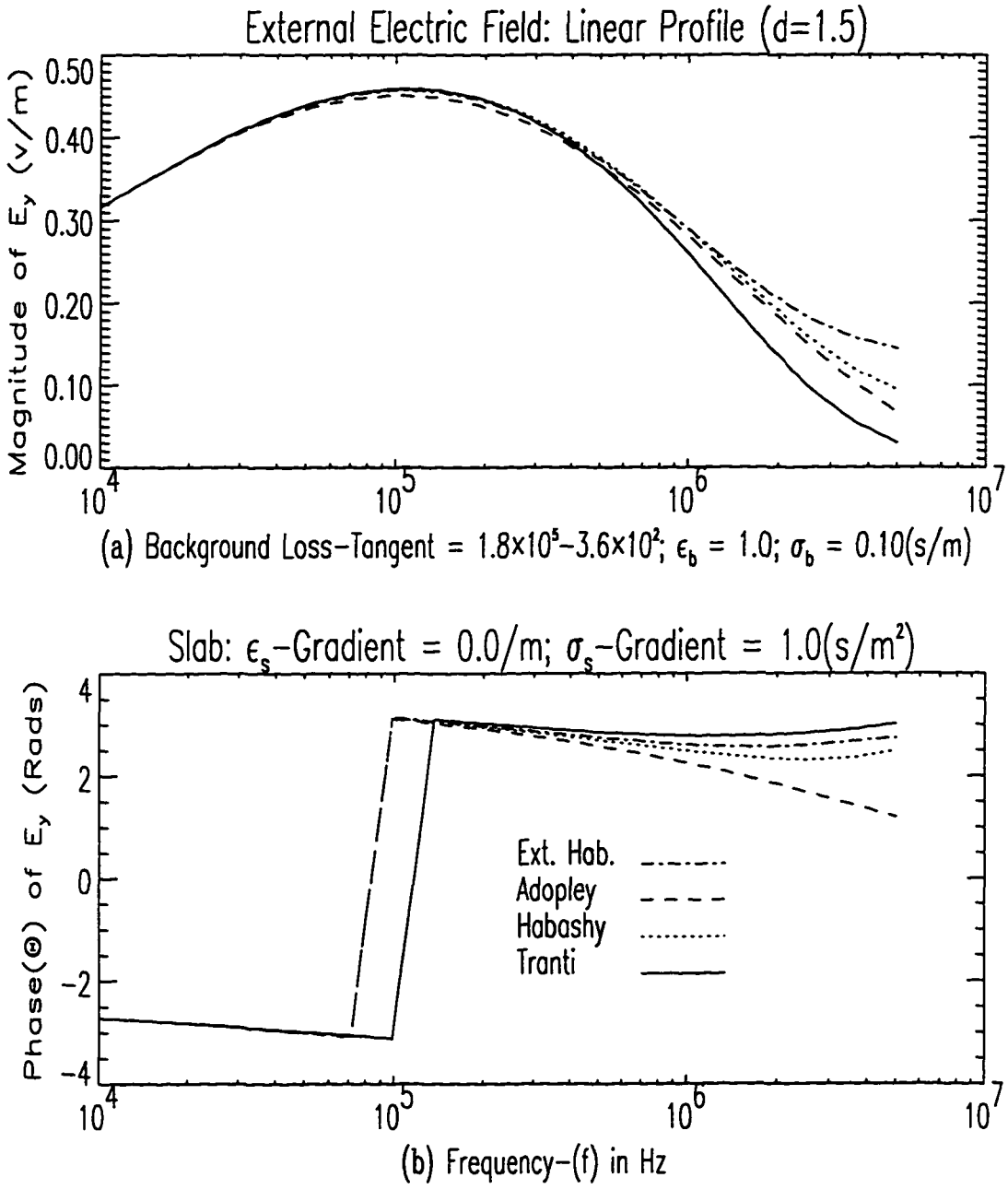

Figure 6.33: Effect of Increasing Conductivity Gradient on Electric Field ($z = 0$)

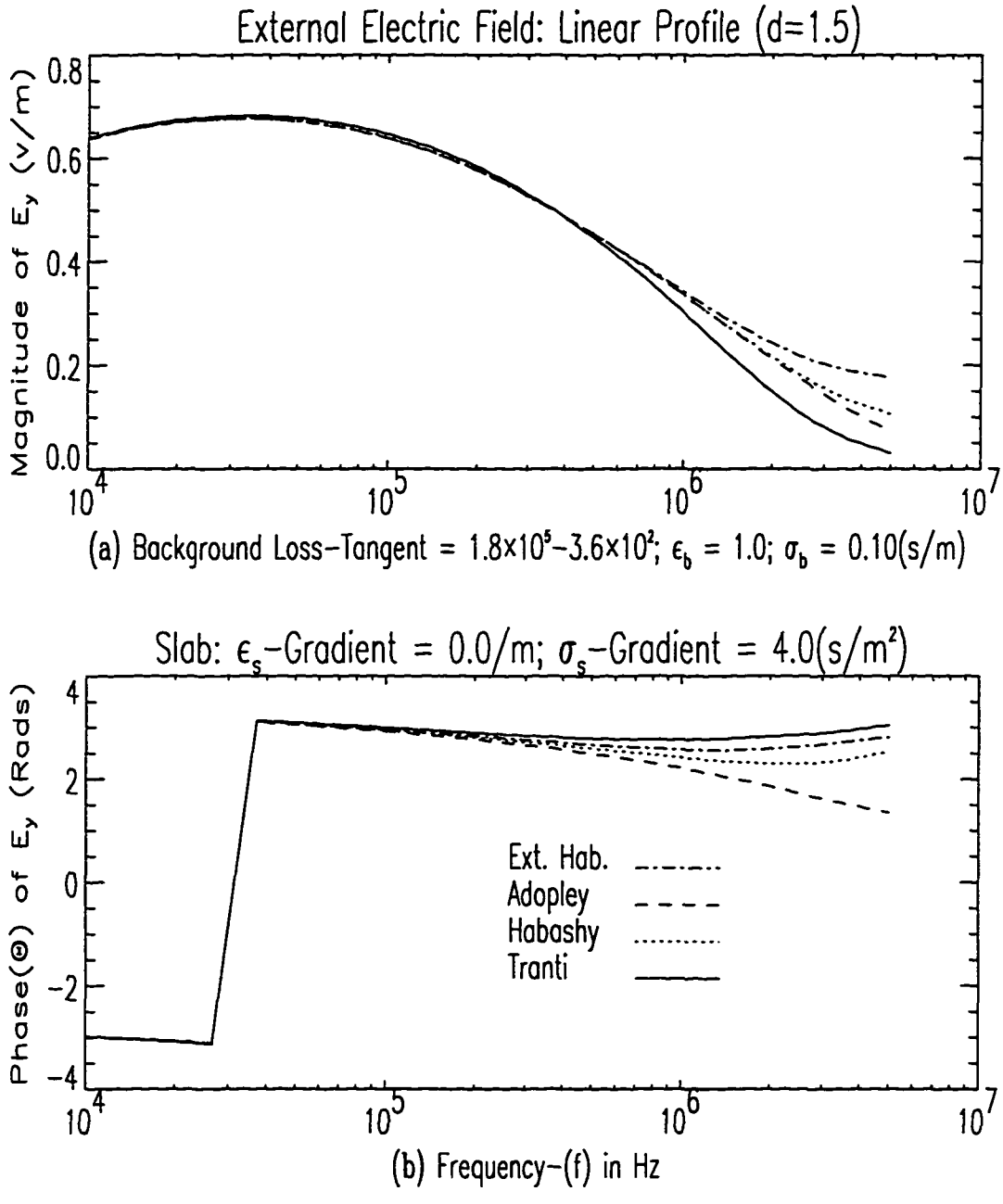

Figure 6.34: Effect of Large Conductivity Gradient on Electric Field ($z = 0$)

high frequencies. One other prominent feature from these plots is that the Habashy model consistently predicted higher magnitude and lower phase values than the Trantanella model at high frequencies. We also observed that as the conductivity slope is increased, the Habashy and the Adopley models predict the same values in the magnitude. At high frequencies the Adopley model predicts a lower phase than the Habashy model for conductivity slope above $0.4s/m^2$.

From our numerical simulations we observe that the internal field evaluation at the boundary was most accurate in almost all cases for the Trantanella approximation. We believe this to be a direct result of specifically enforcing field continuity between the internal and the external expressions at the boundary $z = 0$. It was also noted that the Habashy approximation improves in accuracy with an increase in conductivity contrast. This we explain by the localization of the Green's function for higher conductivities, thus fulfilling the conditions under which the approximation was valid.

CHAPTER 7

Inversion Algorithm

In this chapter we present a formulation of the inversion algorithm. It is based on the philosophy of obtaining the best model with minimum structure or "roughness". This particular inversion method, called Occam's method [36] is described below. It is a practical scheme which optimizes the step size at each and every iteration while maintaining the computational efficiency of layered models. The end result is a stable and rapidly convergent algorithm. We now present the specifics of the method.

7.1 Occam's Method

The traditional least-squares inversion for simple layered models derives its stability from the smoothness of the model function within the layers. Thus a two layered model requires perfectly piecewise smooth model function with a single discontinuity. With an increase in number of layers, this restriction is relaxed. However as the number of layers increases, the layer size at some point falls below the resolving power of the observed data. The model then tends to exhibit features not required by the observed data. Simple layered model fits then become a delicate game played between suppressing significant structures from including too few parameters to introducing

phantom structures from including too many parameters. One school of thought is that, one should permit the model to be as flexible as possible while explicitly suppressing complexity. In [36], this is achieved by defining a roughness parameter as the integrated square of the first or second derivative with respect to width (size) viz:

$$R_1 = \int \left(\frac{d\mathbf{m}}{dz}\right)^2 dz \qquad \text{or} \qquad R_2 = \int \left(\frac{d^2\mathbf{m}}{dz^2}\right)^2 dz \tag{7.1}$$

where $\mathbf{m}(z)$ is the model of, in our particular case, complex conductivity. In our inversion we employ a piecewise constant model defined by

$$\mathbf{m}(z) = \sum_{i=1}^{N} \mathbf{m}_i f_i(z) \tag{7.2}$$

where

$$f_i(z) = \begin{cases} 1; & z \in (z_{i-1}, z_i) \\ 0; & \text{otherwise} \end{cases} \tag{7.3}$$

A discrete version of the roughness parameter that utilizes difference rather than differential operators is

$$R_1 = \sum_{i=2}^{N} (\mathbf{m}_i - \mathbf{m}_{i-1})^2 \tag{7.4}$$

and

$$R_2 = \sum_{i=2}^{N} (\mathbf{m}_{i+1} - 2\mathbf{m}_i + \mathbf{m}_{i-1})^2 \tag{7.5}$$

We denote M measured data as $\mathbf{d}_j$ with $j = 1, 2, \cdots, M$. These are the observed scattered electric field at the slab boundary for our particular problem. We assume that each datum $\mathbf{d}_j$ is associated with an error estimate ν_j. We also assume that

the uncertainties associated with the measured data are due to zero-mean Gaussian processes which are independent in each of the observed datum. The ν_j then become the standard deviations. It is instructive to realize that this is a great deal to assume. But in the light of very poor and often negligible information about error statistics, it is vain to employ more refined statistics that are usually not worth the enormous additional labor involved. Even though the zero-mean independent Gaussian process is most pervasive in the literature, other forms of error statistics have been used [47]. We predict the measured data through a discrete model as $\mathbf{d}_j = F_j[\mathbf{m}]$ and define the acceptability of the model prediction to the actual values with a weighted *Least-square* error

$$\chi^2 = \sum_{j=1}^{M} \left(\frac{\mathbf{d}_j - F_j[\mathbf{m}]}{\nu_j} \right)^2 \tag{7.6}$$

where as defined earlier ν_j is the uncertainty in the j^{th} datum. Here we assume statistical independence in the error.

We may state the mathematical problem as follows: presented with a set of measured data $\mathbf{d_j}$ with the associated uncertainties ν_j, find a model $\mathbf{m}$ that minimizes R_1 or R_2 while χ^2 is kept below some predefined threshold value. This is a nonlinear optimization problem and there is no guarantee that some $\mathbf{m}_i$ will reduce χ^2 to a low enough value. However, we assume that, with some constraints on the model parameters consistent with the physics of the problem, we can obtain a good enough model that will provide a reasonable fit to the observed data. We now proceed to define our cost function to be minimized. We represent R_1 and R_2 in matrix operator

form as

$$R_1 = ||\underline{\delta}\mathbf{m}||^2 \tag{7.7}$$

$$R_2 = ||\underline{\delta}\ \underline{\delta}\mathbf{m}||^2 \tag{7.8}$$

where $\underline{\delta}$ is an $N \times N$ matrix defined by

$$\underline{\delta} = \begin{bmatrix} 0 & & & \\ -1 & 1 & & 0 \\ & -1 & 1 & \\ & & \cdots & \\ & 0 & & -1 \quad 1 \end{bmatrix} \tag{7.9}$$

Also $\mathcal{X}^2$ is given as

$$\mathcal{X}^2 = \|\underline{W}\mathbf{d} - \underline{W}F[\mathbf{m}]\|^2 \tag{7.10}$$

$\underline{W}$ is $M \times M$ diagonal matrix given by

$$\underline{W} = diag\{1/\nu_1, 1/\nu_2, \cdots 1/\nu_M\} \tag{7.11}$$

The uncertainties ν_j are assumed to be zero-mean independent Gaussian processes. Thus $\mathcal{X}^2$ has a χ^2 distribution with expected value of M.

From constraint theory, we apply the Lagrangian multiplier to define our cost function U as

$$U = ||\underline{\delta}\mathbf{m}||^2 + \mu^{-1}\left\{||\underline{W}\mathbf{d} - \underline{W}F[\mathbf{m}]||^2 - \chi_*^2\right\} \tag{7.12}$$

where the first term of U is the roughness and the second term is the misfit weighted by the Lagrangian multiplier. In nonlinear analysis we compute $F[\mathbf{m}]$ to the first

order due to a perturbation of the model $\mathbf{m}_1$

$$F[\mathbf{m}_0 + \Delta] = F[\mathbf{m}_0] + \underline{\mathrm{J}}_0\Delta + \varepsilon \tag{7.13}$$

where ε is a vector with magnitude of $o||\Delta||$ and $\underline{\mathrm{J}}_0$ is s the Jacobian defined by

$$\underline{\mathrm{J}}_0 = \nabla_{\mathbf{m}} F[\mathbf{m}] \tag{7.14}$$

and $\Delta = \mathbf{m}_1 - \mathbf{m}_0$. The implicit assumption is that $F[\mathbf{m}_0]$ is diferentiable about the base model $\mathbf{m}_0$. Approximating $F[\mathbf{m}_1]$ as $F[\mathbf{m}_0] + \underline{\mathrm{J}}_0\Delta$ and substituting into U, we have

$$U = ||\underline{\delta}\mathbf{m}_1||^2 + \mu^{-1}\left\{||\underline{W}(\mathbf{d} - F[\mathbf{m}_0] + \underline{\mathrm{J}}_0\mathbf{m}_0) - \underline{W}\underline{\mathrm{J}}_0\mathbf{m}_1||^2 - \chi_*^2\right\} \tag{7.15}$$

Under this approximation, we define $\mathbf{m}_1$ as the model that minimizes U. Then we employ linear theory to obtain for $dU/d\mathbf{m}_1 = 0$

$$\left[\mu\underline{\delta}^T\underline{\delta} + \underline{W}\underline{\mathrm{J}}_0)^T(\underline{W}\underline{\mathrm{J}}_0)\right]\mathbf{m}_1 = (\underline{W}\underline{\mathrm{J}}_0)^T(\underline{W}\hat{\mathbf{d}})$$

where $\hat{\mathbf{d}} = \underline{W}(\mathbf{d} - F[\mathbf{m}_0] + \underline{\mathrm{J}}_0\mathbf{m}_0)$. We then generate an iterative scheme by selecting μ to yield the desired misfit from computation. $\mathbf{m}_1$ is then used to compute $\mathbf{m}_2$ until the scheme converges, if at all. It may be shown that if the system converges, it solves the original minimization problems with the final solution independent of the starting values, provided the minimum is unique.

The iterative method adopted in [36] did not follow the usual straightforward minimization. Instead, the authors employed a modified iterative scheme that proved

to be very effective in our case. It is as follows: Suppose we have the k^{th} iterate; then we define the vector

$$\mathbf{m}_{k+1}(\mu) = \left[\mu\underline{\delta}^T\underline{\delta} + \underline{W}\mathbf{J}_k)^T(\underline{W}\mathbf{J}_k)\right]^{-1}(\underline{W}\mathbf{J}_k)^T(\underline{W}\hat{d}_k)$$

Next a 1-D line search is employed to find μ that minimizes the true misfit given by

$$\mathcal{X}_{k+1}(\mu) = ||\underline{W}\mathbf{d} - \underline{W}F[\mathbf{m}_{k+1}(\mu)]||$$

This is because any initial guess is usually far from the true model and whatever value of μ is selected, $\mathcal{X}_k$ is always greater than χ_*. After a number of minimizations μ is selected for $\mathcal{X}_k$ to match χ_* exactly. In our version of Occam's inversion, we did not implement the last procedure. Instead, we define a set of convergence criteria which terminates the process whenever a criterion within the set is satisfied. We adopted this modification after we found from extensive numerical experimentation that it is not always possible to find a model vector $\mathbf{m}$ that will match a particular χ_* exactly. The inversion has been applied to three versions of the localized approximations developed in the previous chapters. These are the Adopley model, the Habashy model and the Extended Habashy model.

Before presenting any results we give a derivation of the Jacobian matrix for the Adopley, Habashy and the Extended Habashy models. In our derivation our model parameters are σ and ϵ which were denoted by m in the above derivations. All derivations are carried out for the σ formulation. The ϵ system of equations is not different from the σ one. Indeed the ϵ derivation can be obtained by inspection from the σ results.

7.2 Adopley Model

From the σ formulation presented earlier we have

$$\begin{aligned} E_y^s(z) &\approx \frac{k_b}{2j\bar{\sigma}_b} e^{jk_b z} \sum_{n=1}^{N} \bar{\sigma}_n \int_{\Delta n} e^{-jk_b z'} \bar{E}_n(z') \Gamma_n(z') dz' \quad \text{for } z < 0 \\ E_y^s(z) &\approx \frac{k_b}{2j\bar{\sigma}_b} e^{-jk_b z} \sum_{n=1}^{N} \bar{\sigma}_n \int_{\Delta n} e^{jk_b z'} \bar{E}_n(z') \Gamma_n(z') dz' \quad \text{for } z > d \end{aligned} \tag{7.16}$$

where $\bar{E}_p(z)$ and $\Gamma_p(z)$ are given by equations (4.17) and (4.23) respectively. We will restrict the Jacobian derivation for $z < 0$ only; the Jacobian for $z > d$ could be written down by inspection. (Note: d in this section represents the slab size and not data point as in the optimization formulation.) For convenience we denote $E_y^s(z < 0, \omega)$ as $E0(\omega)$ where ω is the frequency of measurement. $E0(\omega_l)$ becomes

$$E0(\omega_l) = \frac{k_b}{2j\bar{\sigma}_b} e^{jk_b z} \sum_{n=1}^{N} \bar{\sigma}_n \int_{\Delta n} e^{-jk_b z'} \bar{E}_n(z') \Gamma_n(z') dz' \tag{7.17}$$

where k_b is computed at ω_l. The Jacobian J_{lp} is defined as

$$J_{lp} = \frac{\delta(E0(\omega_l))}{\delta \sigma_p}$$

We then have for the Adopley model ($z < 0$),

$$\begin{aligned} J_{lp} &= -j \left(\frac{k_b}{2\bar{\sigma}_b} \right) e^{-jk_b z} \left\{ \int_{\Delta_p} e^{-jk_b z'} \bar{E}_p(z') \Gamma_p(z') dz' \right. \\ &+ \left. \sum_{n=1}^{N} \sigma_n \int_{\Delta_n} e^{-jk_b z'} \left(\bar{E}_n(z') \frac{d}{d\sigma_p} \Gamma_n(z') + \Gamma_n(z') \frac{d}{d\sigma_p} \bar{E}_n(z') \right) dz' \right\} \end{aligned}$$

where

$$\frac{d}{d\sigma_n} \bar{E}_p(z) = \frac{1}{4\bar{\sigma}_b} \begin{cases} -2k_b \Delta_n e^{-jk_b z} & n < p \\ e^{jk_b z} \left(e^{-jk_b z_n} - e^{-jk_b z_{n-1}} \right) & n > p \\ (j - 2k_b (z - z_{p-1})) e^{-jk_b z} + e^{-2jk_b z_p} e^{jk_b z} & n = p \end{cases}$$

$$\frac{d}{d\sigma_n}(\Gamma_p(z))^{-1} = -\frac{1}{8\bar{\sigma}_b{}^2}\left\{\left(F_{n1}(\bar{\sigma}) + \sum_{m=1}^{p-1}\bar{\sigma}_m\frac{d}{d\sigma_n}F_{m1}(\bar{\sigma}) + \bar{\sigma}_p\frac{d}{d\sigma_n}F_{p1}(\bar{\sigma}\right)e^{-jk_bz}\right.$$
$$\left. - \left(\sum_{m=p+1}^{N}\bar{\sigma}_m\frac{d}{d\sigma_n}F_{m2}(\bar{\sigma}) + \bar{\sigma}_p\frac{d}{d\sigma_n}F_{p2}(\bar{\sigma})\right)e^{jk_bz}\right\} \quad n < p$$

$$\frac{d}{d\sigma_n}(\Gamma_p(z))^{-1} = -\frac{1}{8\bar{\sigma}_b{}^2}\left\{\left(\sum_{m=1}^{p-1}\bar{\sigma}_m\frac{d}{d\sigma_n}F_{m1}(\bar{\sigma}) + \bar{\sigma}_p\frac{d}{d\sigma_n}F_{p1}(\bar{\sigma}\right)e^{-jk_bz}\right.$$
$$\left. - \left(F_{n2}(\bar{\sigma}) + \sum_{m=p+1}^{N}\bar{\sigma}_m\frac{d}{d\sigma_n}F_{m2}(\bar{\sigma}) + \bar{\sigma}_p\frac{d}{d\sigma_n}F_{p2}(\bar{\sigma}\right)e^{jk_bz}\right\} \quad n > p$$

$$\frac{d}{d\sigma_n}(\Gamma_p(z))^{-1} = -\frac{2\bar{\sigma}_p}{\bar{\sigma}_b{}^2}$$
$$- \frac{1}{8\bar{\sigma}_b{}^2}\left\{\left(\sum_{m=1}^{p-1}\bar{\sigma}_m\frac{d}{d\sigma_n}F_{m1}(\bar{\sigma}) + F_{p1}(\bar{\sigma} + \bar{\sigma}_p\frac{d}{d\sigma_n}F_{p1}(\bar{\sigma}\right)e^{-jk_bz}\right.$$
$$\left. - \left(\sum_{m=p+1}^{N}\bar{\sigma}_m\frac{d}{d\sigma_n}F_{m2}(\bar{\sigma}) + F_{p2}(\bar{\sigma} + \bar{\sigma}_p\frac{d}{d\sigma_n}F_{p2}(\bar{\sigma})\right)e^{jk_bz}\right\} \quad n = p$$

$$\frac{d}{d\sigma_n}F_{m1}(\bar{\sigma}) = \begin{cases} 2jk_b\Delta_m\frac{d}{d\sigma_n}Q_{Lm} & n < m \\ -\left(e^{2jk_bz_m} - \left(e^{2jk_bz_{m-1}}\right)\frac{d}{d\sigma_n}Q_{Um}\right. & n > m \\ \left\{2jk_b\Delta_n\frac{d}{d\sigma_n}Q_{Ln} + 4\left(e^{jk_bz_n} - e^{jk_bz_{n-1}}\right)\right. & \\ \left. -\left(e^{2jk_bz_n} - \left(e^{2jk_bz_{n-1}}\right)\frac{d}{d\sigma_n}Q_{Un}\right\}\right. & n = m \end{cases}$$

$$\frac{d}{d\sigma_n}F_{m2}(\bar{\sigma}) = \begin{cases} \left(e^{-2jk_bz_m} - \left(e^{-2jk_bz_{m-1}}\right)\frac{d}{d\sigma_n}Q_{Lm}\right. & n < m \\ 2jk_b\Delta_m\frac{d}{d\sigma_n}Q_{Um} & n > m \\ \left\{2jk_b\Delta_n\frac{d}{d\sigma_n}Q_{Un} + 4\left(e^{-jk_bz_n} - e^{-jk_bz_{n-1}}\right)\right. & \\ \left. +\left(e^{-2jk_bz_n} - e^{-2jk_bz_{n-1}}\right)\frac{d}{d\sigma_n}Q_{Ln}\right\}\right. & n = m \end{cases}$$

$$\frac{d}{d\sigma_n}F_{p1}(\bar{\sigma}) = \begin{cases} (1+2jk_b\Delta_{p-1})\frac{d}{d\sigma_n}Q_{Lp} & n<p \\ e^{2jk_bz_{p-1}}\frac{d}{d\sigma_n}Q_{Up} & n>p \\ \left\{e^{2jk_bz_{p-1}}\frac{d}{d\sigma_p}Q_{Up} - 4e^{jk_bz_{p-1}}\right. & \\ \left.+(1+2jk_b\Delta_{p-1})\frac{d}{d\sigma_p}Q_{Lp}\right\} & n=p \end{cases}$$

$$\frac{d}{d\sigma_n}F_{p2}(\bar{\sigma}) = \begin{cases} e^{-2jk_bz_p}\frac{d}{d\sigma_n}Q_{Lp} & n<p \\ (1+2jk_b\Delta_p)\frac{d}{d\sigma_n}Q_{Up} & n>p \\ \left\{e^{-2jk_bz_p}\frac{d}{d\sigma_p}Q_{Lp} + 4e^{-jk_bz_p}\right. & \\ \left.+(1+2jk_b\Delta_p)\frac{d}{d\sigma_p}Q_{Up}\right\} & n=p \end{cases}$$

$$\frac{d}{d\sigma_n}Q_{Lm}(\bar{\sigma}) = \begin{cases} e^{jk_bz_n} - e^{jk_bz_{n-1}} & n<m \\ 0 & n>m \\ e^{jk_bz_{n-1}} & n=m \end{cases}$$

$$\frac{d}{d\sigma_n}Q_{Um}(\bar{\sigma}) = \begin{cases} 0 & n<m \\ e^{-jk_bz_n} - e^{-jk_bz_{n-1}} & n>m \\ e^{-jk_bz_n} & n=m \end{cases}$$

7.3 Habashy Model

For the Habashy model the scattered electric field ($z<0$) is given by

$$E_y^s(z) \approx \frac{k_b}{2j\bar{\sigma}_b}e^{jk_bz}\sum_{n=1}^{N}\bar{\sigma}_n\int_{\Delta n}e^{-2jk_bz'}\Gamma_n(z')dz' \qquad (7.18)$$

The Jacobian J_{lp} is therefore given by

$$\begin{aligned} J_{lp} &= \frac{k_b}{2j\bar{\sigma}_b} e^{jk_b z} \left\{ \int_{\Delta p} e^{-2jk_b z'} \Gamma_p(z') dz' \right. \\ &+ \left. \sum_{n=1}^{N} \bar{\sigma}_n \int_{\Delta n} e^{-2jk_b z'} \frac{d}{d\sigma_p} \Gamma_n(z') dz' \right\} \end{aligned} \tag{7.19}$$

where

$$\frac{d}{d\sigma_p}\Gamma_n(z) = -[\Gamma_n(z)]^2 \frac{d}{d\sigma_p}(\Gamma_n(z))^{-1} \tag{7.20}$$

and

$$\frac{d}{d\sigma_p}(\Gamma_n(z))^{-1} = \frac{1}{2\bar{\sigma}_b} \begin{cases} e^{-jk_b z}\left(e^{jk_b z_p} - e^{jk_b z_{p-1}}\right) & p < n \\ -e^{jk_b z}\left(e^{-jk_b z_p} - e^{-jk_b z_{p-1}}\right) & p > n \\ 2 - e^{-jk_b z} e^{jk_b z_{p-1}} - e^{jk_b z} e^{-jk_b z_p} & p = n \end{cases}$$

7.4 Extended Habashy Model

In case of the Extended Habashy model, the Jacobian J_{lp} for $z < 0$ is given by

$$\begin{aligned} J_{lp} &= -j\left(\frac{k_b}{2\bar{\sigma}_b}\right) e^{-jk_b z} \left\{ \int_{\Delta_p} e^{-jk_b z'} \bar{E}_p(z') dz' \right. \\ &+ \left. \sum_{n=1}^{N} \sigma_n \int_{\Delta_n} e^{-jk_b z'} \frac{d}{d\sigma_p} \bar{E}_n(z') dz' \right\} \end{aligned}$$

where using equation (4.27) we obtain

$$\begin{aligned} \frac{d}{d\sigma_p}\bar{E}_n(z) &= 2E_y^{in}(z)(1-\Gamma_n(z))\frac{d}{d\sigma_p}\Gamma_n(z) \\ &- j\frac{k_b}{2\bar{\sigma}_b}\left\{ \frac{d}{d\sigma_p}\Gamma_n(z) \sum_{m=1}^{N} \bar{\sigma_m} \int_{\Delta_m} e^{-jk_b|z-z'|}\Gamma_n(z') dz' \right. \end{aligned}$$

$$+ \quad \Gamma_n(z) \int_{\Delta_p} e^{-jk_b|z-z'|} \Gamma_p(z') dz'$$

$$+ \quad \Gamma_n(z) \sum_{m=1}^{N} \bar{\sigma_m} \int_{\Delta_m} e^{-jk_b|z-z'|} \frac{d}{d\sigma_p} \Gamma_n(z') dz' \Big\} \tag{7.21}$$

We note that

$$\frac{d}{d\sigma_p} \Gamma_n(z) \tag{7.22}$$

is the same for the Habashy approximation.

This completes the inversion formulations. In the next chapter, we will present some results of extensive numerical experiments. We wish to state here that the formulation adopted here is simple and straightforward. There are other inversion techniques that others have used. Kleinman [40] was able to reconstruct sharp discontinuities using the total variational method of [38, 39]. The Occam's method that we have applied here is a "smoothest" method. Hence we cannot reconstruct sharp discontinuities. However the Occam's method will always indicate any change in the conductivity profile. It is a known fact that bandlimited electromagnetic radiation cannot detect step changes in conductivity profiles. Thus our method is consistent with the physical limitations of the experimental system. One difficulty in simultaneous reconstruction of dielectric constant and conductivity is that the complex conductivity is frequency dependent. This presents numerical computational problems, particularly very difficult to handle even with the subspace technique proposed in [30, 27].

CHAPTER 8

Numerical Inversion

We next present some results from extensive numerical inversions performed using the formulation developed in the Chapter 7. The inversions are performed on various types of piecewise constant conductivity profiles, which are shown in Figure 6.1, and the linear profile. Our most investigated profile is the "inclusion" type. This is because we consider this particular profile as a realistic approximation to some practical situations. Quite often in geophysical prospecting where inversion techniques are greatly utilized, the exact boundary of any discontinuity in conductivity profile is unknown. Also in non-destructive testing, the exact location of the anomaly is not known a priori. Hence the "inclusion" profile gives the most practical situation. We also investigate the effects of frequency and amplification factor in uneven slab partitioning on resolution of the reconstructed conductivity profile. These investigations are limited to the "inclusion" profile only. We will also present results for linear conductivity profiles.

In all our inversion experiments, we employ scattered electric field at the measurement boundary $z = 0$, which is equivalent to the reflection coefficient. For the piecewise constant profile we generated the synthetic measured data using the

transmission-line formulation. The data is then contaminated with Gaussian white-noise of zero mean and 5% standard deviation. This is used for all our inversions. We now present some of the inversion results.

8.1 Piecewise constant profile

The first conductivity reconstruction was performed on the constant profile. The homogeneous background conductivity (σ_b) and dielectric constant (ϵ_b) are $1.0 s/m$ and 1.0 respectively. These are the typical values used for most of the reconstructions presented. Data is sampled at frequencies distributed logarithmically between a minimum frequency of $10.0 Hz$ and a maximum frequency f_m which is selected individually for each inversion. We select the maximum frequency based on the maximum frequency at which the models accurately simulate the noiseless data. The reconstruction for the "uniform" piecewise constant profile is shown in Figure 8.1. The maximum frequency f_m utilized in this reconstruction is $10.0 KHz$. A slab-width of $4.0m$ is used in all the reconstructions. We observe from the figure that the Adopley model produced the best reconstruction with the Habashy model providing the least accurate. We also note from the figure that the error in reconstruction increases progressively from the leading edge of the slab, in case of the Adopley model. This is not the case for the other models. In fact, the error from the Extended-Habashy model peaks up approximately at midpoint within the slab and decreases towards

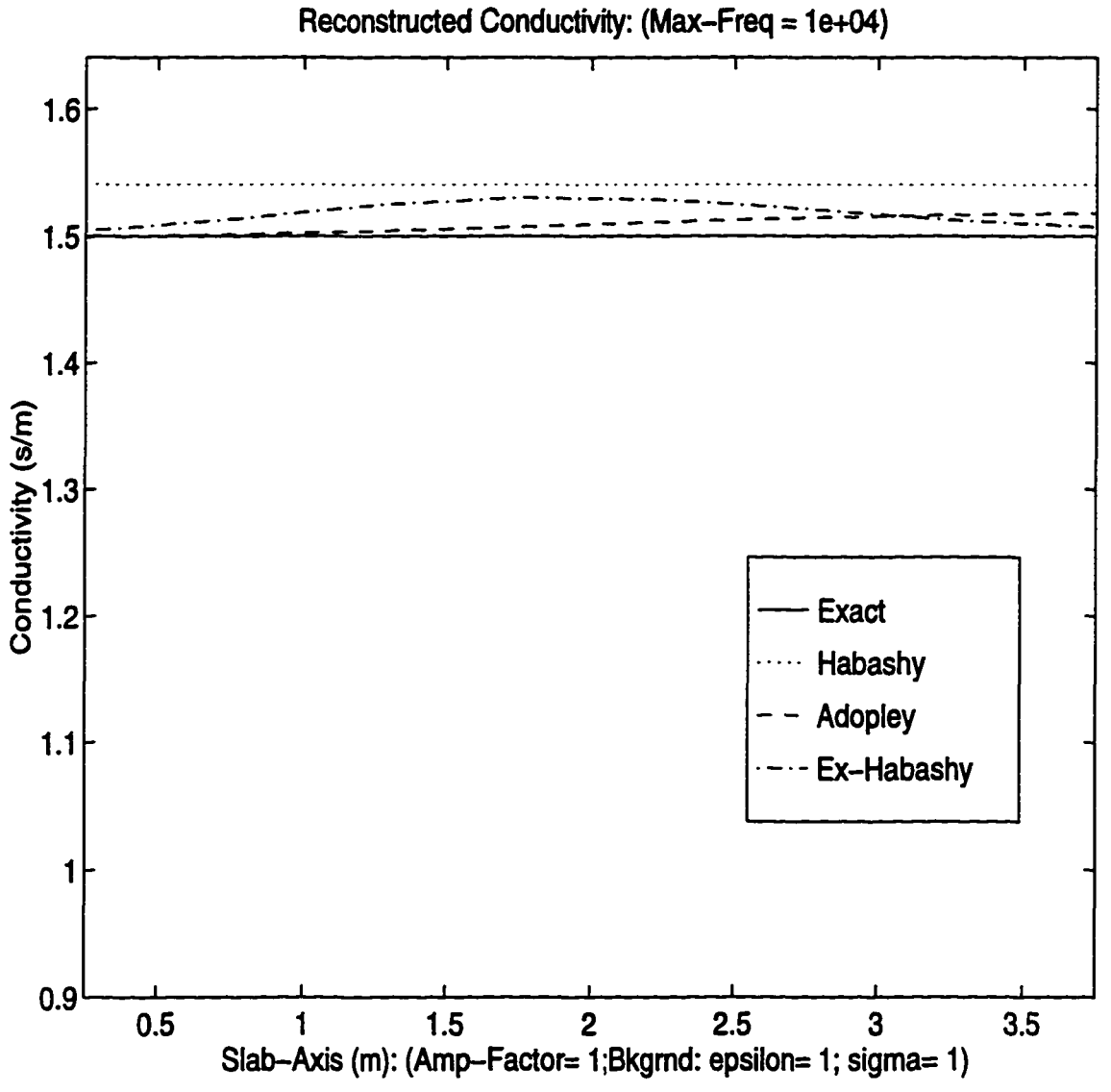

Figure 8.1: Constant Profile Reconstruction

the edges. The Habashy model on the other hand showed nearly uniform error distribution over the slab width. In the constant profile inversion, we observe greater error in profile reconstruction with higher frequencies. Figure 8.2 shows reconstruction of a left-step conductivity profile. The maximum frequency used in this inversion is $0.10MHz$. We note that the Adopley model provides the best inversion results followed by the Extended-Habashy model. The Adopley model also gave the best indication of the jump location in the conductivity profile. In this particular reconstruction, we have observed the Adopley model to be sensitive to initial guesses in the inversion. It was noted that if the initial guess of the profile is not of the same order of magnitude as the background conductivity profile, the inversion does not always converge. This we attribute to the formulation of the model. As was noted earlier in Chapter 2, the first iterative process in the formulation of the Adopley model is the Born approximation. This puts a limit on the magnitude of the contrast between the homogeneous background and slab profiles. Hence we have to be very aware of this limitation which is inherent in the formulation. Our observation is that, when the initial guess is more than two orders of magnitude or less than two orders of magnitude from the background profile, we most often experienced convergence problems. Indeed, the minimization gets trapped in a local minimum. This is easily detectable as the χ^2 values are very high and oscillate erratically between iterations. This is not the case for the Habashy and the Extended-Habashy models. These are very insensitive to initial guesses. It is noted for these two models that if the model

converges for a particular set of starting values, then it will converge for any set of starting values.

The next reconstruction is that of a right-step profile shown in Figure 8.3. We observe that the Habashy model produces the best reconstruction of the σ discontinuity location, followed by the Extended-Habashy model. However, the Habashy model predicted a higher step value. The best general profile reconstruction is by the Adopley model. One should observe that the discontinuity in conductivity of right-step profile is greater than the one used for the left-step profile shown in Figure 8.2. In general we observed that for larger discontinuities in conductivity profile, the Habashy model gives best prediction of its location. Also we note the overshoot above the discontinuity is closely correlated to its magnitude.

Most of our numerical investigation of the inversion algorithm is performed on the inclusion profile which we regard as the most realistic of any practical system. Hence almost all of our in-depth investigations involve the inclusion profile. The first two reconstructions of the inclusion profile are shown in Figures 8.4 and 8.5 which portray the relative performances of the different approximation models. In Figure 8.4 the maximum frequency of reconstruction is $0.10MHz$ and $1.0MHz$ for Figure 8.5. At the lower frequency, the Extended-Habashy model predicted the best results. We observe also that the Habashy model produced a little better results than the Adopley model. However, for reconstruction at the higher frequency shown in Figure 8.5, the Adopley model seemed to have produced the overall best results. One

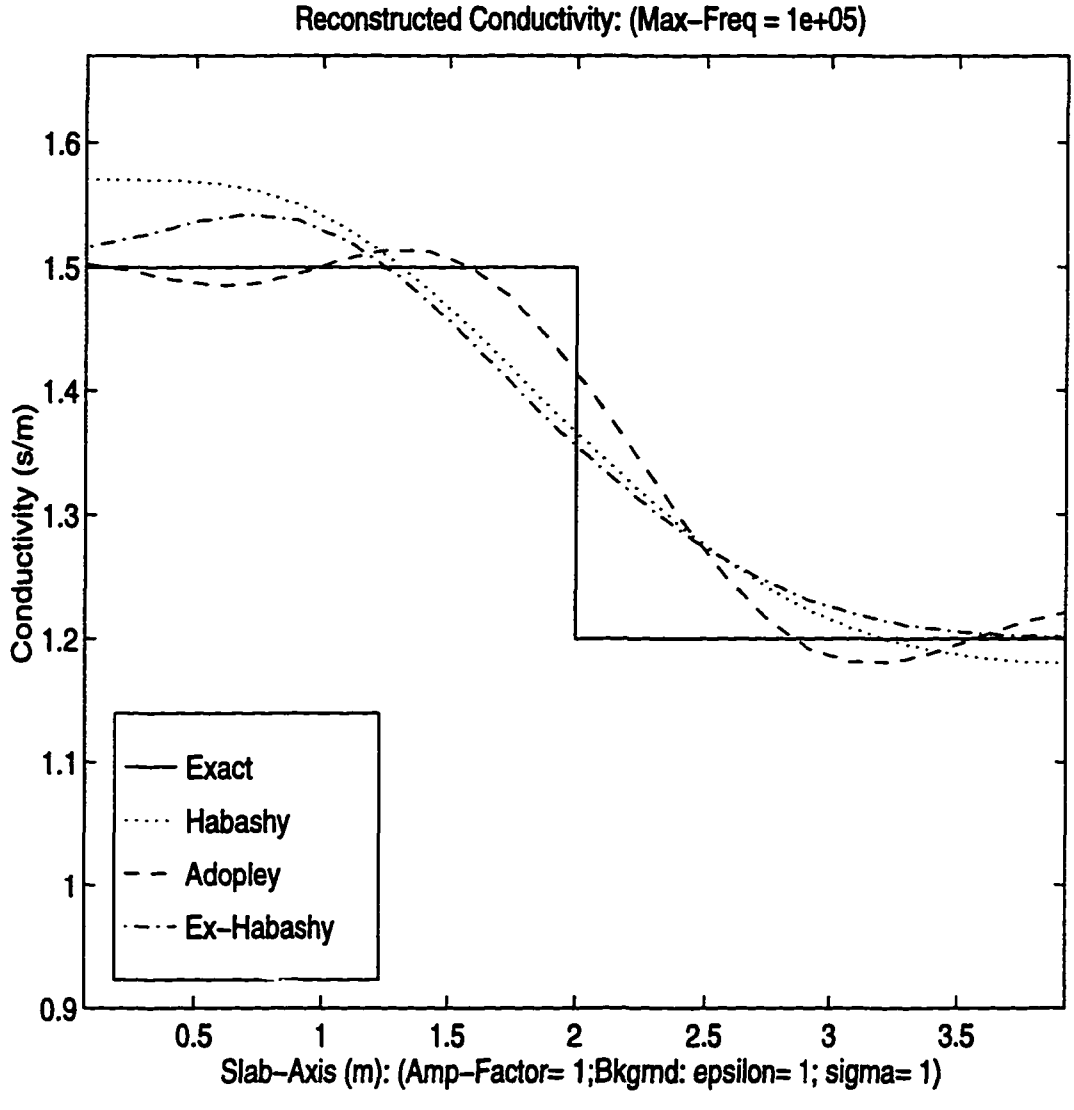

Figure 8.2: Left-Step Profile Reconstruction

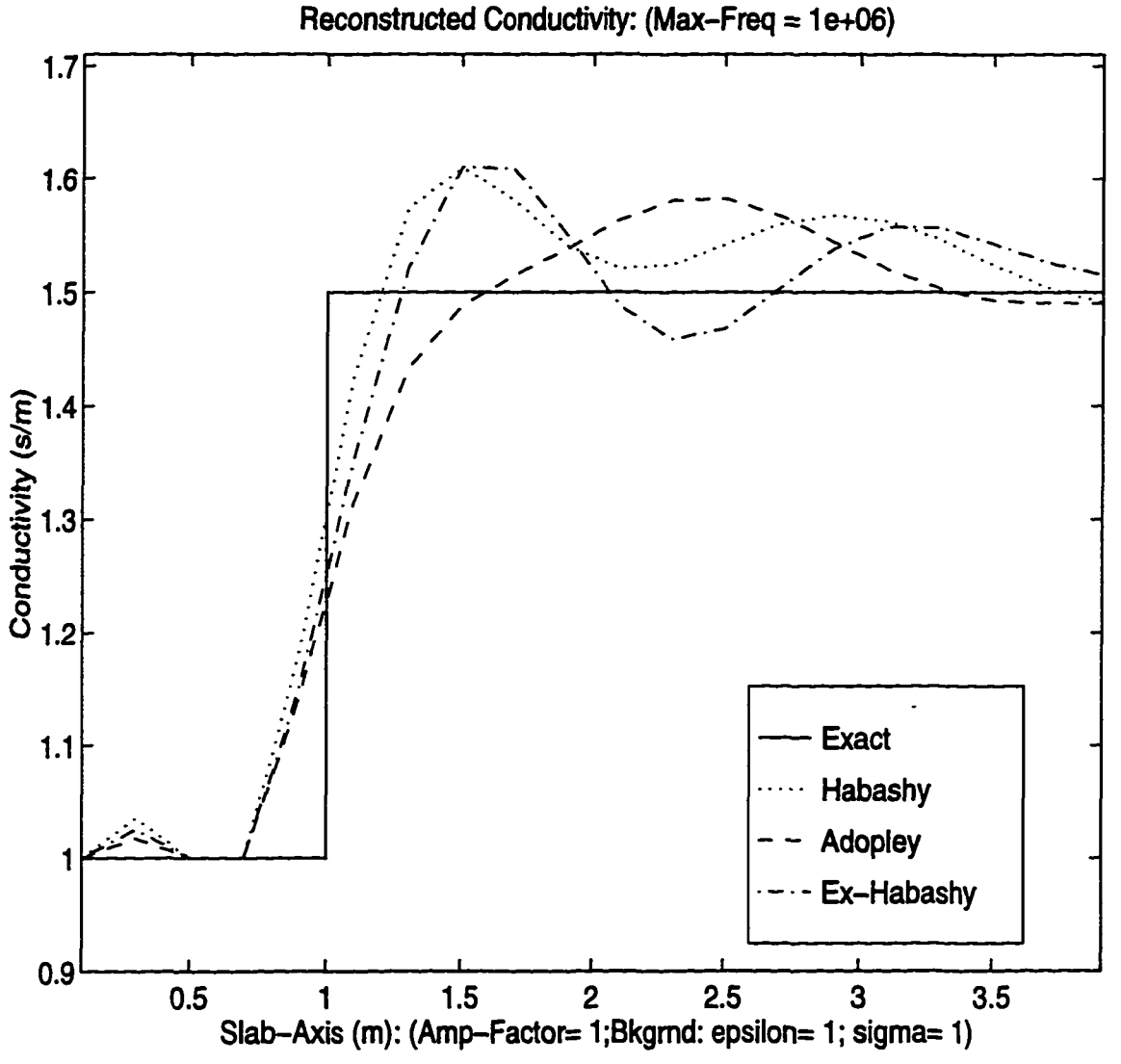

Figure 8.3: Right-Step Profile Reconstruction

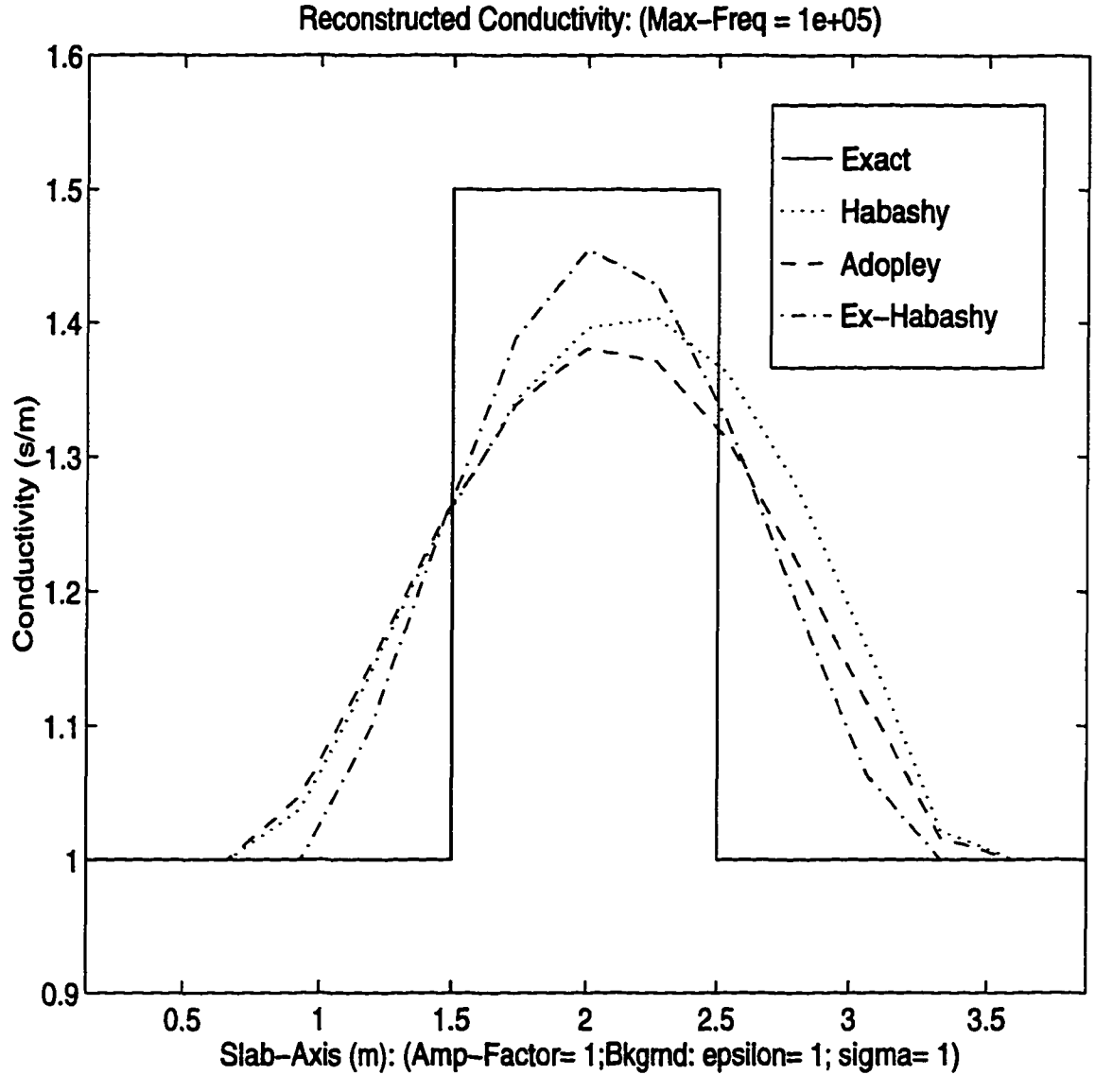

Figure 8.4: Relative Performance of Models in "Inclusion" Profile Reconstruction

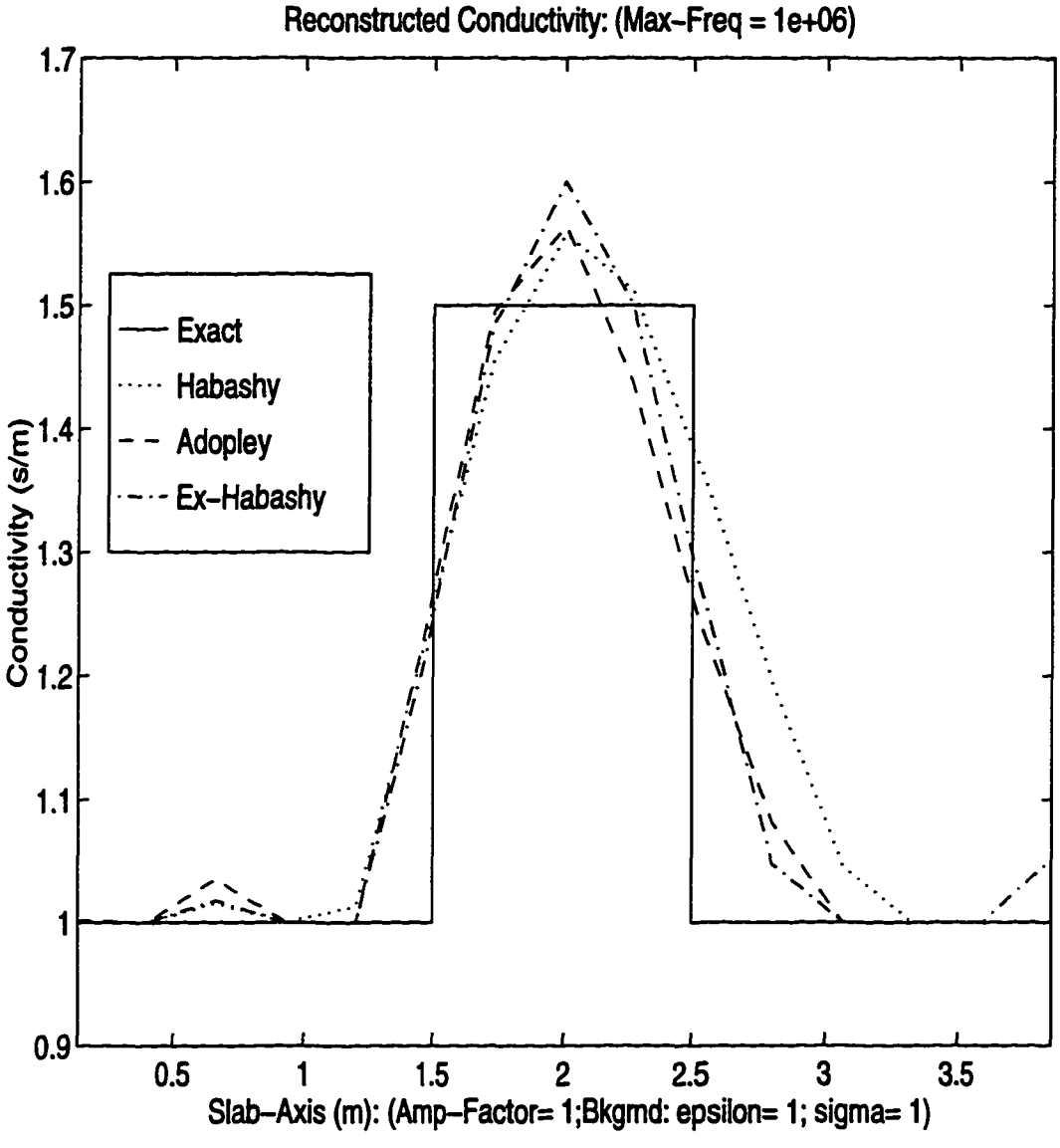

Figure 8.5: Frequency Effect on "Inclusion" Profile Reconstruction

should observe in these two figures that the resolution of the profile reconstruction is sharper at the higher frequency. This is a general trend. Hence, reconstructions should be done at the highest frequency for which convergence is possible. We also note that, at the higher frequency, the Habashy model yields the least resolution for the reconstructed profile. The Habashy model tends to give higher reconstructed values at the higher frequency.

Figures 8.6 and 8.7 show the effects of maximum frequency f_m and the amplification factor in uneven slab partitioning respectively on profile reconstruction. We have employed the "inclusion" profile in these studies. The maximum frequencies of investigation for Figure 8.6 are $0.10MHz$, $0.50MHz$ and $1.0MHZ$. We observe an increase in profile resolution for higher maximum frequencies. We also note higher reconstructed values for higher frequencies. In Figure 8.7 we show reconstruction using different amplification factors in the uneven element slab partitioning. In the figure, the 1-label is for uniform element sizes, where each element is the same size. The 1.02-label shows that the *amplification factor* used in the uneven element slab partitioning is 1.02. This is true also for the 1.05-label. Our observation is that, the element size has very little influence on the magnitude of the predicted values. However, we note a general shift of the reconstructed profile to the right. This we can attribute to the change in the element location due to increase in element size towards the trailing edge of the slab. In general, the uneven elements tend to predict

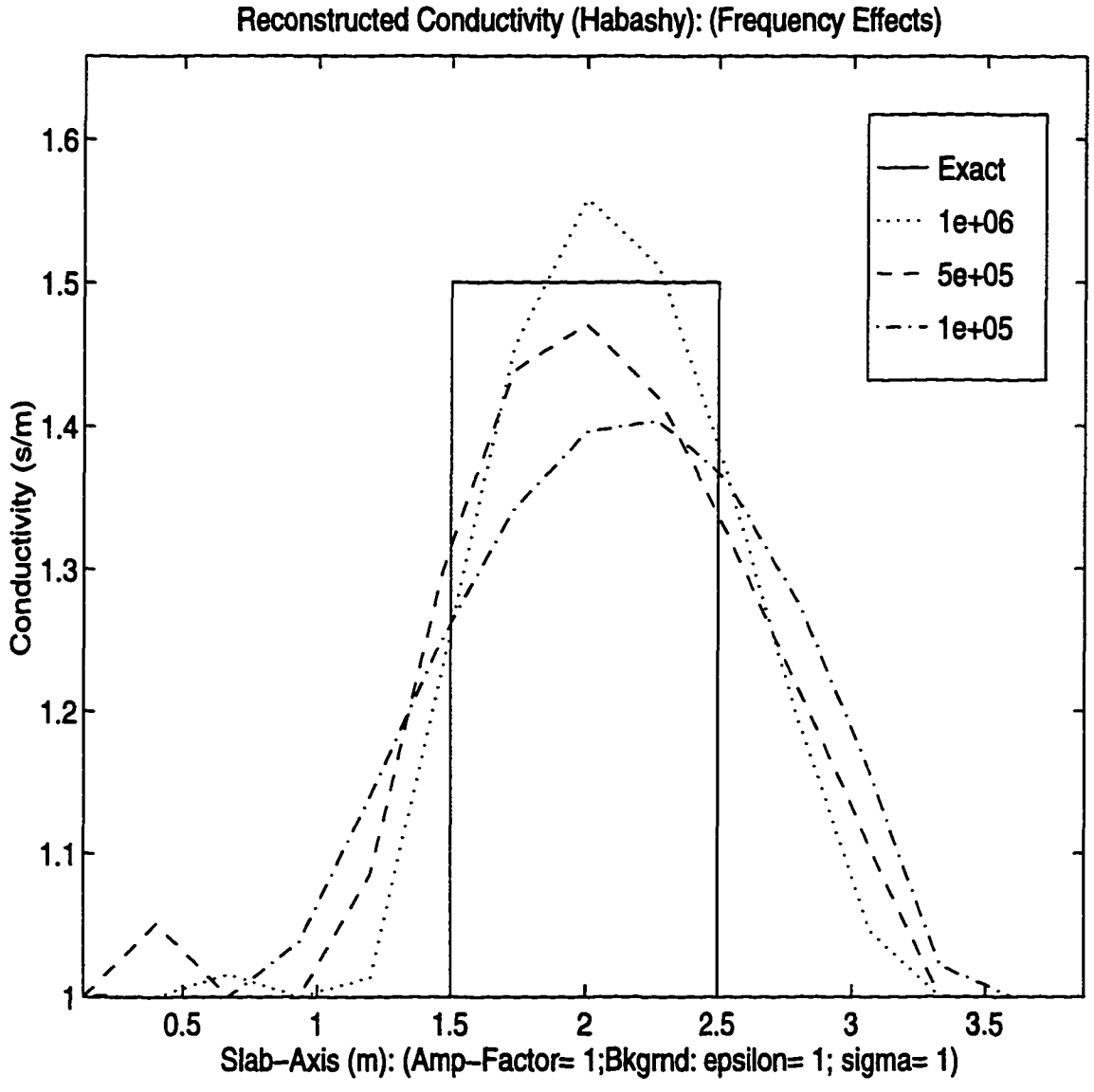

Figure 8.6: Frequency Effect on Profile Reconstruction for Habashy Model

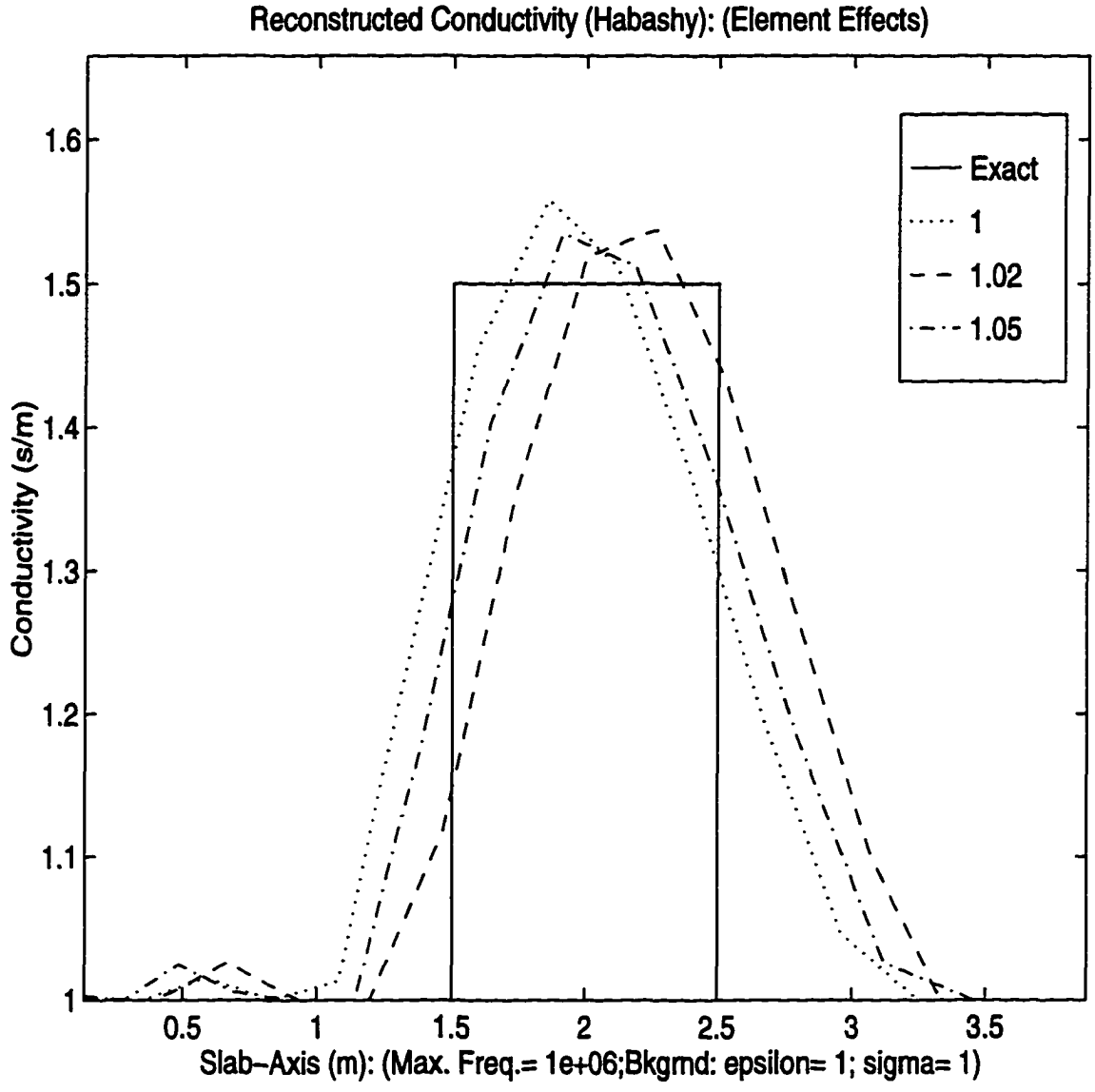

Figure 8.7: Uneven-Partition Element Effects on Profile Reconstruction for Habashy Model

the leading edge of the slab better than the uniform elements but also give a worse prediction of the trailing edge.

Figures 8.8 and 8.9 show plots of frequency and uneven elements effects respectively for the Adopley model. The observations noted for the Habashy model also hold for the Adopley model. In addition we note a close prediction for the $0.5MHz$ and $1.0MHz$ results. The maximum overshoot above the exact profile appears to be less for the Adopley model. The next two plots in Figures 8.10 and 8.11 show the same frequency and uneven elements effects for the Extended-Habashy model. The general trend observed for the Adopley and Habashy models also apply to the Extended-Habashy model.

The last three figures presented for the piecewise constant profile are for comparing the relative performance of the individual models. The profile for Figure 8.12 is more complex than those of our previous investigation. It is a combination of right-step, inclusion and left-step. The reconstruction is fairly accurate not withstanding the complexity of the profile. We note a larger oscillation about the true profile for the Extended-Habashy and Habashy models. The Adopley model predicted a smoother profile. All models predict the general contour of the conductivity profile fairly well. In Figure 8.13 the "inclusion" is reversed to produce a depression in the conductivity profile. The three models were able to indicate the conductivity depression quite accurately. However we observed some distinct differences in each model performance. The Adopley model predicts the conductivity profile at the slab leading

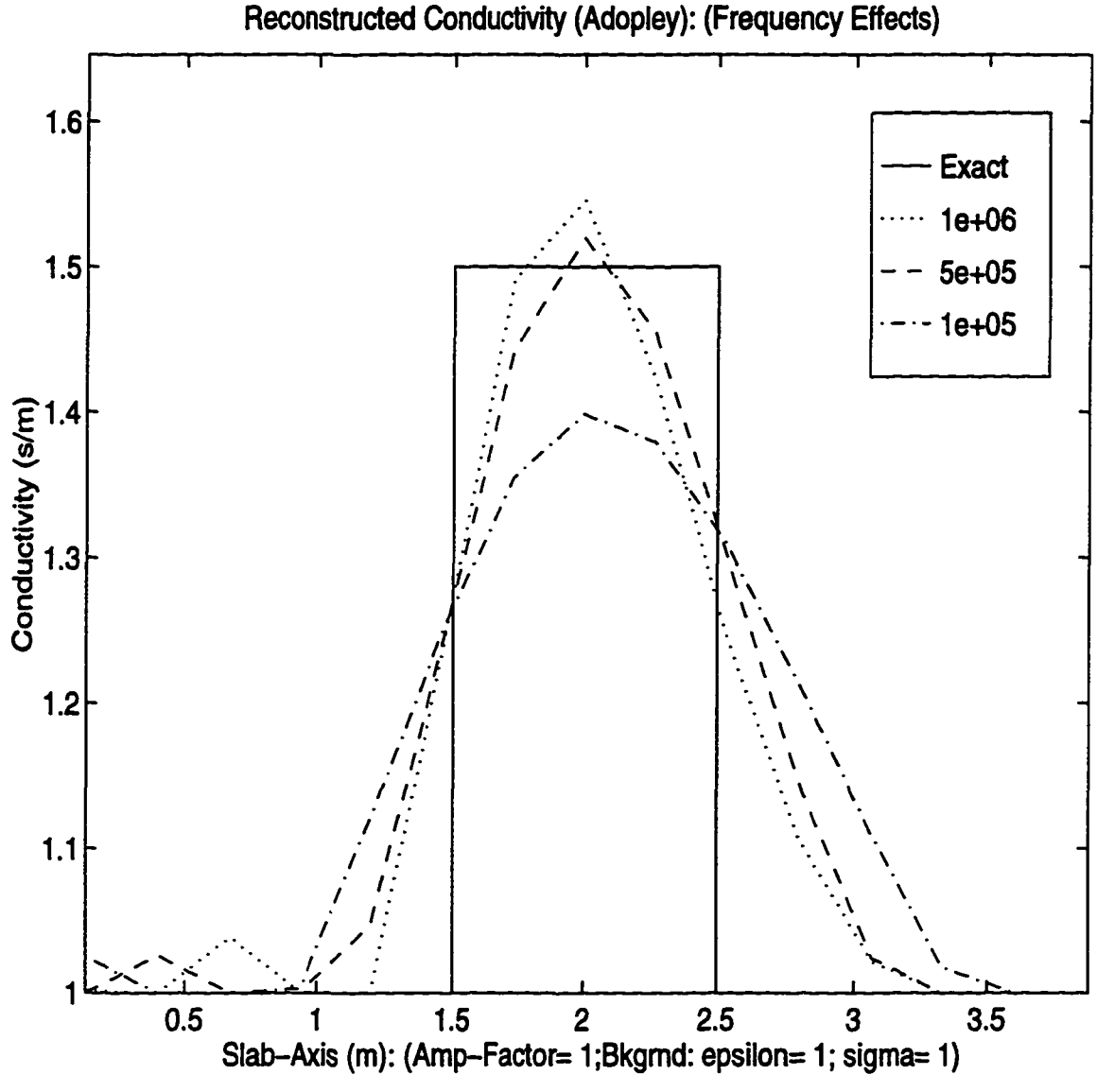

Figure 8.8: Frequency Effect on Profile Reconstruction for Adopley Model

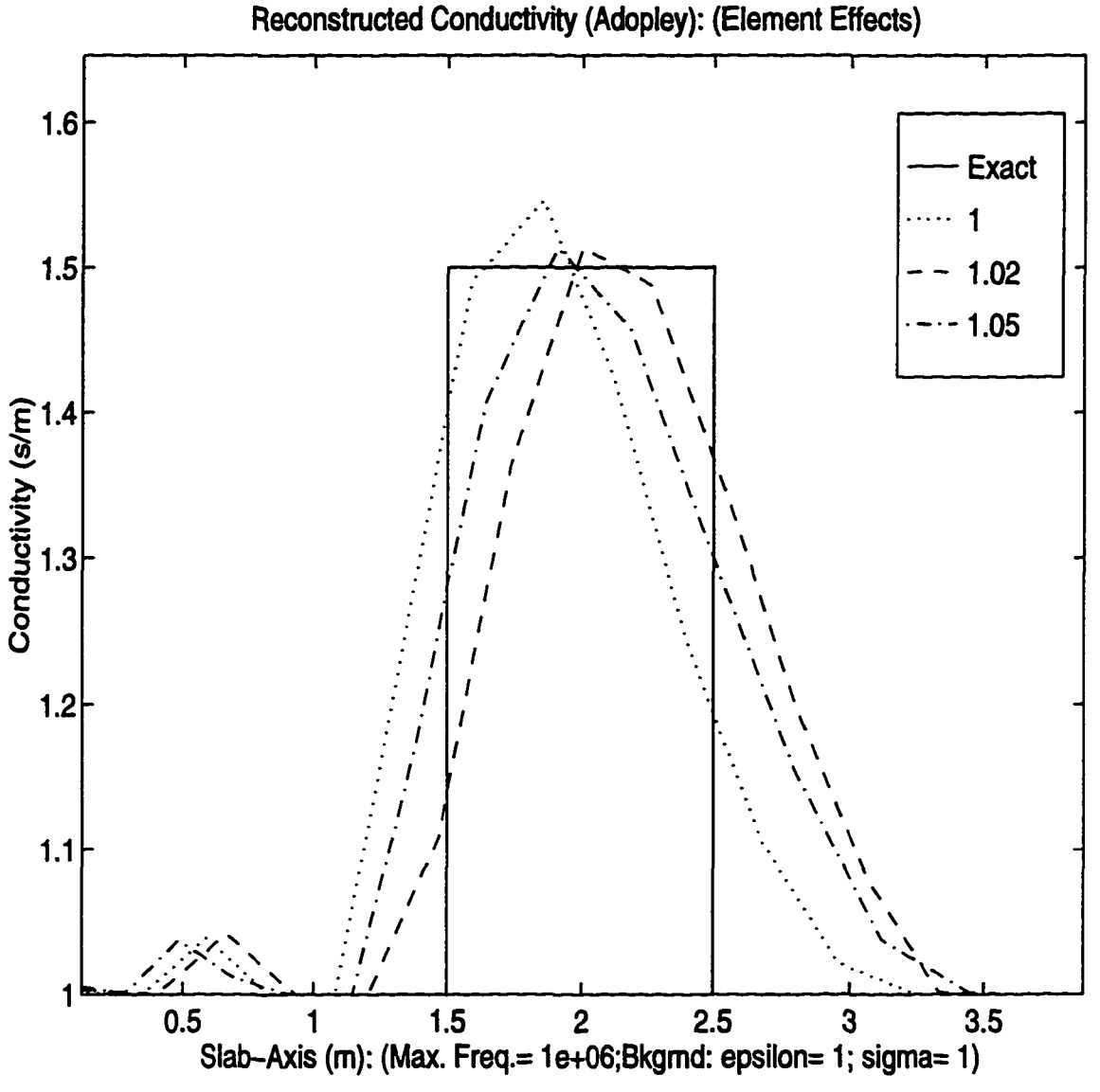

Figure 8.9: Uneven-Partition Element Effects on Profile Reconstruction for Adopley Model

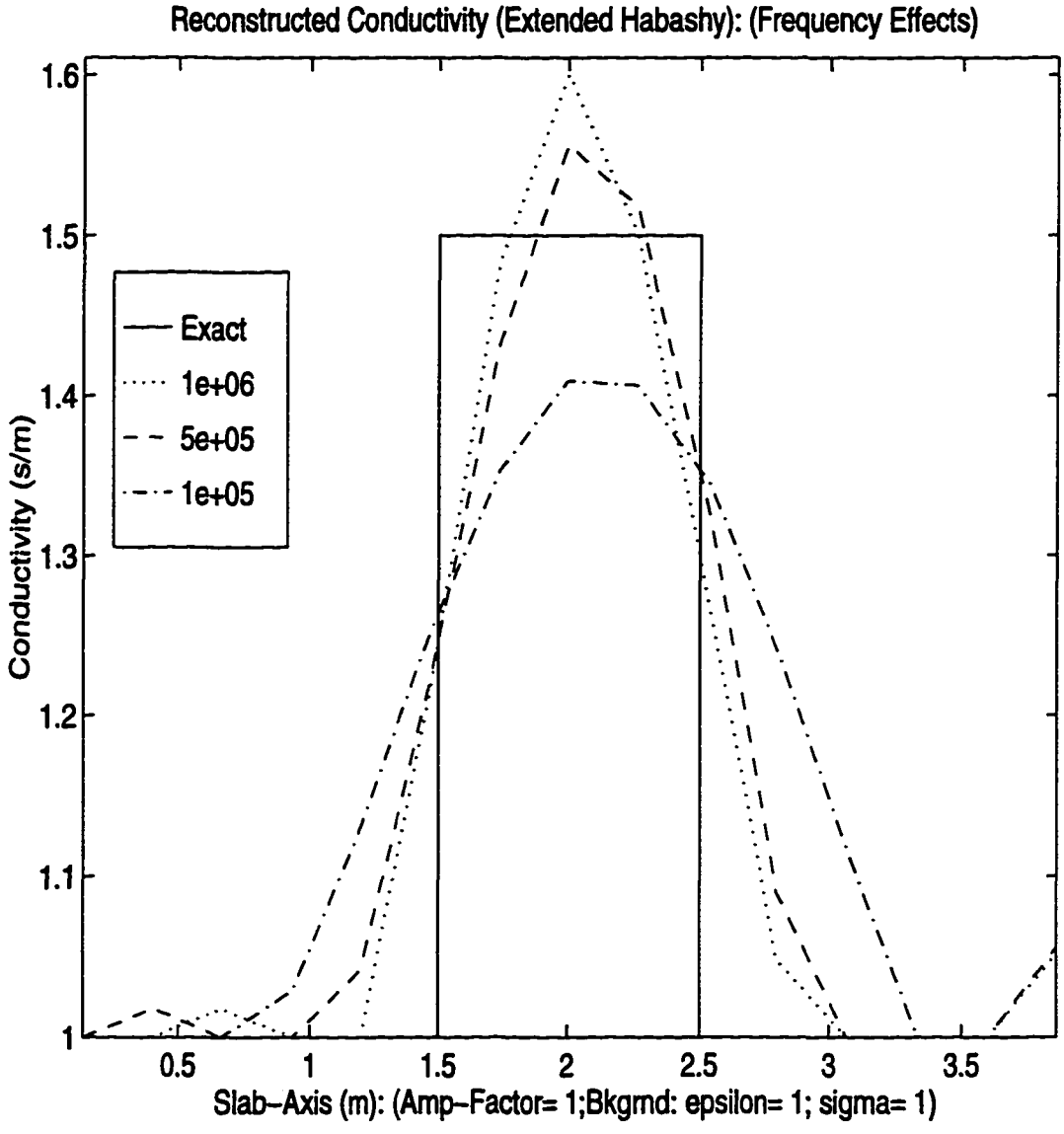

Figure 8.10: Frequency Effect on Profile Reconstruction for Extended-Habashy Model

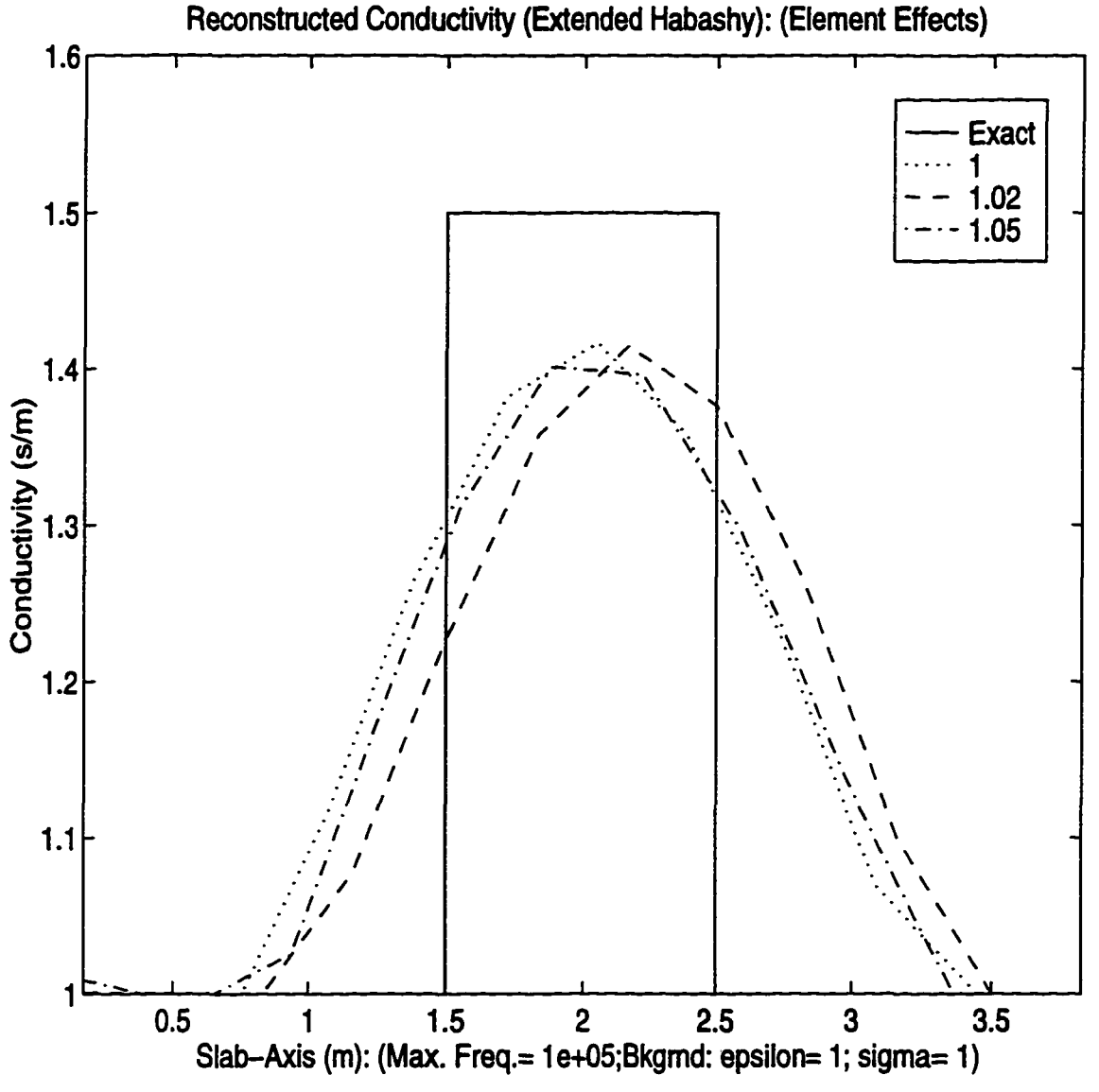

Figure 8.11: Uneven-Partition Element Effects on Profile Reconstruction for Extended-Habashy Model

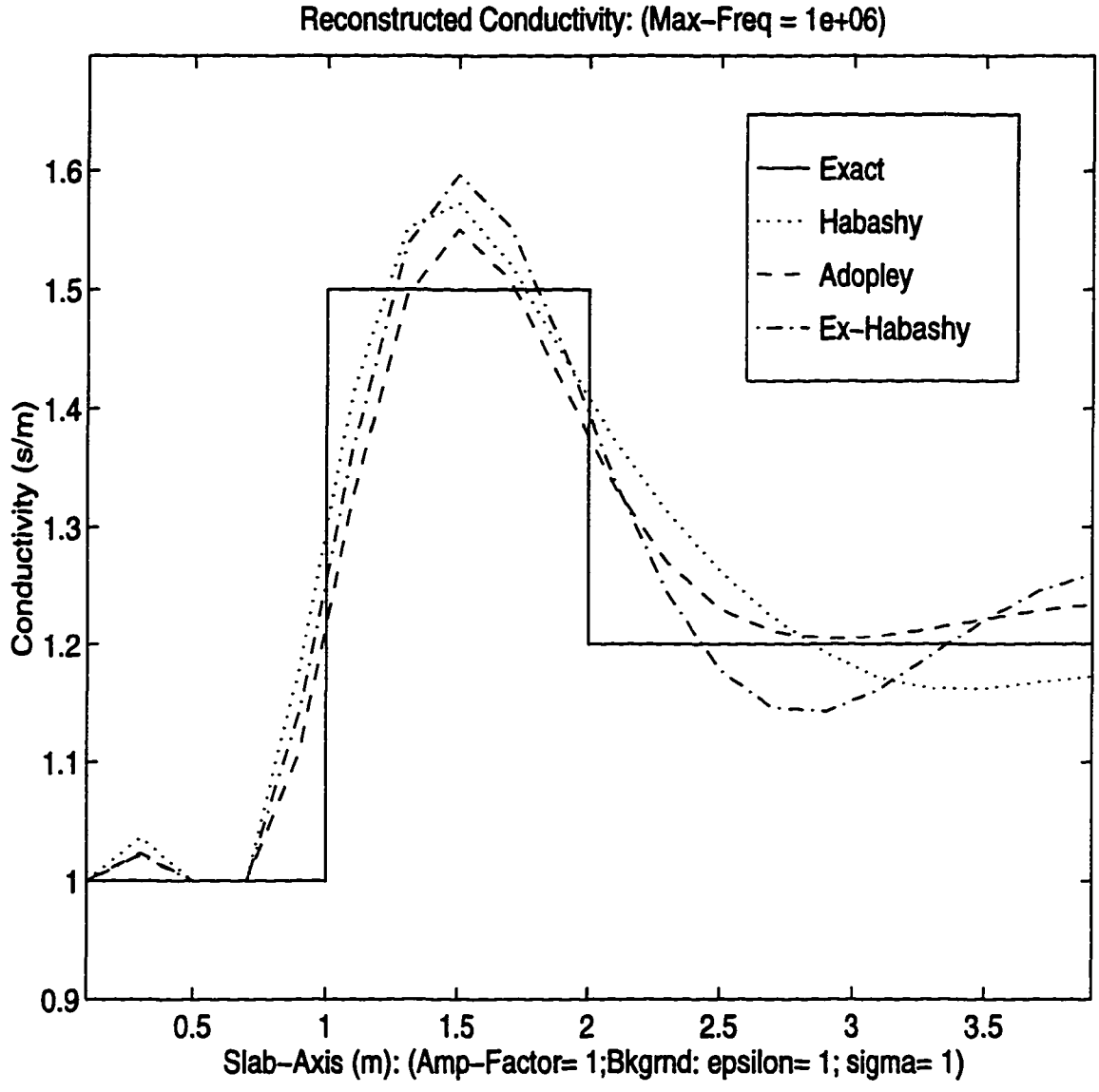

Figure 8.12: Complex Profile Reconstruction

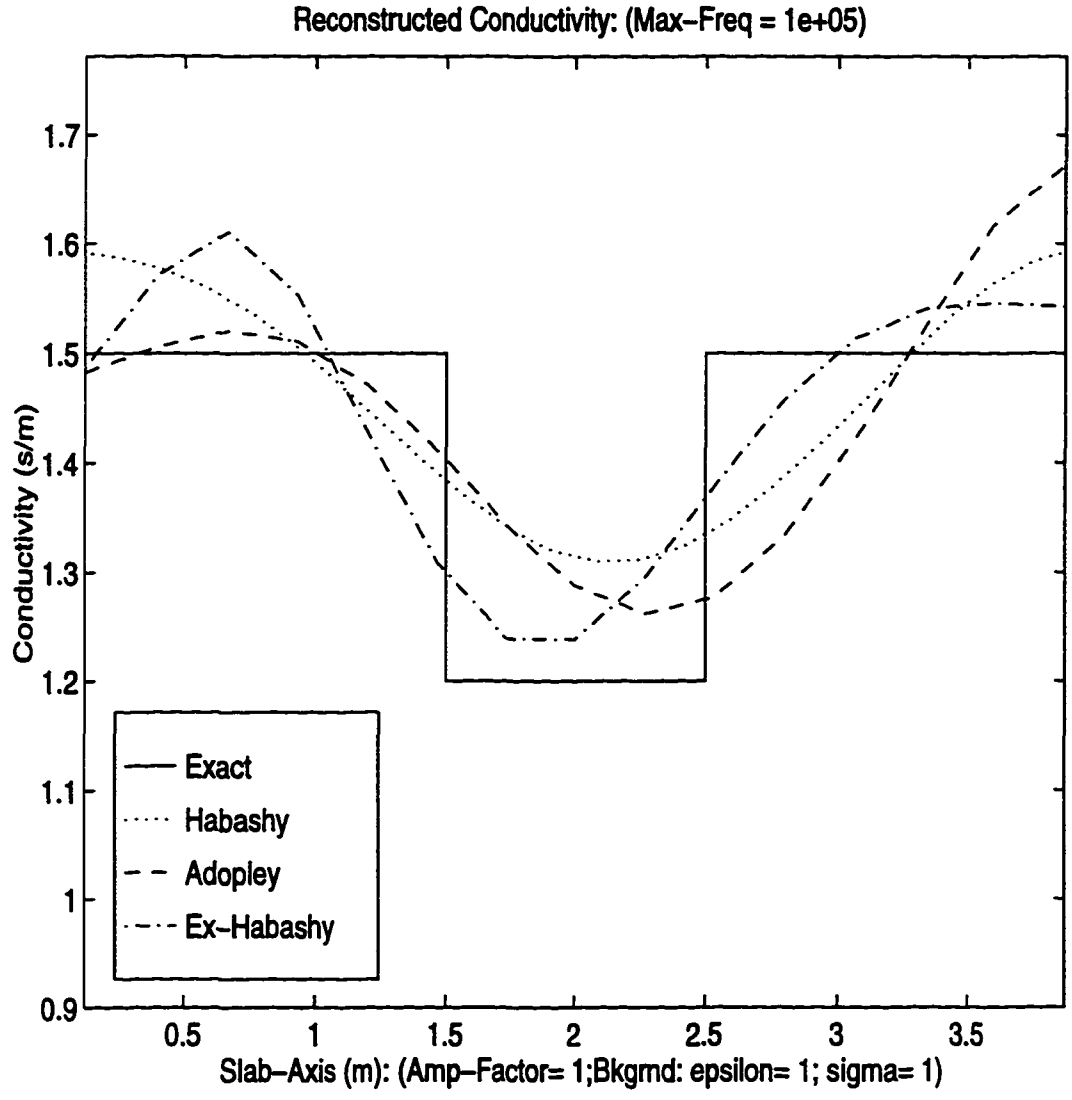

Figure 8.13: Inverse Profile Reconstruction

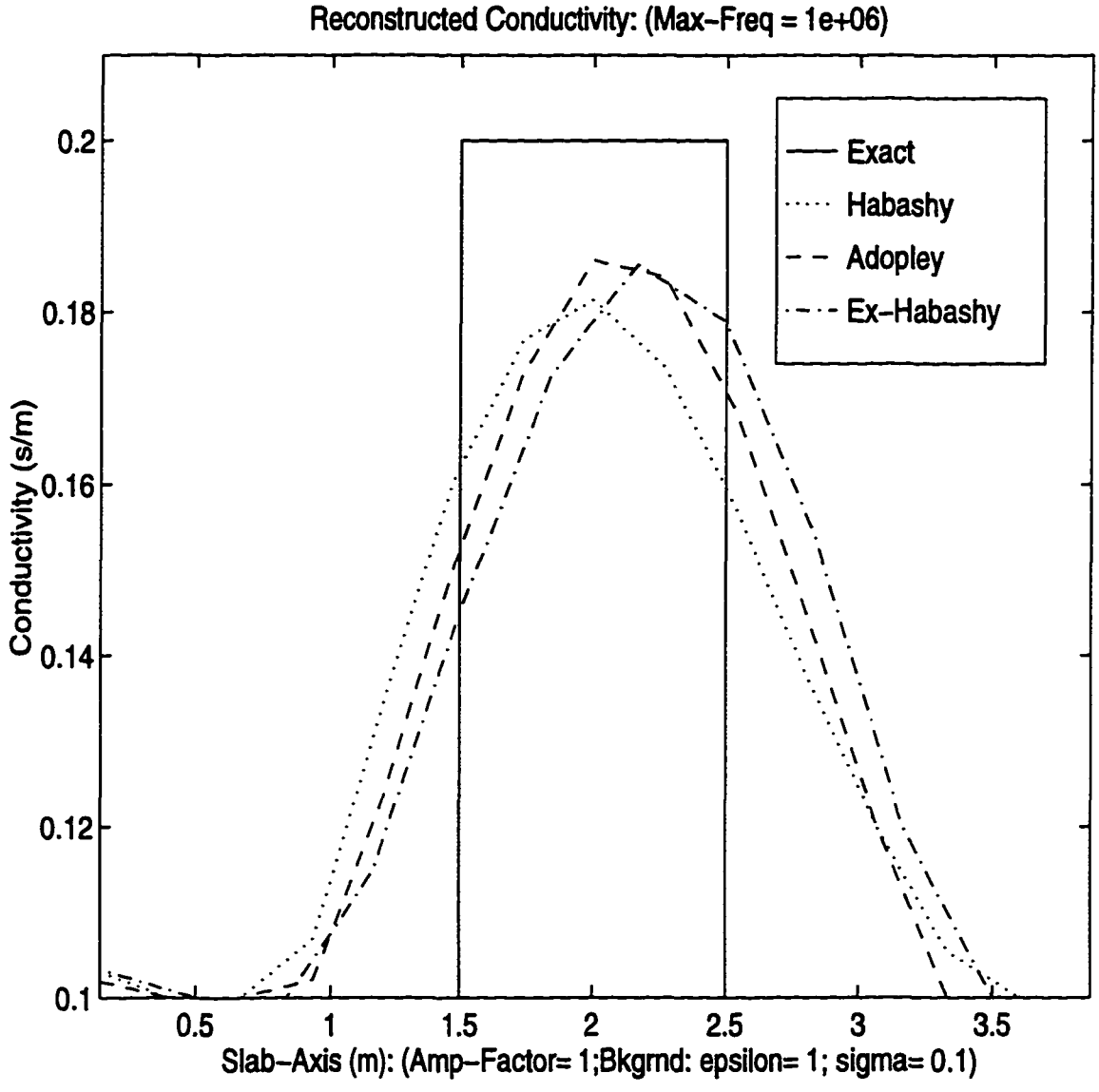

Figure 8.14: Background Complex Conductivity Effects on Profile Reconstruction

edge better than the Habashy and the Extended-Habashy models. However, at the slab trailing edge, the Habashy and the Extended Habashy predicted better results. The Extended-Habashy predicts the σ depression with a little shift to the left while the Adopley and the Habashy predict with a little shift to the right. In Figure 8.14 we investigated the effect of background conductivity on model performance. The three models predicted roughly the same results. The Habashy model predicted a peak value a little less than the other models. However we also observe that all the models predicted peak values less than the actual peak values at maximum frequency of $1.0MHz$ employed in the investigation. This is a general observation that for very low conductivity background, we require higher maximum frequencies for accurate profile reconstruction. We also note that with lower conductivity background, the range of conductivity contrast reconstruction increases. All the observations noted above are fundamentally governed by the maximum frequency at which each model is capable of accurate field simulation. It was generally observed that if the model cannot simulate the field accurately at all the sampling frequencies used, then we experience instabilities in reconstruction. In the next section we present our results of conductivity reconstruction for the linear profile.

8.2 Linear profile reconstruction

The linear profile reconstruction was performed on synthetic measured data, simulated using the Habashy approximation. As we recall, the exact solution of the

linear profile was obtained in terms of *Airy* functions of the first and second kinds. For complex arguments, it was impossible to generate accurate and reliable results from the numerical routines available to us. Furthermore, we could not obtain tabulated results of any kind for the *Airy* functions with complex arguments. Hence it was practically impossible to attach any validity to numbers generated with complex arguments. In the light of this we felt obliged to adopt one of the approximation routines for use in generating the measured data. Our logical choice was the Habashy approximation which is the very basis of this work. It is therefore imperative to keep in mind that our synthetic measured data have some inherent threshold error from the approximate simulation.

As was the case for the piecewise constant profile, we added 5% noise to the generated measured data. This sets the minimum contamination noise-level at 5%. The inversion was performed using all three approximate formulations. The present inversion was limited to real conductivity profiles of the slab ($\epsilon_s = \epsilon_b$). The first two illustrations in Figures 8.15 and 8.16 show the relative performance of the individual approximations for two different background and conductivity slopes. The homogeneous background has $\epsilon = 1$, $\sigma = 0.10$ in Figure 8.15 and $\sigma = 1.0$ in Figure 8.16. The slab has $\epsilon = 1$ and σ-slope of $0.002 s/m^2$ in Figure 8.15 and $0.1 s/m^2$ in Figure 8.16. The maximum frequencies used are $1.0 MHz$ for Figure 8.15 and $0.1 MHz$ for Figure 8.16. All parameters used in the inversion are shown in the figures. It is interesting to note that, even though the data are simulated using the Habashy

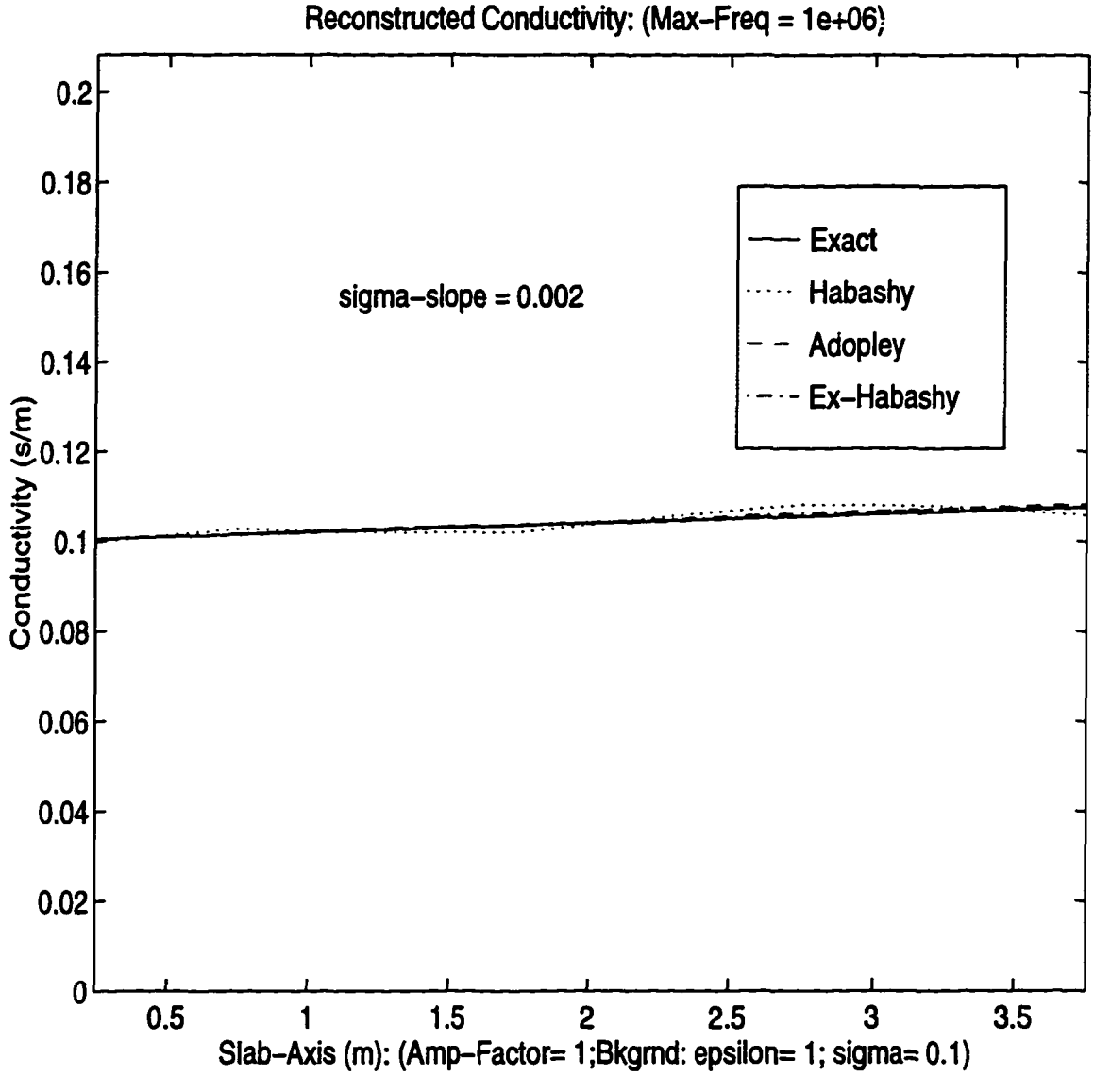

Figure 8.15: Model Accuracies in Profile Reconstruction

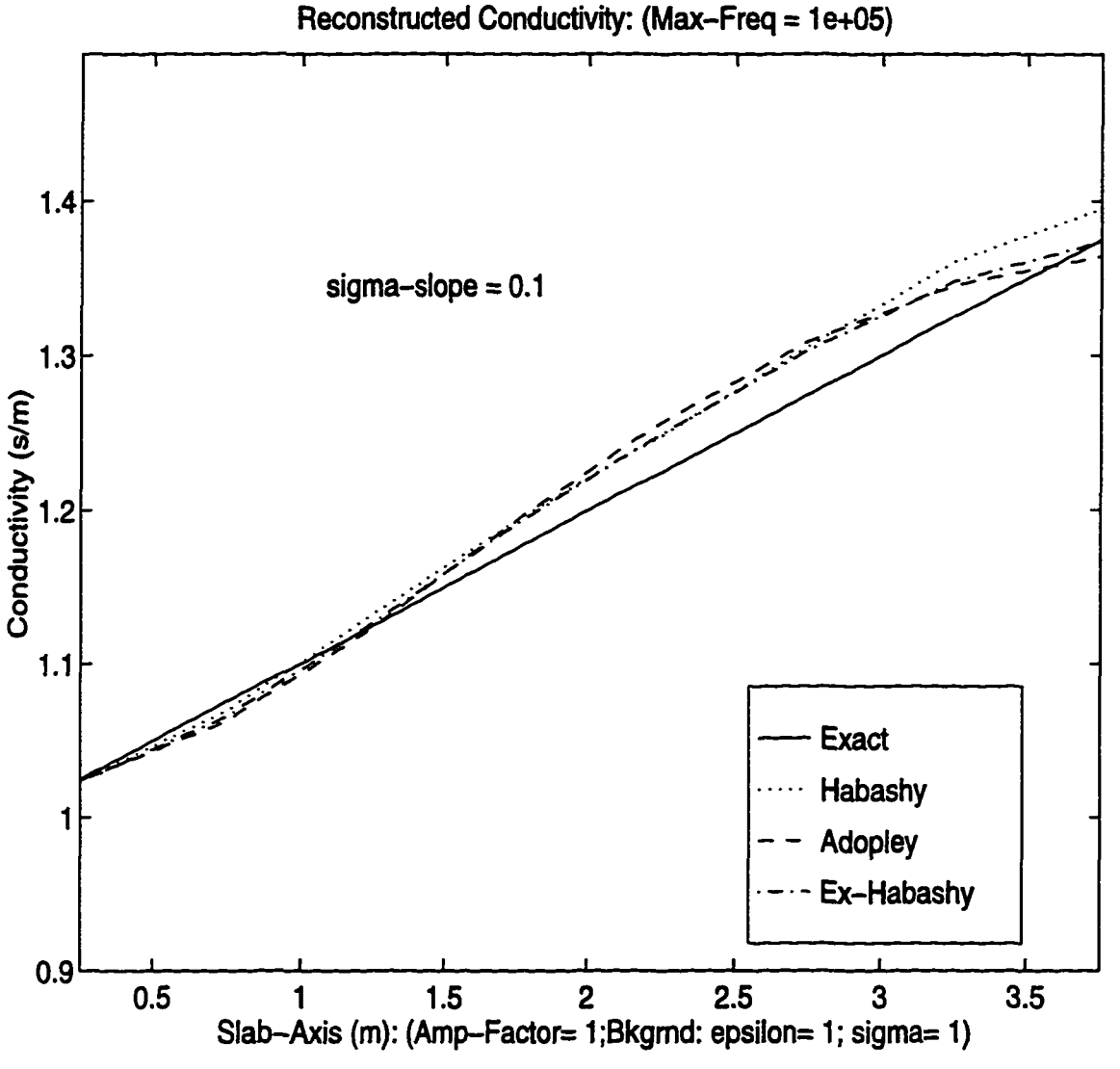

Figure 8.16: Effect of Complex σ-Gradient on the Accuracy of Models in Profile Reconstruction

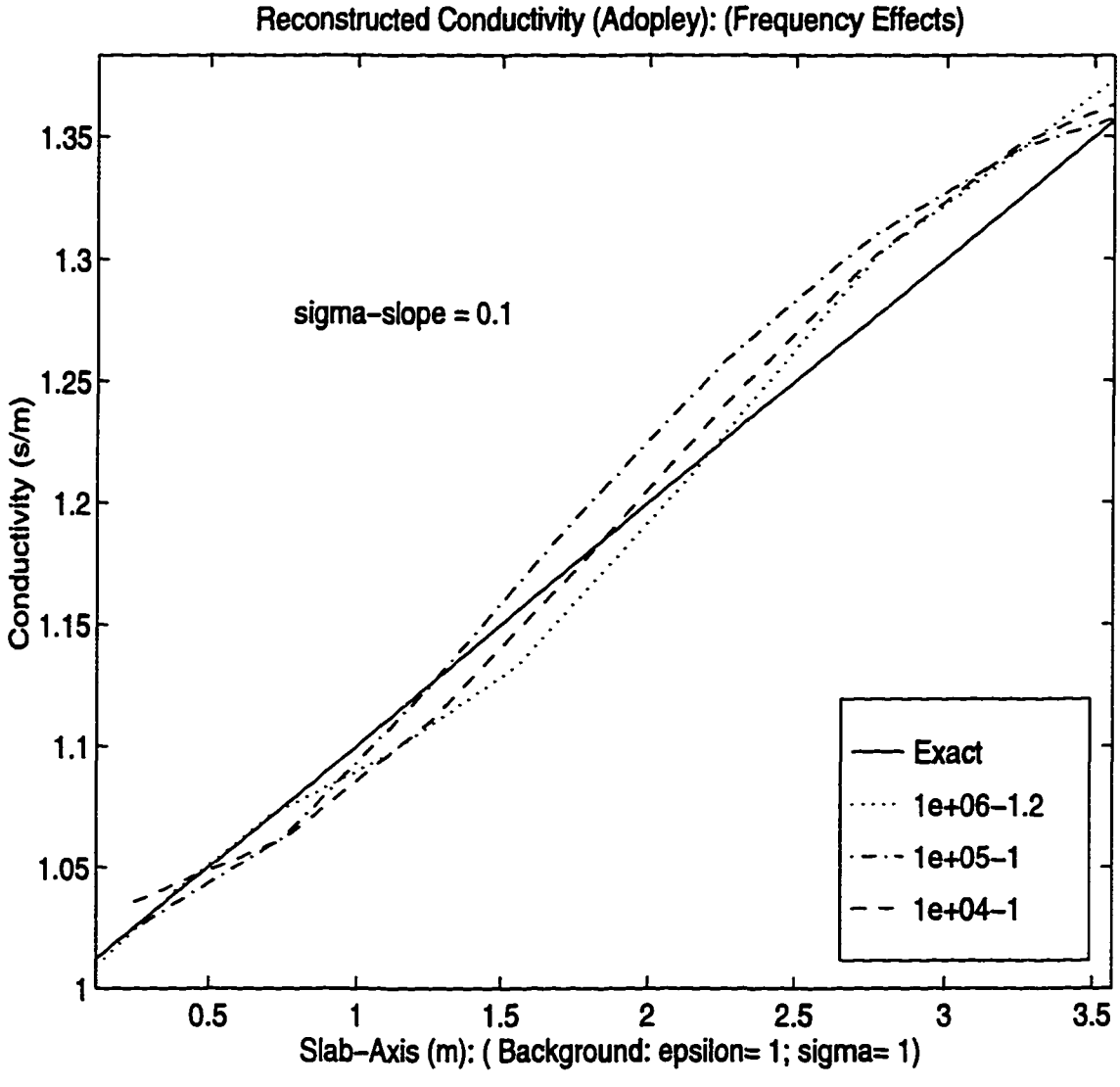

Figure 8.17: Frequency Effects on Profile Reconstruction Using the Adopley Model

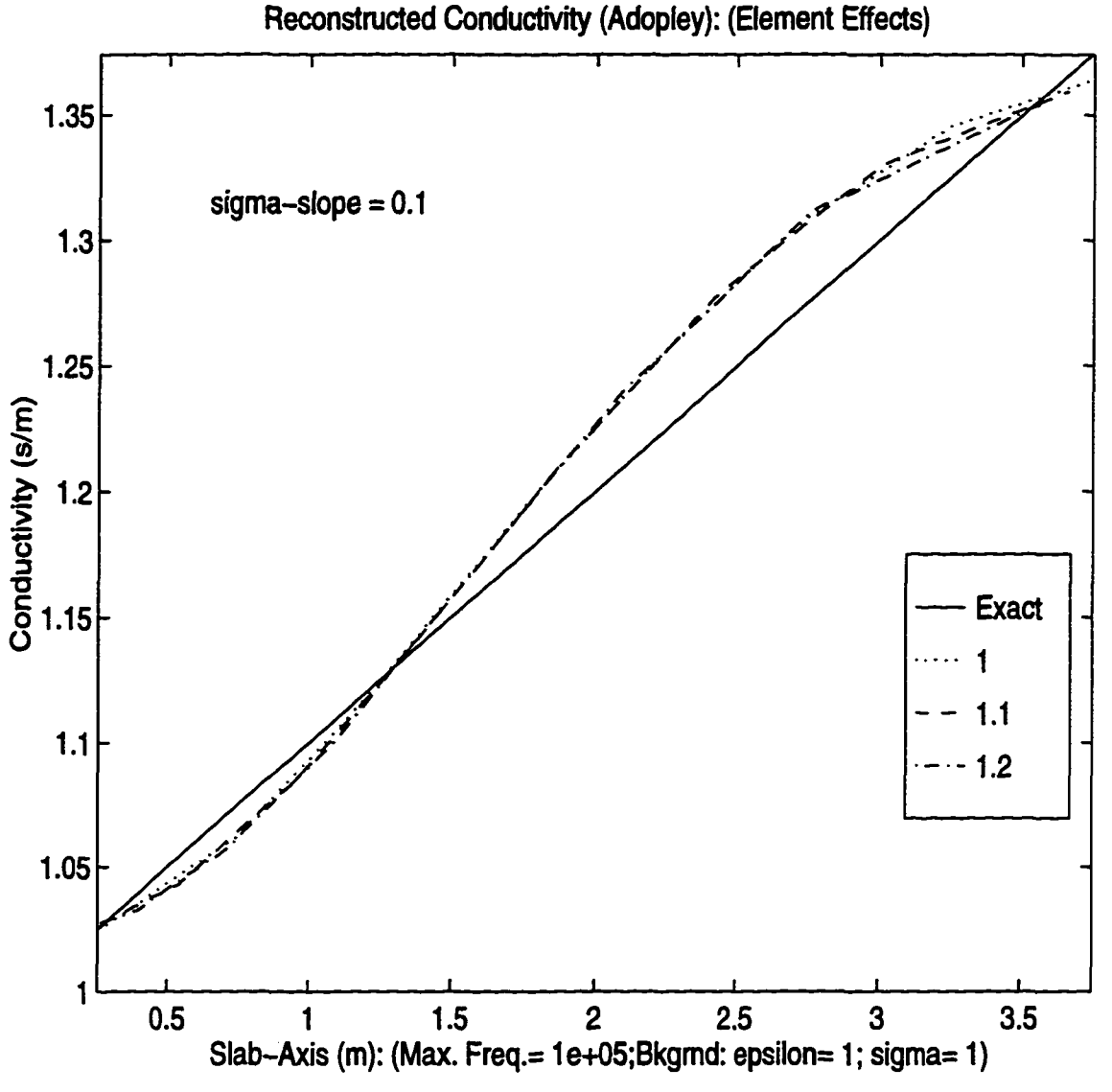

Figure 8.18: Uneven-Partition Element Effects on Profile Reconstruction Using the Adopley model

approximation, the Adopley and the Extended Habashy approximation produced a more accurate reconstruction in Figure 8.15. In Figure 8.16, the reconstruction is very similar for all models. Figures 8.17 and 8.18, show the effects of frequency and uneven partition element-size on the reconstruction respectively for the Adopley model. In Figure 8.17, the legend has two numbers below the exact-profile label. The first number is the maximum frequency of reconstruction, and the second number is the *amplification factor* applied in the uneven element partitioning of the slab. The amplification number signifies the minimum element amplification for which reasonable reconstruction can be obtained. We observed that, for higher frequencies of reconstruction, element amplification becomes important for reasonable reconstruction. From our plots, we note that the accuracy of reconstruction tends to be better at higher frequencies when the accuracy of the simulated data is within the error limit. In Figure 8.18, the maximum frequency of reconstruction is $0.1MHz$ and we note that the amplification factor does not make much difference in the accuracy of reconstruction.

Frequency and partition element-size effects on reconstruction are shown for the Habashy model in Figures 8.19 and 8.20 respectively. In Figure 8.19 we note better reconstruction at lower frequencies. However, we also note that the amplification factor is the same at all frequencies of reconstruction. The influence of amplification factor is negligible at the frequency of reconstruction show in Figure 8.20.

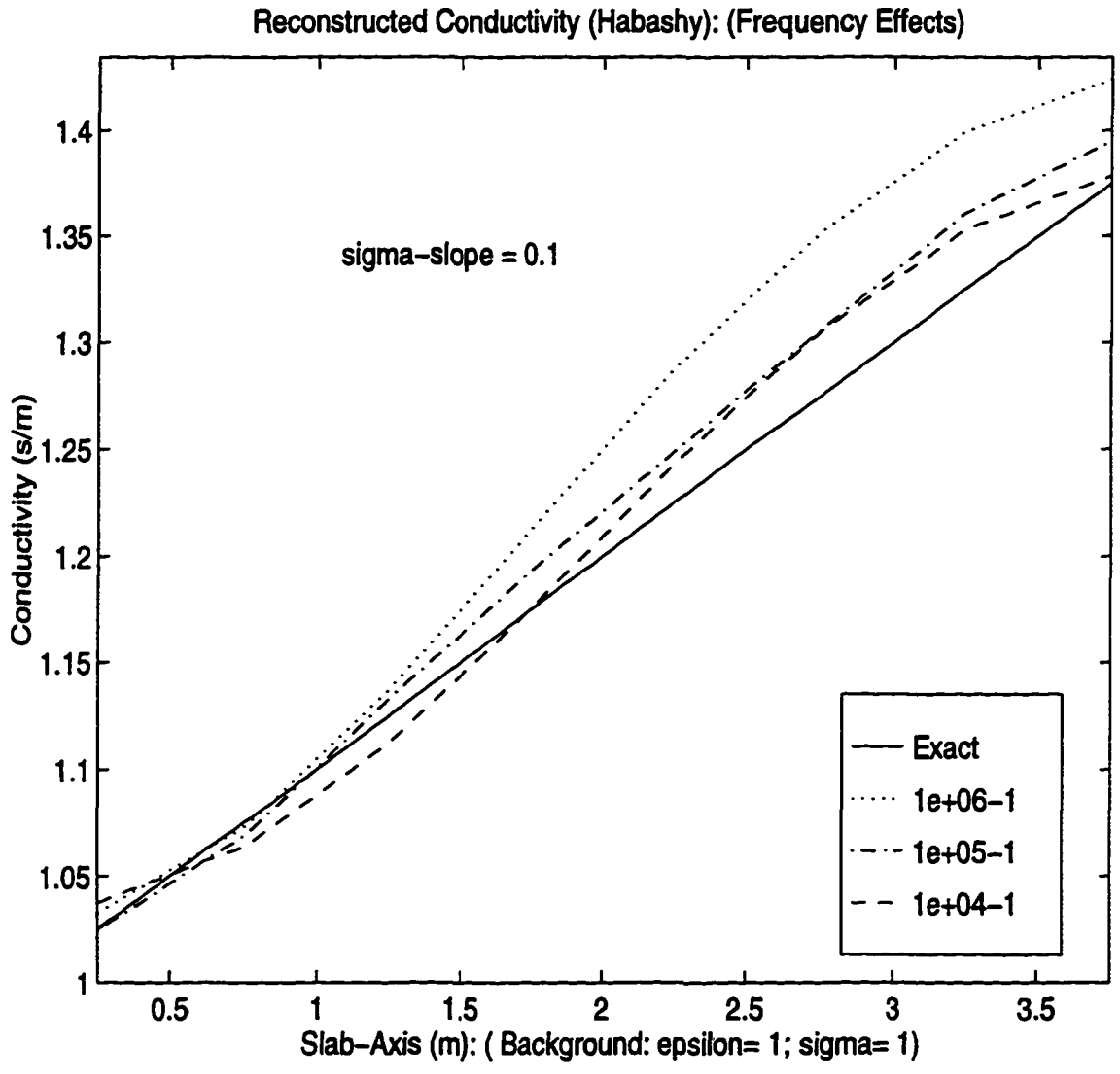

Figure 8.19: Frequency Effects on Profile Reconstruction Using the Habashy Model

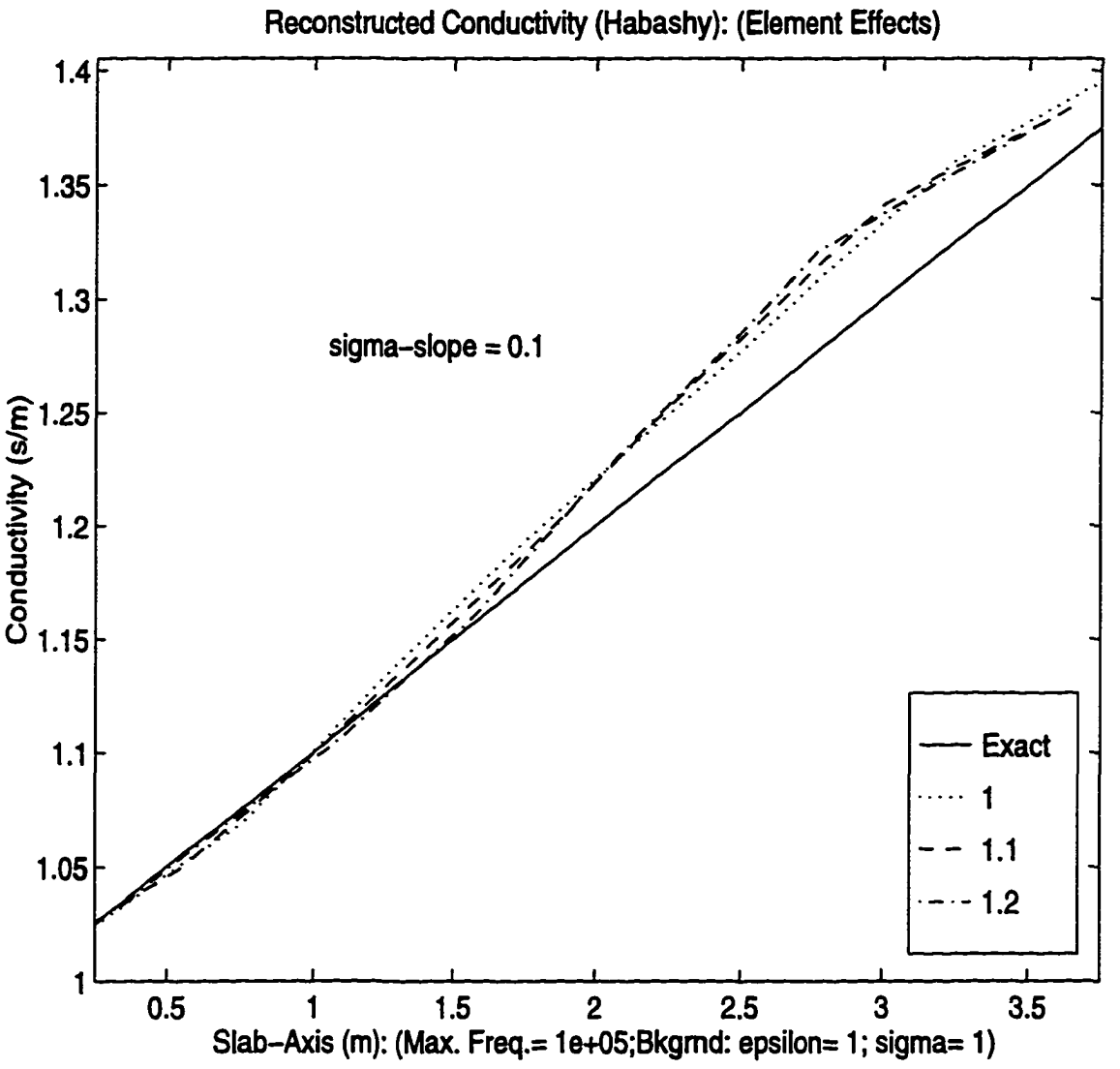

Figure 8.20: Uneven-Partition Element Effects on Profile Reconstruction Using the Habashy Model

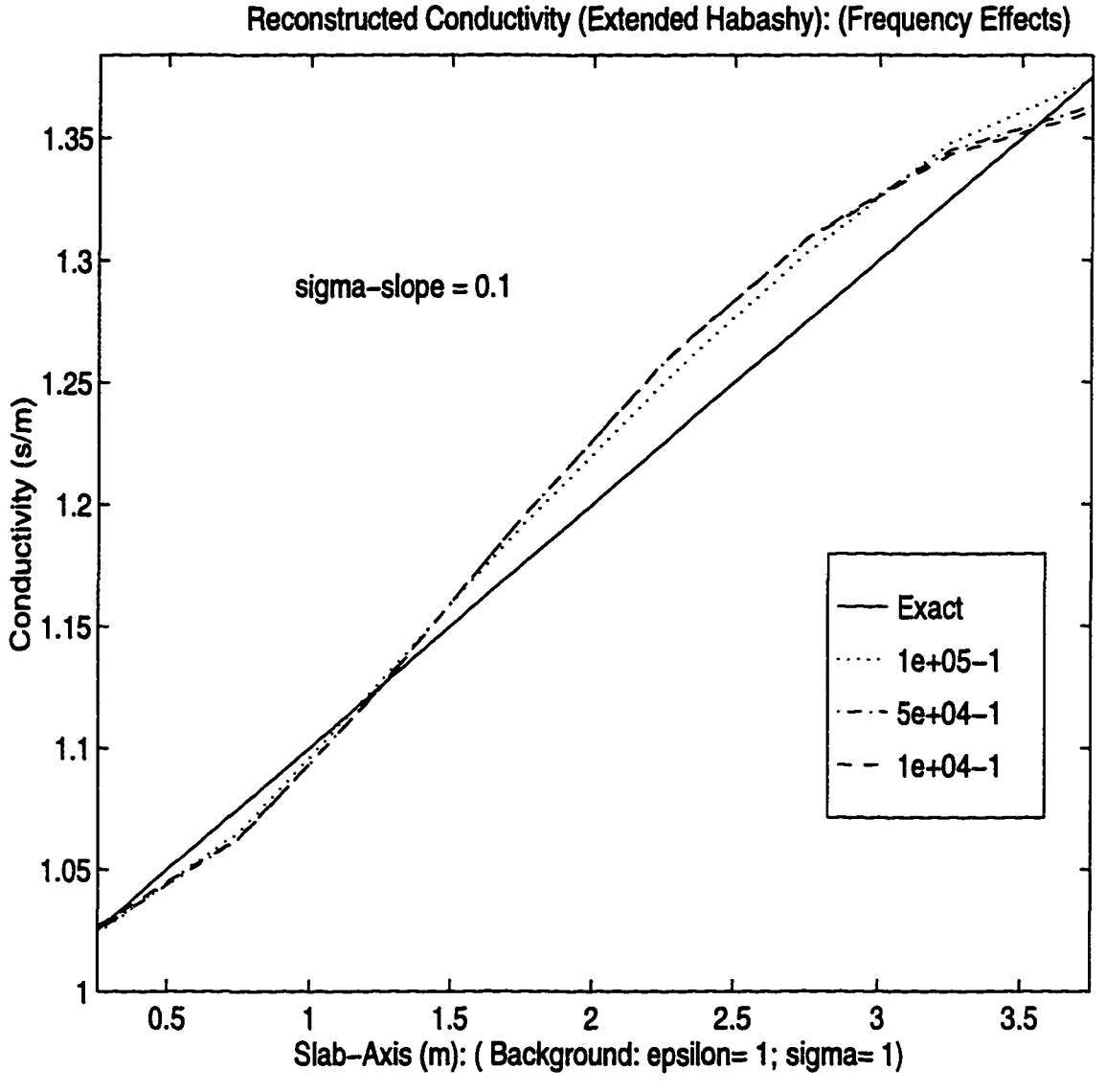

Figure 8.21: Frequency Effects on Profile Reconstruction Using the Extended Habashy Model

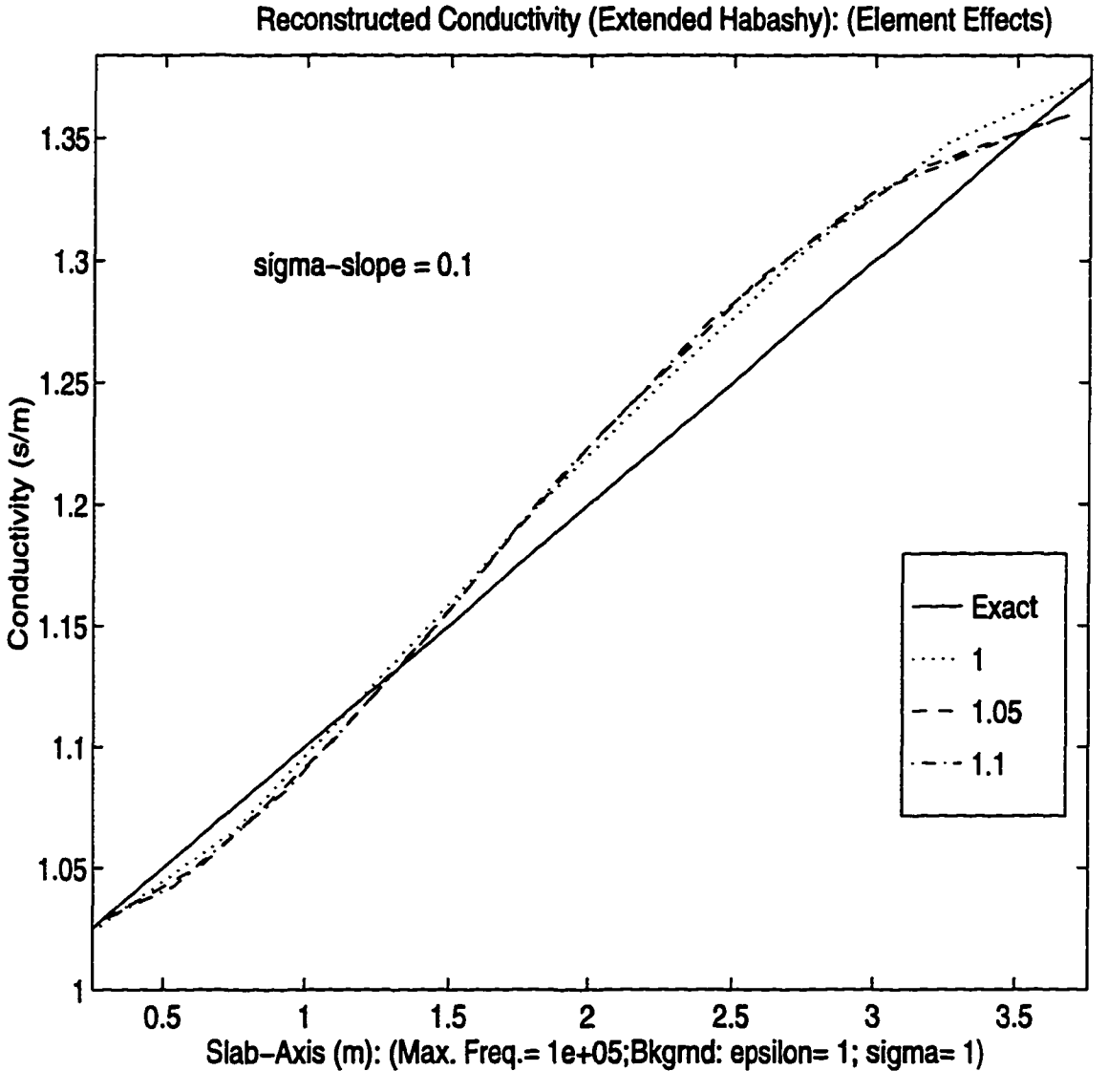

Figure 8.22: Uneven-Partition Element Effects on Profile Reconstruction Using the Extended Habashy Model

A set of plots showing the effects of frequency and partition element-size are given in Figures 8.21 and 8.22 for the Extended Habashy model. In Figure 8.22, the amplification factors are lower than those used for the Habashy and Adopley models. This is due primarily to instabilities when higher amplification factors are used. We observe that the uniform partition appears to provide better reconstruction. We particularly note that the Extended Habashy is the most prone to numerical error. This we attribute to the double numerical integration required. This is also responsible for the model being the slowest.

The last plot presented in Figure 8.23 shows a typical rate of convergence using the Adopley model. The maximum frequency of reconstruction is $0.1MHz$. The background medium has $\epsilon_b = 1.0$ and $\sigma_b = 1.0s/m$. The conductivity profile of the slab has a slope of $0.1s/m^2$. The slab has a width of $4.0m$. The number of elements is 8 which are of uniform size. From *chi* statistics, the expected value is 8.0 and one of the conditions for convergence is $chi < 8.0$. We note that after the first iteration, the χ value is 11.27 and 0.06676 after the second iteration when the routine converges.

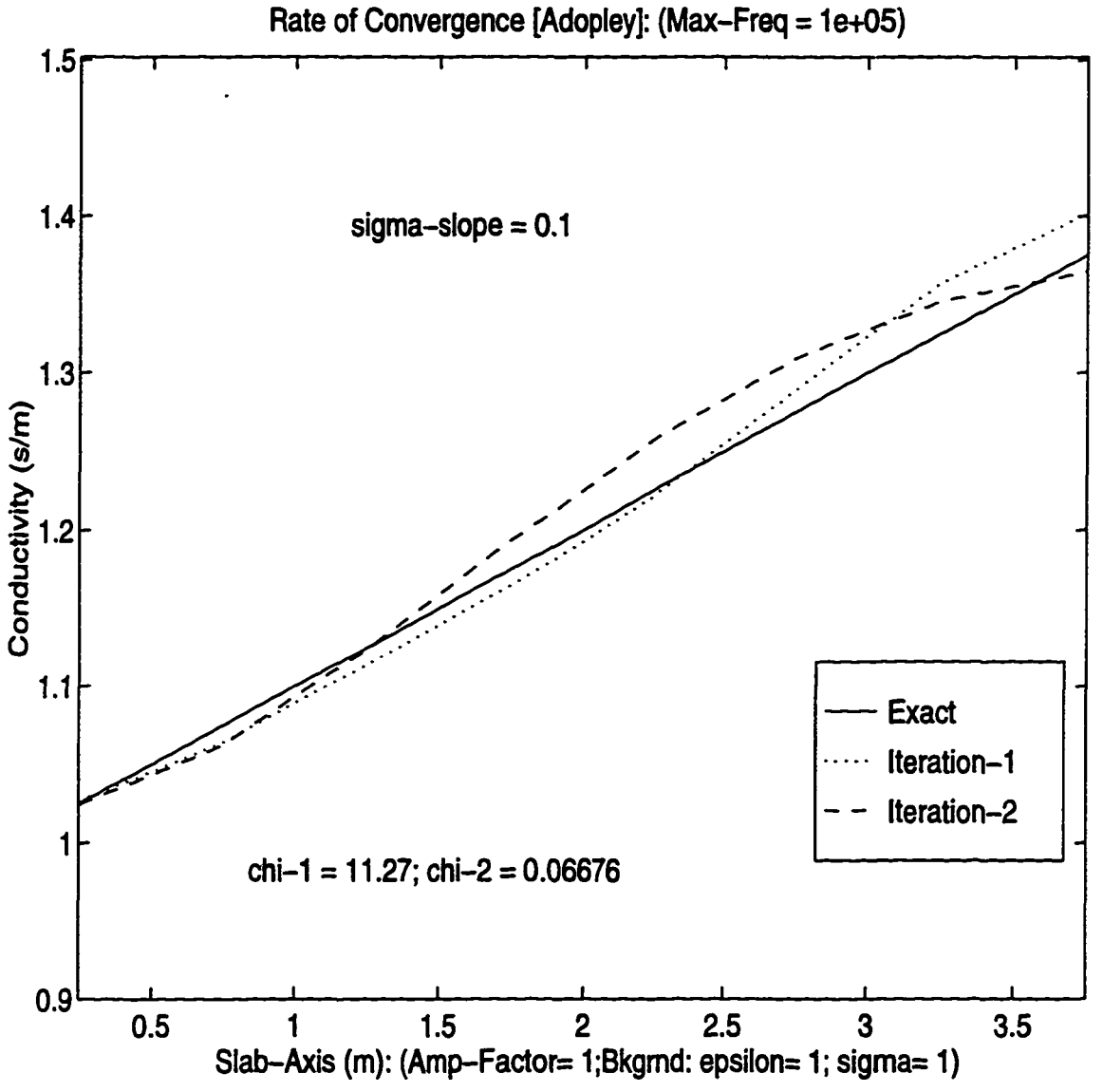

Figure 8.23: Rate of Convergence at each Iteration in Profile Reconstruction Using the Adopley model

CHAPTER 9

Future Work

Our immediate plans for the future are to extend the investigation on the localized approximation to three dimensions. Below we present a general three-dimensional formulation as communicated to us by Habashy [20]. Although this formulation is not ours, we include it for future reference, with permission.

9.1 The Extended Born Approximation for 3-D Modeling (An Iterative Approach)

The wave equation for the electric field is given by

$$\nabla \times \nabla \times \bar{E}(\bar{r}) - k^2(\bar{r})\bar{E}(\bar{r})i = j\omega\mu_o\bar{J}(\bar{r}) - \nabla \times \bar{M}(\bar{r}) \tag{9.1}$$

which can be cast as follows:

$$\nabla \times \nabla \times \bar{E}(\bar{r}) - k_b^2\bar{E}(\bar{r}) = k_b^2\tilde{\sigma}(\bar{r})\bar{E}(\bar{r}) + k_b^2\bar{S}(\bar{r}) \tag{9.2}$$

where

$$k^2(\bar{r}) = j\omega\mu_o\sigma(\bar{r}) \tag{9.3}$$

$$k_b^2 = j\omega\mu_o\sigma_b \tag{9.4}$$

$$\tilde{\sigma}(\bar{r}) = \frac{\sigma(\bar{r})}{\sigma_b} - 1 \tag{9.5}$$

$$\bar{S}(\bar{r}) = \frac{1}{\sigma_b}\bar{J}(\bar{r}) - \frac{1}{k_b^2}\nabla \times \bar{M}(\bar{r}) \tag{9.6}$$

$\bar{J}(\bar{r})$ and $\bar{M}(\bar{r})$ are the electric and magnetic impressed sources, respectively, $\sigma(\bar{r})$ is the actual complex conductivity distribution and σ_b is a constant complex conductivity of a homogeneous background medium. We introduce a Dyadic Green function governed by the following equation:

$$\nabla \times \nabla \times \bar{\bar{G}}_b(\bar{r},\bar{r}') - k_b^2\bar{\bar{G}}_b(\bar{r},\bar{r}') = k_b^2\bar{\bar{I}}\delta(\bar{r},\bar{r}') \tag{9.7}$$

The solution of equation (9.7) can be represented in the following form:

$$\bar{\bar{G}}_b(\bar{r},\bar{r}') = \left[k_b^2\bar{\bar{I}} + \nabla\nabla\right] g(\bar{r},\bar{r}') \tag{9.8}$$

and $g(\bar{r},\bar{r}')$ is the scalar Green's function governed by

$$\nabla^2 g(\bar{r},\bar{r}') + k_b^2 g(\bar{r},\bar{r}') = -\delta(\bar{r},\bar{r}') \tag{9.9}$$

and is given by the following expression:

$$g(\bar{r},\bar{r}') = \frac{e^{jk_b|\bar{r}-\bar{r}'|}}{4\pi|\bar{r}-\bar{r}'|} \tag{9.10}$$

We represent the solution of equation (9.2) in terms of the dyadic Green's function of equation (9.7) as follows:

$$\begin{aligned} \bar{E}(\bar{r}) &= \bar{E}_b(\bar{r}) + \int_{V_s} d\bar{r}'\bar{\bar{G}}_b(\bar{r},\bar{r}')\cdot\bar{E}(\bar{r}), \qquad \bar{r} \notin V_s \\ &= \bar{E}_b(\bar{r}) + (k_b^2\bar{\bar{I}} + \nabla\nabla)\cdot\int_{V_s} d\bar{r}' g(\bar{r},\bar{r}')\bar{E}(\bar{r}), \qquad \bar{r} \in V_s \end{aligned} \tag{9.11}$$

where V_s is the support of $\tilde{\sigma}(\bar{r})$ and $\bar{E}_b(\bar{r})$ is the response in the background medium and it the solution to the following wave equation:

$$\nabla \times \nabla \times \bar{E}_b(\bar{r}) - k_b^2 \bar{E}_b(\bar{r}) = k_b^2 \bar{S}(\bar{r}) \tag{9.12}$$

which can be solved in Dyadic Green's function form as follows:

$$\bar{E}_b(\bar{r}) = \int d\bar{r}' \bar{\bar{G}}_b(\bar{r}, \bar{r}') \cdot \bar{S}(\bar{r}') \tag{9.13}$$

One of the standard approaches in solving equation (9.11) is by repeated iteration resulting in the Born series (or the Neuman series):

$$\bar{E}(\bar{r}) = \sum_{n=0}^{N-1} \bar{E}_n(\bar{r}) + \bar{e}_N(\bar{r}) \tag{9.14}$$

where we only keep the first $N-1$ iterations with a residual error $\bar{e}_N(\bar{r})$, and

$$\bar{E}_0(\bar{r}) = \bar{E}_b(\bar{r}) \tag{9.15}$$

The n^{th} iterate is given by

$$\begin{aligned} \bar{E}_n(\bar{r}) &= \int_{V_s} d\bar{r}' \tilde{\sigma}(\bar{r}') \bar{\bar{G}}_b(\bar{r}, \bar{r}') \cdot \bar{E}_{n-1}(\bar{r}') \\ &= \int_{V_s} d\bar{r}_1 \tilde{\sigma}(\bar{r}_1) \bar{\bar{G}}_b(\bar{r}, \bar{r}_1) \cdot \int_{V_s} d\bar{r}_2' \tilde{\sigma}(\bar{r}_2) \bar{\bar{G}}_b(\bar{r}_1, \bar{r}_2) \cdots \\ &\cdot \int_{V_s} d\bar{r}_{n-1} \tilde{\sigma}(\bar{r}_{n-1}) \bar{\bar{G}}_b(\bar{r}_{n-2}, \bar{r}_{n-1}) \cdot \int_{V_s} d\bar{r}_n \tilde{\sigma}(\bar{r}_n) \bar{\bar{G}}_b(\bar{r}_{n-1}, \bar{r}_n) \cdot \bar{E}_b(\bar{r}_n) \end{aligned} \tag{9.16}$$

and

$$\begin{aligned} \bar{e}_N(\bar{r}) &= \int_{V_s} d\bar{r}_1 \tilde{\sigma}(\bar{r}_1) \bar{\bar{G}}_b(\bar{r}, \bar{r}_1) \cdot \int_{V_s} d\bar{r}_2' \tilde{\sigma}(\bar{r}_2) \bar{\bar{G}}_b(\bar{r}_1, \bar{r}_2) \cdots \\ &\cdot \int_{V_s} d\bar{r}_{N-1} \tilde{\sigma}(\bar{r}_{N-1}) \bar{\bar{G}}_b(\bar{r}_{N-2}, \bar{r}_{N-1}) \cdot \int_{V_s} d\bar{r}_N \tilde{\sigma}(\bar{r}_N) \bar{\bar{G}}_b(\bar{r}_{N-1}, \bar{r}_N) \cdot \bar{E}(\bar{r}_N) \end{aligned} \tag{9.17}$$

An alternative representation for the residual $\bar{e}_N(\bar{r})$ is given by the following recurrence formula:

$$\bar{e}_n(\bar{r}) = \int_{V_s} d\bar{r}' \tilde{\sigma}(\bar{r}') \bar{\bar{G}}_b(\bar{r}, \bar{r}') \cdot \bar{e}_{n-1}(\bar{r}') \qquad n = 1, 2, \cdots, N-1, N \tag{9.18}$$

with

$$\bar{e}_0(\bar{r}) = \bar{E}(\bar{r}) \tag{9.19}$$

To derive an *Extended Born approximation,* we apply a localization to either equation (9.17) or equation (9.18) to obtain two different approximations:

9.1.1 Approximation (I):

Applying a repeated localization approximation to equation (9.17), where:

$$\bar{E}(\bar{r}_N) \approx \bar{E}(\bar{r}_{N-1}) \approx \cdots \approx \bar{E}(\bar{r}_2) \approx \bar{E}(\bar{r}_1) \approx \bar{E}(\bar{r}) \tag{9.20}$$

we get

$$\bar{e}_N(\bar{r}) \approx \bar{\bar{\Lambda}}_N(\bar{r}) \cdot \bar{E}(\bar{r}) \tag{9.21}$$

where $\bar{\bar{\Lambda}}_N(\bar{r})$ is a tensor given by the following N-tuple integral:

$$\begin{aligned} \bar{\bar{\Lambda}}_N(\bar{r}) \;=\; & \int_{V_s} d\bar{r}_1 \tilde{\sigma}(\bar{r}_1) \bar{\bar{G}}_b(\bar{r}, \bar{r}_1) \cdot \int_{V_s} d\bar{r}_2 \tilde{\sigma}(\bar{r}_2) \bar{\bar{G}}_b(\bar{r}_1, \bar{r}_2) \cdots \\ & \cdot \int_{V_s} d\bar{r}_{N-1} \tilde{\sigma}(\bar{r}_{N-1}) \bar{\bar{G}}_b(\bar{r}_{N-2}, \bar{r}_{N-1}) \cdot \int_{V_s} d\bar{r}_N \tilde{\sigma}(\bar{r}_N) \bar{\bar{G}}_b(\bar{r}_{N-1}, \bar{r}_N) \end{aligned} \tag{9.22}$$

Substituting from equation (9.21) in equation (9.14), we obtain the following approximation for the internal electric field:

$$\bar{E}^{int}(\bar{r}) \approx \bar{\bar{\Gamma}}_N(\bar{r}) \cdot \sum_{n=0}^{N-1} \bar{E}_n(\bar{r}) \tag{9.23}$$

where

$$\bar{\bar{\Gamma}}_N(\bar{r}) = \left[\bar{\bar{I}} - \bar{\bar{\Lambda}}_N(\bar{r})\right]^{-1} \tag{9.24}$$

Note that for $N = 1$, the localized approximation becomes:

$$\bar{E}^{int}(\bar{r}) \approx \bar{\bar{\Gamma}}_1(\bar{r}) \cdot \bar{E}_b(\bar{r}) \tag{9.25}$$

where

$$\bar{\bar{\Gamma}}_1(\bar{r}) = \left[\bar{\bar{I}} - \bar{\bar{\Lambda}}_1(\bar{r})\right]^{-1} \tag{9.26}$$

and

$$\bar{\bar{\Lambda}}_1(\bar{r}) = \int_{V_s} d\bar{r}' \tilde{\sigma}(\bar{r}') \bar{\bar{G}}_b(\bar{r}, \bar{r}') \tag{9.27}$$

which gives the original Extended Born approximation of [17].

9.1.2 Approximation (II):

Applying the localized approximation to equation (9.18), we obtain

$$\bar{e}_n(\bar{r}) \approx \bar{\bar{\Omega}}(\bar{r}) \cdot \bar{e}_n(\bar{r}), \qquad n = 1, 2, \cdots, N-1, N \tag{9.28}$$

where

$$\bar{\bar{\Omega}}(\bar{r}) = \int_{V_s} d\bar{r}' \tilde{\sigma}(\bar{r}') \bar{\bar{G}}_b(\bar{r}, \bar{r}') \tag{9.29}$$

Hence,

$$\bar{e}_n(\bar{r}) \approx \bar{\bar{\Omega}}(\bar{r})]^N \cdot \bar{E}(\bar{r}) \tag{9.30}$$

Substituting from equation (9.30) in equation (9.14), we obtain the following approximation for the internal electric field:

$$\bar{E}^{int}(\bar{r}) \approx \bar{\bar{\Gamma}}_N(\bar{r}) \cdot \sum_{n=0}^{N-1} \bar{E}_n(\bar{r}) \tag{9.31}$$

where

$$\bar{\bar{\Gamma}}_N(\bar{r}) = \left[\bar{\bar{I}} - [\bar{\bar{\Omega}}(\bar{r})]^N\right]^{-1} \tag{9.32}$$

we again note that for $N = 1$, this localized approximation gives the original Extended Born approximation of [17]. It is important to note that the $e^{-i\omega t}$ sign convention used in this derivation is the negative of the one we employed in our one-dimensional analysis.

We also note that, for $N = 2$, the first approximation yields the 3-D version of the Adopley approximation. We reiterate that the above work was communicated to us from Habashy [20] and we do not claim any credit in its construction. We do however plan on performing simulations in the future based on his formulation.

CHAPTER 10

Summary and Conclusions

This works concerns the comparative performance of localized approximations in one-dimensional complex conductivity profile reconstruction. The integral equation (Chapter 2) that describes the one-dimensional electromagnetic wave propagation is deceptively very simple. The hidden difficulty begins to unravel as it is realized that the elements in the integrand of the integral equation are nonlinearly interdependent. Specifically, the total internal field is a function of the difference between the scatterer and background complex conductivity profiles. The localized approximation as was originally proposed is extended herein and performances evaluated.

In Chapter 3 , we developed the equations for the localized approximation and also for the various extensions. Also included are the Trantanella approximation and the extension of the Trantanella approximation to incorporate the localized approximation. In the first extension, which we denote the Adopley model, we applied the Born approximation before adopting the localized approximation. A second extension, which we called the Extended Habashy approximation, was developed by iterating the localized approximation once. We showed how the Adopley approximation can be obtained as a special case from one of two generalized localized approximations

using the extended Born approximation. However, the Extended Habashy could not be immediately extracted from any of the two generalized localized approximations. We concluded the chapter by investigating the implications of homogeneous complex conductivity background. It was proved that for the inversion of a lossy media, the background medium has to be lossy also.

In Chapter 6 we carried out simulations of the internal and external field of the slab problem with the various approximations developed. For low contrast between the background and slab complex conductivities, all the approximations gave excellent results. The results were compared against the exact simulations from transmission-line solution. Generally, for very low loss systems the Adopley approximation provided the best results. When the system becomes very lossy the Habashy and the Extented Habashy provided the best results, with a slight edge on accuracy from the Extended Habashy model if numerical noise is negligible. Generally, the Trantanella approximation provided very good results. The chapter ended with relative comparisons of the various approximations for lossy linear profiles. Generally, all approximations performed well at moderate frequencies of simulations. We also found that the maximum frequency of accurate field simulation increases with decrease in conductivity contrast.

We developed the smoothest (Occam's) inversion algorithm in Chapter 7. The algorithm involves a minimization of the model roughness functional, subject to constraint on the magnitude of a weighted least-squares criterion between the measured

and predicted data. In Chapter 8 we applied the inversion algorithm to synthetic data. Two profiles were used in the numerical inversions, viz: the piecewise constant profile and the linear profile. The reconstructions were very promising. We note, however, that we could not reconstruct very sharp contrasts in conductivity profiles exactly. This is because Occam's inversion method is L_2 *norm* dependent. In general for very low loss profiles the Adopley model gives the best reconstruction. For high contrast in profile conductivities between the homogeneous background and the slab, the best reconstruction are from the Habashy and the extended Habashy models. We note that the Adopley model diverges when the conductivity contrast gets too large. Also, we observed that the contrast level for accurate reconstruction for the Adopley model decreases with increase in background conductivity. Concerning speed of performance, the Habashy model was the fastest. We noted the Extended Habashy model to be very slow when the number of unknowns exceeds 20. This we attribute to the numerical computation of the internal field. The Adopley model performed at moderate speed, slower than Habashy.

One limitation from the present work is that the inversion was restricted to real conductivity profiles only. This is because of the frequency dependence of the complex conductivity with subsequent high differences in orders of magnitude for the imaginary part of the complex conductivity. One way to circumvent this may be to adopt the subspace technique proposed in [26, 27]. This we recommend as future

work. Also we have not investigated the performance of the second generalized localized approximation beyond the one-term approximation. This we intend to follow up in the very near future.

REFERENCES

[1] N. Bleistein and J. K. Cohen, "Nonuniqueness in inverse source problems in acoustics and electromagnetics", *Journal of Mathematical Physics*, vol. 18, no. 2, pp. 194-201, February 1977.

[2] A. J. Devaney, "Nonuniqueness in the inverse scattering problem", *Journal of Mathematical Physics*, vol. 19, no.7, pp. 1526-31, July 1978.

[3] A. J. Devaney and E. Wolf,"Radiating and Nonradiating Classical Currents Distributions and the Fields They Generate ", *Physical Review D*, vol. 8, no. 4, pp. 1044-47, August 1973.

[4] iR. P. Porter and A. J. Devaney, "Holography and the inverse source problem,", *J. Opt. Soc. Am.*, 72, pp. 327-330, 1982.

[5] R. Stone, "A review and examination of results on uniqueness in inverse problems", *Radio Science*, Vol. 22, No. 6, pp. 1026-1030, November 1987.

[6] R. L. Parker, "Understanding inverse theory", *Ann. Rev. Earth Planet. Sci.*, 5, pp. 35-64, 1977.

[7] G. E. Backus and J. F. Gilbert, "Numerical application of a formalism for geophysical inverse problems", *Geophys. J. R. Astron. Soc.*, vol. 13, pp. 247-276, 1967.

[8] G. Backus and F. Gilbert, "The resolving power of gross Earth data", *Geophys. J. R. Astron. Soc.*, vol. 16, pp. 169-205, 1968.

[9] G. Backus and F. Gilbert, "Uniqueness in the inversion of inaccurate gross Earth data", *Phil. Trans. R. Soc. London. Ser. A*, vol. 266, pp. 123-192, March 1970.

[10] T. M. Habashy, R. W. Groom and B. R. Spies, "Beyond the Born and Rytov approximations: A nonlinear approach to electromagnetic scattering", *Journal of Geophysical Research*, vol. 98, no. B2, pp. 1759-1775, February 1993.

[11] M. Born and E. Wolf, *Principles of Optics*, Pergamon, New York, 1980.

[12] S. M. Rytov, "Diffraction of light by ultrasonic waves", *Izv. Akad. Nauk. SSSR.*, Ser. Fiz. 2, 223, 1937.

[13] M. L. Oristaglio, "Accuracy of the Born and Rytov approximations for the reflection and refraction at a plane interface", *Optical Society of America*, vol. 2, no. 11, pp. 1987-1992, November 1985.

[14] L. R. Rabiner and R. W. Schafer, *Digital Processing of Speech Signals*, Prentice-Hall, Englewood Cliffs, N.J., 1978.

[15] J. B. Keller, "Accuracy and validity of the Born and Rytov approximations", *J. Opt. Soc. Am.*, vol. 59, pp. 1003-1004, August 1969.

[16] M. Sancer and A. D. Varvatsis, "A comparison of the Born and Rytov methods", *Proceedings of the IEEE*, pp. 140-141, January 1970. Holden-Day, 1976.

[17] C. Torres-Verdin and T. M. Habashy, "Rapid 2.5-dimensional forward modeling and inversion via a new nonlinear sacttering approximation", *Rado Science*, vol. 29, no. 4, pp. 1051-1079, July-August 1994.

[18] C. J. Trantanella, "Beyond the Born approximation in one- and two-dimensional profile reconstruction", Masters thesis submitted to the faculty of the Department of Electrical and Computer Engineering, University of Arizona, May 1994.

[19] C. J. Trantanella, D. G. Dudley and K. A. Nabulsi, "Beyond the Born approximation in one-dimensional profile reconstruction", *J. Opt. Soc. Am.*, vol. 12, no. 7, pp. 1469-1478, July 1995.

[20] T. M. Habashy, "Private communications" *Schlumberger-Doll Research, Old Quary Road, Ridgefield, CT.*

[21] S. Ramo, J. R. Whinnery and T. Van Duzer, *Fields and Waves in Communication Electronics*, Second Edition, John Wily & Sons Inc., 1984.

[22] W. Tabbara, "Reconstruction of Permittivity profiles from a Spectral Analysis of the reflection Coefficient", *IEEE Transactions on Antenna and Propagation*, vol. AP-27, no. 2, pp. 241-244, March 1979.

[23] J. S. Chipman, "On least squares with insufficient observation", *Americam Statistical Association Journal*, pp. 1078-1111, December 1964.

[24] Y. Zhou and C. K. Rushforth, "Least-squares reconstruction of spatially limited objects using smoothness and non-negativity constraints", *Applied Optics*, vol. 21, no. 7, pp. 1249-1252, April 1982.

[25] A. G. Tijhuis and C. Van Der Worm, "Iterative approach to the frequency-domain solution of the inverse-scattering problem for an inhomogeneous lossless dielectic slab", *IEEE Transactions on Antenna and Propagation*, vol. AP-32, no. 7, pp. 711-716, July 1984.

[26] B. L. N. Kennett and P. R. Williamson, "Subspace methods for large-scale non-linear inversion", *Mathematical Geophysics*, pp. 139-154, 1988.

[27] B. L. N. Kennett, M. S. Sambridge and P. R. Williamson, "Subspace methods for large inverse problems with multiple parameter classes", *Geophysicical Journal*, 94, pp. 237-247, 1988.

[28] M. S. Sambridge, "Non-linear arrival time inversion: constrained velocity anomalies by seeking smooth model in 3-D", *Geophys. J. Int.*, 102, pp. 653-677, 1990.

[29] D. W. Oldenburg and R. G. Eliss, "Inversion of geophysical data using an approximate inverse mapping", *Geophys. J. Int.*, 105, pp. 325-353, 1991.

[30] D. W. Oldenburg, P. R. McGillivary and R. G. Eliss, "Generalized subspace methodes for large-scale inverse problems", *Geophys. J. Int.*, 114, pp. 12-20, 1993.

[31] R. E. Kleinman and P. M. van den Berg, "An extended range-modified gradient technique for profile inversion", *Radio Science*, vol. 28, no. 5, pp. 877-884, 1993.

[32] K. Levenberg, "A method for the solution of certain non-linear problems in least squares", *Quart. Appl. Math.*, no. 2, pp. 164-168, July-August 1944.

[33] D. W. Marquardt, "Least squares analysis of electron paramahnetic resonance Spectra", *Journal of Molecular Spectroscopy*, 7, pp. 269-279, 1961.

[34] D. W. Marquardt, "Generalized inverses, ridge regression, biased linear estimation and nonlinear estimation", *Tecnometrics*, vol. 2, no. 3, pp. 591-612, 1970.

[35] A. N. Tikhonov and V. Y. Arsenin, *Solutions of Ill-Posed Problems*, V. H. Winston & Sons, Washington, D.C., 1977.

[36] S. C. Constable, R. L. Parker, and C. G. Constable, "Occam's inversion: A practical algorithm for generating smooth models from electromagnetic sounding data", *Geophysics*, vol. 52, no. 3, pp. 289-300, March 1987.

[37] J. T. Smith and J. R. Booker, "Magnetotelluric inversion for minimum structure", *Geophysics*, vol. 53, no. 12, pp. 1565-1576, December 1988.

[38] L. I. Rudin, S. Osher and E. Fatemi, "Nonlinear total variation based noise removal algorithm", *Physica D*, 60, pp. 259-268 1992.

[39] S. Osher and L. I. Rudin, "Feature-oriented image enhancement using shock filters", *SIAM J. Numer. Anal.*, vol. 27, no. 4, pp. 919-940, August 1990.

[40] P. M. van den Berg and R. E. Kleinman, "A total variation enhanced modified gradient algorithm for profile reconstruction", *University of Delaware Tecnical Report*, Newark DE 19716, vol. 95-4, 1995.

[41] D. Oldenburg, "Inversion of electromagnetic data: An overview of new techniques", *Surveys in Geophysics*, 11, pp. 231-270, 1990.

[42] T. M. Habashy and R. Mittra, "On some inversion methods in electromagnetics", *Journal of Electromagnetic Waves and Applications*, vol. 1,no. 1, pp. 25-58, 1987.

[43] E. L. Miller and A. S. Willsky, "A multiscale, statistically based inversion scheme for linearized inverse scattering problems", *IEEE Transactions on Geoscience and Remote Sensing*, vol. 34, no. 2, pp. 346-357, March 1996.

[44] M. S. Zhdanov and S. Fang, "Three-dimensional quasi-linear electromagnetic inversion", *Radio Science*, vol. 31, no. 4, pp. 741-754, July-August 1996.

[45] D. G. Dudley, *Mathematical Foundations for Electromagnetic Theory,* IEEE, Piscataway, NJ, USA, 1994.

[46] W. H. Press, S. A. Teukolsky,W. T. Vetterling and B. P. Flannery, *Numerical Recipes in Fortran: The Art of Scientific Computating* Second Edition, Cambridge University Press, 1992.

[47] H. Jeffreys, "An alternative to the rejection of observations", *Proceedings of the Royal Society of London*, ser. A, vol. CXXXVII, pp 78-87, September 1932.

[48] C. M. Bender and S. A Orszag, *Advanced mathematical methods for scientists and engineers*, McGraw-Hill, Inc., 1978.